EXPERIMENTAL AND NUMERICAL CHARACTERIZATION OF THE FRETTING FATIGUE BEHAVIOR OF ELASTOMERS

Dissertation by

Szilárd Tamás Vezér

prepared at the

Polymer Competence Center Leoben GmbH

and the

Institute of Materials Science and Testing of Plastics

submitted to the

Montanuniversität Leoben

Academic Advisor
Univ.-Prof. Dipl.-Ing. Dr. Gerald Pinter
Montanuniversität Leoben, Austria

Supervisor
Univ.-Prof. Dr. Zoltán Major
Johannes Kepler University Linz, Austria

Referees
Univ.-Prof. Dipl.-Ing. Dr. Gerald Pinter
Montanuniversität Leoben, Austria
Priv.-Doz. Dipl.-Ing. Dr. Hans-Peter Gänser
Montanuniversität Leoben, Austria

Leoben, Januar 2011

DECLARATION

I declare in lieu of oath, that I wrote this thesis and performed the associated research myself, using only literature cited in this volume.

Leoben, Januar 2011

Vezér Szilárd

(Szilárd Tamás Vezér)

ACKNOWLEDGEMENT

Though only my name appears on the cover of this dissertation, a great many people have contributed to its production. I owe my gratitude to all those people who have made this dissertation possible and because of whom my graduate experience has been one that I will cherish forever.

Firstly, I would like to thank my mentor Prof. Zoltán Major for introducing me to the principles of scientific work in material science and testing of plastics. I have been amazingly fortunate to have an advisor who gave me the freedom to explore on my own and at the same time the guidance to recover when my steps faltered. I am also grateful to Prof. Reinhold W. Lang for his tireless work as the scientific leader of the PCCL and the head of the Institute of Materials Science and Testing of Plastics at the Montanuniversität Leoben.

The research work of this paper was performed at the Polymer Competence Center Leoben GmbH within the framework of the K_{plus}-program of the Austrian Ministry of Traffic, Innovation and Technology with contributions from University of Leoben and SKF Economos Austria GmbH. The PCCL was founded by the Austrian Government and the State Governments of Styria and Upper Austria. I would like to acknowledge the members of the project partners for their support: Dr. Thomas Schwarz, Manfred Moitzi and Mario Mitterhuber.

I would like to thank my colleagues of the PCCL for many discussions and help in recent years. I am indebted to Peter Fuchs, Michael Berer for their advice in the finite element simulations and to Andreas Hausberger, Stefan Hinterdorfer, Dr. László Oláh, Martin Reiter, Bernd Schrittesser and Rath Walter for being ministerial to the experimental works. Many thanks to Dr. Robin Steinberger for helping decisively with various aspects, especially in the development stage of the optical measurement software. Special thank goes to Jürgen Föttinger for manufacturing test instruments.

I want to express my sincere gratitude to my parents for their great support that made my education and therefore also this paper possible. Finally, I am indebted to my girlfriend Viktória for her patience and devoted helpfulness.

ABSTRACT

Fretting fatigue behaviour has recently been investigated for a number of engineering polymers. Due to the stress concentration in the contact zone and due to the small tangential oscillations, cracks may initiate rapidly under fretting conditions or under stick-slip conditions. The fretting wear and the fretting fatigue could cause a catastrophic failure both for metals and polymer composites, but this behaviour was also observed for elastomeric materials.

To generate fretting crack initiation and to characterize the fretting behavior of elastomers, a new complex test and analysis method was developed and used, as described in the first part of the thesis. The schematic representation of this fretting method is shown in Figure A along with the research connections to the other chapters of this thesis. The sliding regimes of the two elastomers investigated (Hydrogenated Nitrile Butadiene Rubber – HNBR, thermoplastic polyurethane grade - TPU) were determined in short-term experiments. Furthermore, to characterize the fretting fatigue material response under various loading conditions, long-term fretting fatigue tests were performed with different displacement amplitudes at a specific normal force level. Moreover, specimen surfaces were analyzed by optical and electron microscope images. Depending on the location of the contact area and the displacement amplitude, different wear types were determined.

In addition to the fretting measurements, hyperelastic material models were defined along with appropriate material parameters for both elastomeric materials. Additionally, fretting contact situations were simulated using the finite element method. The spatial and temporal distributions of the stresses on the elastomer surfaces were determined and plotted in terms of normal and shear stresses versus tangential sliding distances. Finally, the observations of the failure analysis and the results of the FE simulations were summarized in fretting failure models for both elastomers, as described in the first part of this thesis.

Chapter 2 of the thesis contains the development of novel tools for a non-contact, optical observation of the strain and damage initiation during cyclic fatigue measurements. For these optical measurements an image acquisition software tool was written in LabVIEW. It was possible to save comparable pictures of the test specimen surfaces at the displacement maximum of the cycles with an analog-signal triggered timing module in this program. Some examples of real applications of this software tool for cyclic tests are also demonstrated in this study.

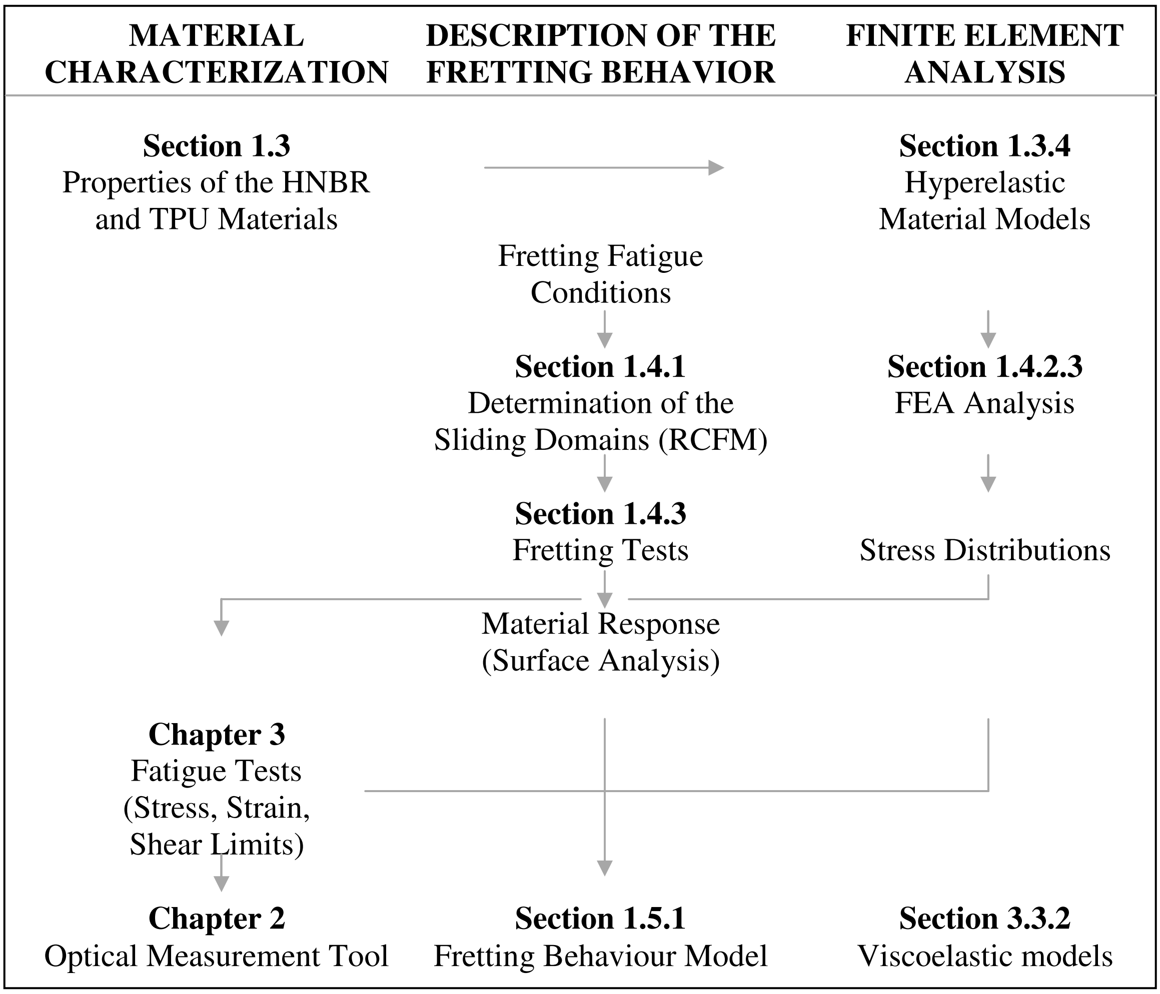

Fig. A: Flowchart of the chapters of this thesis

To get more information about the bulk material fatigue behaviour, conventional force controlled fatigue experiments were performed at room temperature, at a test frequency of 1 Hz, and at a nominal stress ratio of $R_{\sigma}=0.1$. The results are described and discussed in section 3.2 of the thesis. In addition to the conventional fatigue analysis by Wöhler curves, the hysteretic behaviour was analyzed in detail up to the ultimate failure. The damage initiation was tracked by the image acquisition system which was introduced in the previous chapter.

Furthermore, a new specimen form was introduced and a novel combined experimental/FE simulation procedure was developed to determine local strain based Wöhler curves for the elastomers, as described in section 3.3. To determine reliable cycles-to-failure data, displacement controlled cyclic tests were carried out at room temperature and at a strain ratio of $R_{\varepsilon}=0.1$. To establish relationships between the local stress-strain states and the global displacement, the strain distribution in the Diabolo-type specimen was analyzed with a finite element simulation using a viscoelastic-hyperelastic material model.

Finally, to complete the bulk fatigue characterization and to extend the significance to more complex multiaxial loading conditions, cyclic torsion experiments were performed and shear stress Wöhler curves determined. The overall assumption for all Wöhler curves was that a distinct fatigue strength limit exists, at least for practical engineering applications. Hence, the data points were correlated by proper mathematical functions and the fatigue strength limit values determined in terms of nominal stress, local true strain and shear stress values for both elastomers investigated in this thesis.

TABLE OF CONTENTS

1. FRETTING FATIGUE

1.1 Introduction and objectives

Due to industry demand, fretting damages of metallic materials have been widely investigated for 30 years (Waterhouse, 1972; 1981). Fretting wear and fretting fatigue are now determined as the response of materials under global overstraining or local overstressing of the material surface in sliding contacts (King, 1981). These two failure mechanisms (fatigue and wear) are connected to the particle detachment, crack nucleation and propagation, which can lead to catastrophic failure. Fretting fatigue damage has been reported in many engineering applications (like in the parts of helicopters, fixed-wing aircrafts, automotives, orthopaedic implants etc.) by Hoeppner (Hoeppner, 1992). Due to the material loss and crack formations, the fretting behaviour can not be determined only by the bulk material properties of the contacting bodies. Along with the loading parameters and the properties of the interfaces, the environmental atmospheres also have different effects on the failure mechanisms. In spite of that, there are some existing approaches to describe the fretting damage. However, the determination of the relevant material fretting properties and the fatigue life time predictions are still under research.

1.1.1 Fretting regimes

The fretting behaviour has been described with experimental and theoretical results by Waterhouse (Waterhouse, 1972; 1981). The main parameters were reported to be displacement amplitude, normal load, frequency, surface roughness, morphology and residual stresses. In vibration contact, depending on two basic parameters, on the normal load or on the tangential displacement amplitude, the contact conditions can be either partial slip or gross slip. These two states do not produce the same local loading on the surface. Under partial slip conditions as it was described by Mindlin, in sphere/plane contact, in the middle dominates the sticking surrounded by circular oscillating domains (Mindlin, 1993). When gross slip occurs, however, a full sliding phase can be observed after the initial partial slip evolution. The dominant sliding conditions depend on the normal force (P) and the displacement (δ) and they are described in a sliding condition fretting map (Vingsbo, 1988) like Figure 1.1 shows. The transition line can be determined from the measured tangential force (Q) vs. tangential displacement diagrams (δ).

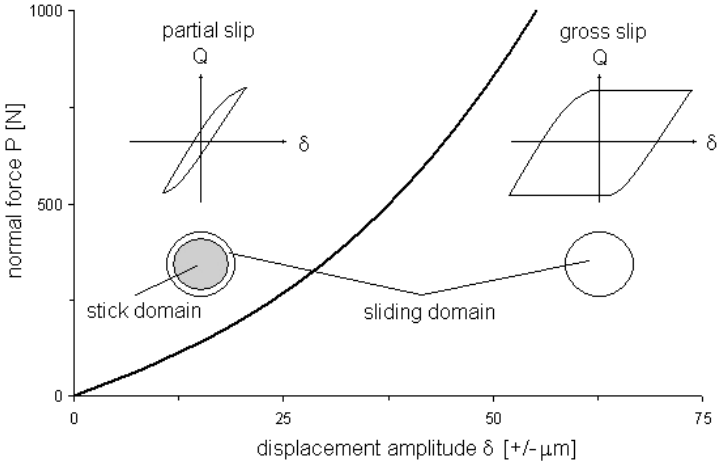

Fig. 1.1: Sliding condition by Vingsbo et al. (Vingsbo, 1988).

These two fretting conditions (partial slip and gross slip) have been modified to three regions by Vincent et al., which result in three different fretting regimes (Vincent, 1992). Displaying the test parameters and the material answers in the diagrams, we are able to describe the Running Condition Fretting Map (RCFM) and the Material Response Fretting Map (MRFP), as it is shown in Figure 1.2. When the sliding condition does not change throughout the test duration, partial slip (PSR) or gross slip (GSR) regimes are considered. Mixed slide regime (MSR) is that area in the displacement-normal force diagram, where the sliding tangential force changes during the test time (Zhou, 1995).

Determination of this transition criterion for steels was published by Fouvry et al. (Fouvry, 1995). Based on the hysteresis cycles, a tribologically independent criterion has been described as the quotient of the dissipated energy and work area of the smallest parallelogram around the hysteresis curve:

$$B = \frac{W_d}{4 \cdot Q \cdot \delta_0} \tag{1.1}$$

where W_d is the dissipated energy, Q is the maximum tangential force and δ_0 is the displacement aperture of a cycle (Q=0). For the used steel materials, this system free criterion was defined in the value of B=0.77 and this region has been defined as the most dangerous regime for crack nucleation and service failure.

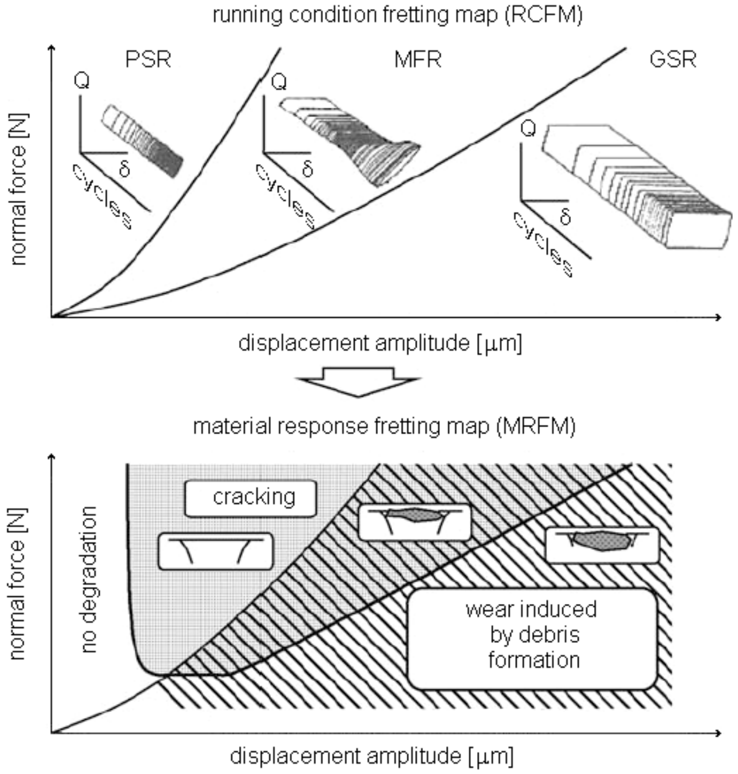

Fig. 1.2: Running condition (RCFM) and material response fretting map (MRFM) (Vincent 1992).

In a surface contact with low relative displacement at high frequency, the fretting wear mechanisms are also potential failure behaviour for polymeric materials (Briscoe, 1998). During the fretting wear the debris, as a third body in the interaction, can not be transported out easily from the sliding zone and plays basic role in the wear of materials (Godet, 1984; Hurricks, 1970).

1.1.2 Description of the contact area

The sphere-plane contact is described in several studies. The basic contact pressure distribution comes from the Hertzian equation, which is independent from the shear stresses:

$$p(x) = p_0\sqrt{1-\frac{x^2}{a^2}} \tag{1.2}$$

where a is the half width of the contact area, and p_0 is the maximum pressure.
Under gross slip conditions the relative motion between the contacting surfaces induces severe modification of the contact geometry, the contact area increases and the Hertzian stress (Hertz, 1895) description is no more valid. The cyclic stress distribution can be estimated by the combination of the Cattaneo-Mindlin model (Mindlin, 1953) and the Stackfield and Hills or Hamilton sphere-plane expressions (Hamilton, 1983).
Figure 1.3 shows the distribution changes under tangential loading in 2D. Shear traction on the surface ($\tau_{(x;0)}$) is zero outside the contact zone (|x|>a), while in the stick zone (|x|<c) $\tau_{(x;0)}<\mu p_{(x)}$, where μ denotes the friction coefficient.

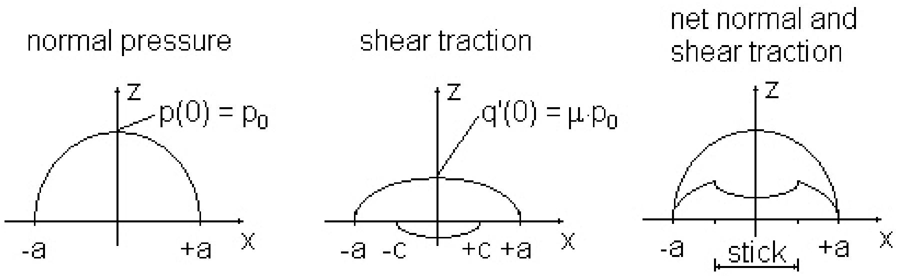

Fig. 1.3: Fretting contact problem illustration.

The surface shear traction can be described with the following equations:

$$\tau_{(x,0)} = q'(x)+q''(x) \tag{1.3}$$

$$q'(x) = \mu\cdot\frac{p_0}{a}\sqrt{a^2-x^2} \tag{1.4}$$

$$q''(x) = -\mu\cdot\frac{p_0}{a}\sqrt{c^2-x^2} \tag{1.5}$$

where q is a stress-like quantity and q' and q" are components. These values are valid at the point of maximum monotonic tangential load (Q'_{max}, where q'''(x)=0). For dynamic loading and unloading conditions, an expression for the subsurface stress was also published by Szolwinski and Farris (Szolwinski, 1996).

1.1.2.1 Deformation energy

It has to be differentiated between the fretting and reciprocating gross slip. In the more interesting first case, an unexposed surface exists, which means the displacement amplitude is smaller than the length of the contact area. The dissipated energy was described with by Hertzian shear and pressure field distribution in the PhD Thesis of Fouvry (1996) (Figure 1.4).

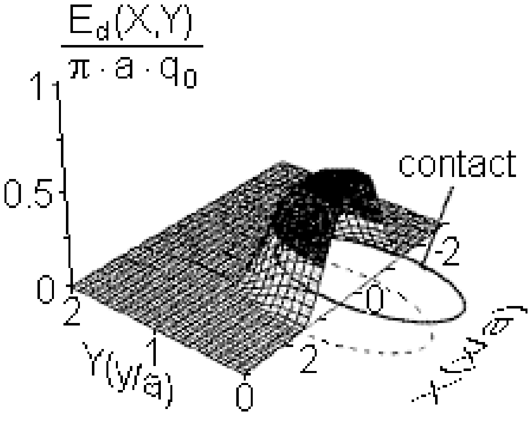

Fig. 1.4: Dissipated energy distribution under fretting gross slip condition (Fouvry, 1996).

1.1.2.2 Crack formation

Under partial slip, the stress tensor of the surface points at each time is determined by $\Sigma(X,Y,Z,t)$. This stress analysis results in several main fatigue approaches. The complex multiaxial Dang Van fatigue model assumes an isotropic hardening behaviour, and characterizes the chance of the crack nucleation by a variable "d" (Dang Van, 1993; Fouvry, 1996):

$$d = \max\left[\frac{\tau(t)}{\beta - \alpha \cdot p(t)}\right] \tag{1.6}$$

where τ is the shear stress, p is the hydrostatic pressure, α and β are parameters as they are shown in Figure 1.5. If the “d” variable is higher than 1, there is a risk of crack nucleation.

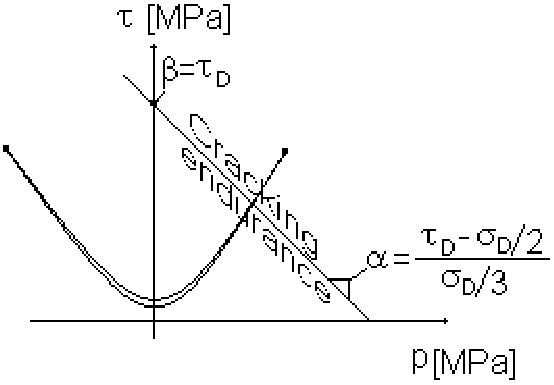

Fig. 1.5: Dang Van fatigue approach (Dang Van, 1993).

We are able to use the classical plain fatigue parameters like bending fatigue limit (σ_D) or shear stress fatigue limit (τ_D) for complex multiaxial stressing with this model, which was tested for cylinder-plane and sphere-plane contacts of low alloy steels (Petiot, 1995). Fouvry et al. showed with fatigue tests and analyses, the highest risk for crack nucleation is at the borders of the contacting surfaces (Figure 1.6, Fouvry, 1996).

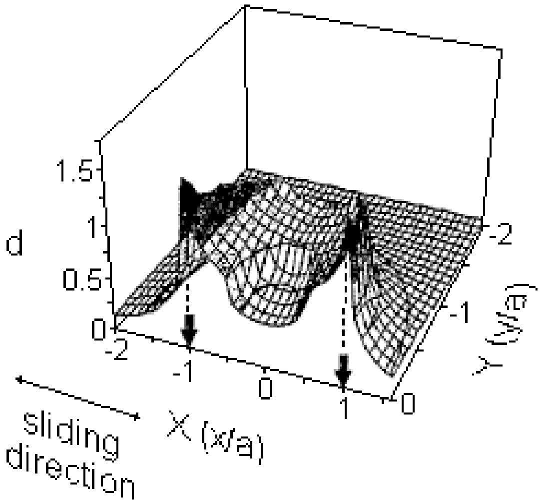

Fig. 1.6: Surface distribution of the Dang Van crack nucleation parameter (Fouvry, 1996).

In this case the stress analysis concentrates on this point (|x|=a, y=z=0) and the material response fretting map has been modified to place the fretting fatigue damage over the Dang Van Fatigue limits as Figure 1.7 shows.

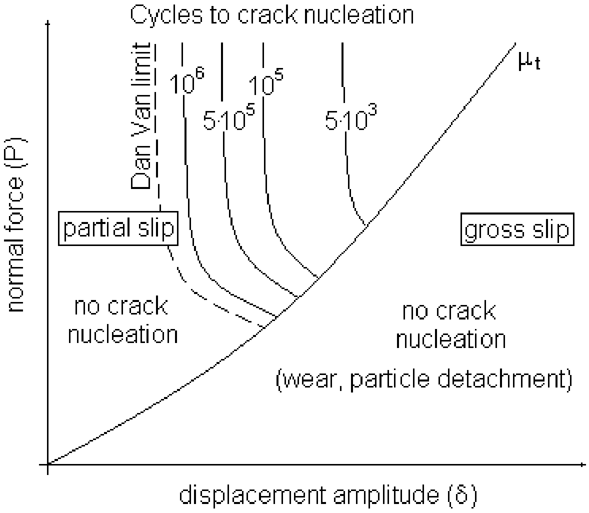

Fig. 1.7: Fatigue life on a Material Response Fretting Map (Fouvry, 1996).

At this border points also the tensile stresses and also the Von Mises σ_{emax} parameter reach their maximum values. The non cracking limit (σ_{eDfret}=1740 MPa – 10^6 cycles) has been determined to be nearly equal to the yield stress (σ_Y=1700 MPa) for steels, but the main cause of crack nucleation was the tensile maximum, compared with the bending fatigue limit (σ_D=1000 MPa) (Fouvry, 1996). From the combination of the Hertzian and the shear stress distributions of the contact area together with the Von Mises stresses, the shear force limit (Q_Y) could be described by the yield stress σ_Y in the slip zone as:

$$Q_Y = \frac{\pi \cdot R}{4 \cdot \mu \cdot E^*} \cdot \frac{{\sigma_Y}^2}{\nu^2 - \nu + 1} \tag{1.7}$$

where R is the radius of the contact cylinder, μ is the friction coefficient, E* is the effective Young’s modulus (Proudhon, 2006).

1.1.3 Fretting behaviour of polymer materials

Polymeric materials are frequently used in engineering applications under sliding contacts (e.g., gears, bushings, sealing), where wear and also fretting are the dominant failure modes. Hence, in addition to the characterization of the fretting wear and fretting fatigue behaviour of metallic materials and fiber reinforced polymer composites, the characterization of the fretting fatigue and wear of unreinforced polymers and also of the elastomers becomes a relevant research task. While the first have already been described by several authors, difficult to find any investigations have been published for the second.

Krichen investigated poly-methylmethacrylate (PMMA) materials under fretting conditions and the Running Condition Fretting Map and a FEM simulation were presented (Krichen, 1996). The same material together with polycarbonate (PC) and polystyrol (PS) has been tested by Stolanski et al. under rolling contact, and they found the same failure modes (crack formation and propagation) as the other authors with steels (Stolanski, 1998). Torsional contact condition issues in the same results, fretting wear with third body and fretting cracking are also described by Briscoe (Briscoe, 1998) and the generated fretting failure images of the specimens surfaces are shown in Figure 1.8 after different cycle numbers (Chateauminois, 2003).

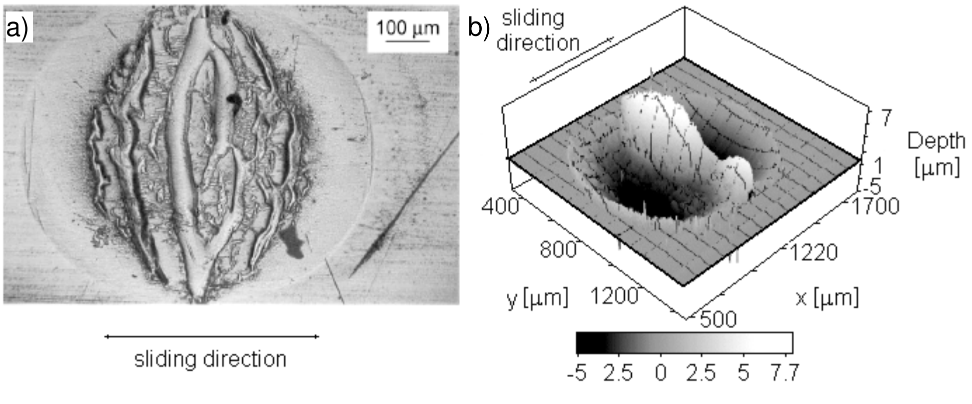

Fig. 1.8: Formation of the PMMA third body agglomerate: after 10^3 cycles (a) and 10^4 cycles (b).

The FEM analysis of the PMMA material showed that micro-cracks can be initiated at the border of the contact zone at the tensile stress maximum, and between the border and the sticking area particle detachment have been observed at the dissipated energy maximum (Krichen, 1999). Gou and Luo investigated twelve different polymer materials (PSU, MCPA, POM, PI, ABS, PC, PA1010, PP, HDPE, UHMWPE, PTFE, PPS) under fretting conditions with ball contact, and 5 different wear behaviours were observed according to their topography and debris shape without any crack formation (Guo, 2002). With epoxy polymers (DGEBA/DDM and DGEBA/DDM/AM) crack initiation and propagation have been produced and modelled (Lamethe, 2003; Duborg, 2003).

Because the friction coefficient plays a basic role in fretting failure, this material parameter was investigated with rubber coatings by Baek (Baek, 2006). The experimental results show four different regions of material behaviour under fretting conditions with increasing cycle number. After the initial phase, a peak value comes in the second region, followed by debris formation with lower COF, and final failure. Due to the stick-slip effect of the TPU material's sliding behaviour; similar surface damage has been observed under wear conditions as by Chateauminois (Figure 1.9).

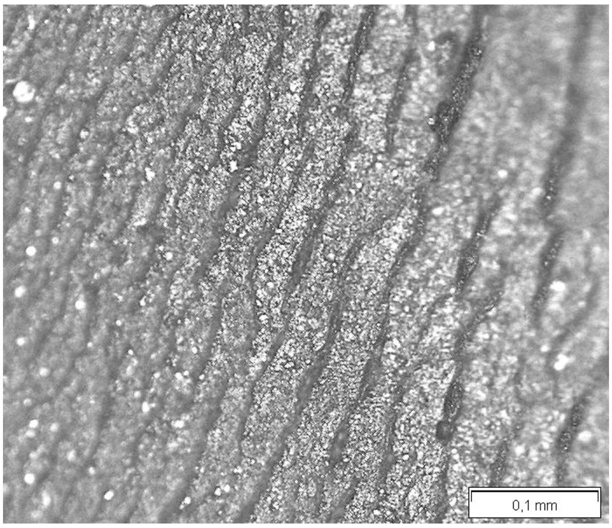

Fig. 1.9: Light microscope image of a TPU specimen surface after wear tests. (PCCL P2.7, 2005)

1.1.4 Materials

Two different elastomeric materials, a thermoplastic Polyurethane (TPU) and a Hydrogenated Nitrile Butadiene Rubber (HNBR) have been investigated in this thesis. Both have special combinations of the material properties. Main characteristics of these elastomers are the high tensile strength, good abrasion resistance and high elasticity. Their thermal ageing and also their chemical resistance at low temperatures open up a wide range of applications for both materials, mainly in the automotive industry.

1.1.4.1 Thermoplastic Polyurethane (TPU)

Thermoplastic polyurethane elastomers (TPUs) were the first homogeneous materials that could be proceed by the commonly used thermoplastic processing methods together with the beneficial features of elastomers due to the multiblock structure of the phase-separated system. The hard segment is formed by the addition of a chain extender, such as butadiene diol, to the isocyanate. The soft segment consists of the flexible polyether or polyester chains that connect the two hard segments (Drobny, 2007). The basic reaction of the polyurethane chemistry is between an isocyanate and a compound containing a hydroxyl (or other groups containing active hydrogen, like NH_2, COOH, etc.) as it is shown in Figure 1.10.

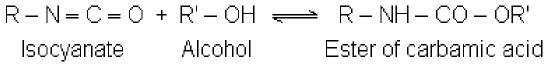

$$\underset{\text{Isocyanate}}{R-N=C=O} + \underset{\text{Alcohol}}{R'-OH} \rightleftharpoons \underset{\text{Ester of carbamic acid}}{R-NH-CO-OR'}$$

Fig. 1.10: Example of the urethane chemical reaction.

The resulting compound is an ester of a carbamic acid, usually called usual “urethane”. TPUs are mostly prepared from long-chain polyols, chain extenders and polyisocyanate. The kind of components and their ratios determine the final material properties, which can vary in a wide range.

1.1.4.2 Hydrogenated Nitrile Butadiene Rubber (HNBR)

Hydrogenated Nitrile Butadiene Rubber (HNBR) belongs to the group of polar and saturated elastomers. HNBR is derived from the unsaturated Nitrile Butadiene Rubber (NBR) as it is shown in Figure 1.11. The unsaturated double bonds within a nitrile's butadiene segments are the main attack sites for heat, chemicals and oxidation. The hydrogenation process reduces the unstable double bonds between carbon atoms in the polymer chain, allowing saturation rates of 85% to 99.9%. The result is a high performance polymer with improved chemical and temperature resistance (Jagels, 2006).

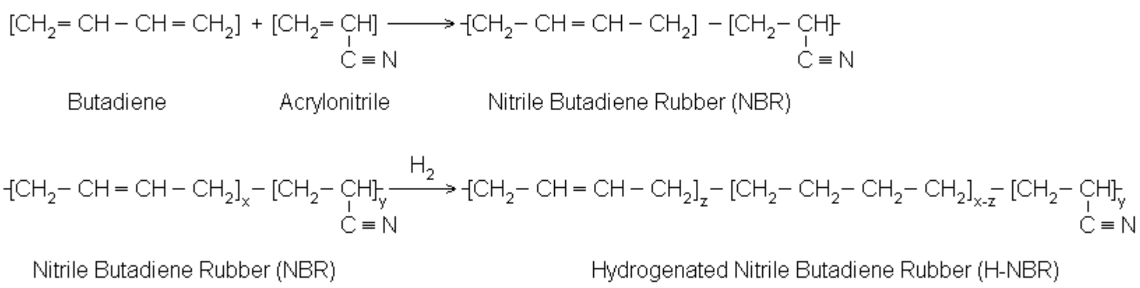

$$[CH_2=CH-CH=CH_2] + [CH_2=\underset{\underset{C\equiv N}{|}}{CH}] \longrightarrow -[CH_2-CH=CH-CH_2]-[CH_2-\underset{\underset{C\equiv N}{|}}{CH}]-$$

$$-[CH_2-CH=CH-CH_2]_x-[CH_2-\underset{\underset{C\equiv N}{|}}{CH}]_y- \xrightarrow{H_2} -[CH_2-CH=CH-CH_2]_z-[CH_2-CH_2-CH_2-CH_2]_{x-z}-[CH_2-\underset{\underset{C\equiv N}{|}}{CH}]_y$$

Fig. 1.11: Production of the HNBR material.

HNBR is mainly used for applications where resistance against mineral oil, high elasticity and good compression set is important, especially in connection with high temperatures.

1.1.5 Objectives

The overall objective of the research work described in this thesis is to characterize the fretting fatigue and the bulk fatigue behaviour of the two selected elastomeric materials by means of experiments and finite element simulations.

The objective of the research work specified in this chapter is to characterize the fretting fatigue behaviour of two selected elastomeric materials and to determine a Running Condition Fretting Map (RCFM) and a Material Response Fretting Map (MRFM) according to the proposal of Fouvry et al. (Vincent, 1992; Fouvry, 1996) for these materials. The methodology used and the main tasks are described as follows:

- Development of a novel fretting fatigue test system based on existing studies and on the available laboratory equipments.
- Determination of ranges for the sliding conditions along with the transition criteria according to Fouvry et al. in the tangential displacement-normal force diagram for the construction of a Running Condition Fretting Map for both elastomeric materials (Fouvry 1996).
- Description of the material response of a thermoset rubber (hydrogenized nitrile butadiene rubber (HNBR) and of a thermoplastic polyurethane elastomer (TPU) for different sliding behaviours by using failure analysis of the contact surfaces with conventional light and confocal microscopy.
- Furthermore, the special features of the contact zone and the multiaxial stress state together with the inherent viscoelastic behaviour of the elastomeric materials make the analysis of the fretting process for elastomers very complex. To get more details about the contact conditions, two-dimensional full-field strain analyses, monotonic compression and creep compression tests have to be performed.
- Finally, to accurately describe the stress state of the contact areas under sliding conditions, finite element simulations which use hyperelastic material models with accurate material data will be performed and subsequently compared with the experimental results.

The final goal is to develop a functional model for the fretting fatigue failure behaviour of various elastomers. This model accounts for the adequate bulk and surface related material properties and their effect on the crack initiation in relation to the local sliding conditions.

1.2 Test method development for fretting fatigue tests of elastomers

Several fretting test systems have been developed depending on the materials investigated, the objectives and the equipments available at the different research groups. There are testing machines with plane (Zhou, 1995), cylinder (Szolwinski, 1996; Farris, 2000) or ball counterparts (Vincent, 1992; .Krichen, 1996; Gou, 2002) resulting in different local stress states on the specimen surfaces.

A novel testing machine using plane-ball contact was built on an electro-dynamic shaker (Brüel & Kjær, 4814 and 4805, Nærum, DK) based on the concept of the fretting system of Matlik (Matlik, 2003). The test system works in displacement control mode, where the power amplifier (B&K type 2707) together with a signal generator controls tangential movement. Due to the difficult management of the amplitude and the stroke in the mid position, an adjustment method should be the next developmental direction.

In the mid-part positioned specimen is pressed from both sides by metal spheres as it is shown in Figure 1.12. The balls have been produced by Kugel Pompel Regina Geider GmbH (Wien, A) with the following properties: R_a=2,7 µm E=93 GPa, and with the nominal diameter of 10 mm.

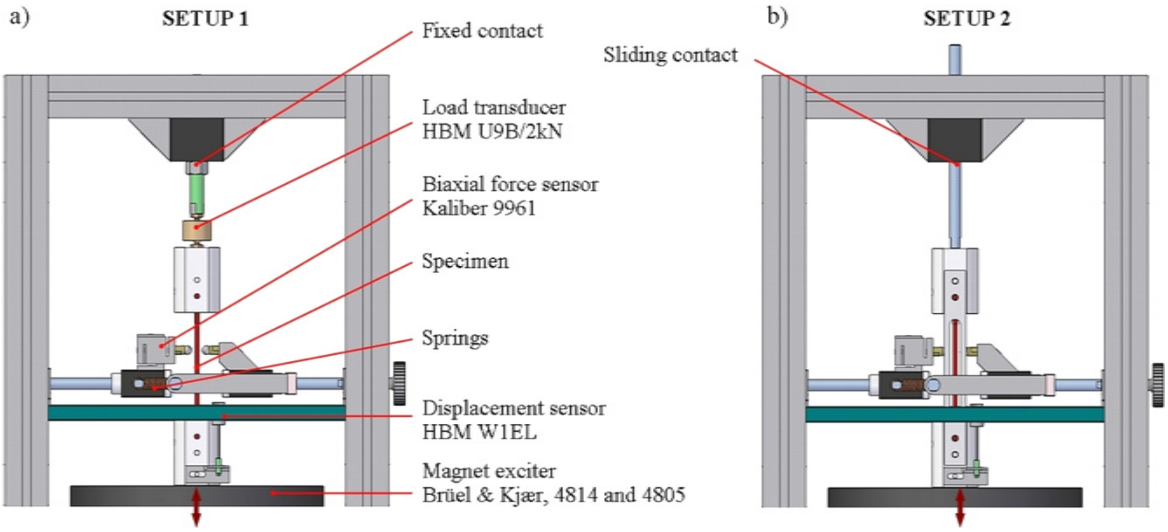

Fig. 1.12: Testing modes and configuration setup 1 (a) and setup 2 (b).

The horizontal force required was realized by two double steel springs (produced by Febrotech GmbH, Halver, D), which have the following features: wire diameter ∅1,4 mm; nominal spring diameter D_a=10,67 mm; length L_0=44,45 mm and spring constant c=2,57 N/mm. They pull both sphere holders together moving on the THK SF10 (H6) and THK LMH-10UU linear bushing-shaft pairs (THK Austria, Pasching, A) reducing the friction to a minimum.

There are two options to clamp the specimens as depicted in Figure 1.12. Similar to the test configuration described by Wittkowsky (Wittkowsky, 1999) the upper part is fixed and the specimen is exposed to a cyclic tensile loading (see setup 1) or the upper and the bottom holder can move simultaneously with the tested material (see setup 2). While the first results in a stretched condition for the material investigated, the second corresponds to a rigid body motion.

The displacement was measured by an inductive sensor (HBM W1EL, Darmstadt, D) and the force in setup 1 by an HBM U9B/2kN (HBM, Darmstadt, D) load transducer. With this configuration we are able to generate different stress states and fretting conditions on the specimen surface. To measure the normal and tangential load simultaneously in the contact area, a biaxial force sensor (Kaliber 9961, Budapest, H) was used. All data are acquired with a Spider 8 DAQ system (HBM) and with the CatMan^R (HBM) software (Figure 1.13).

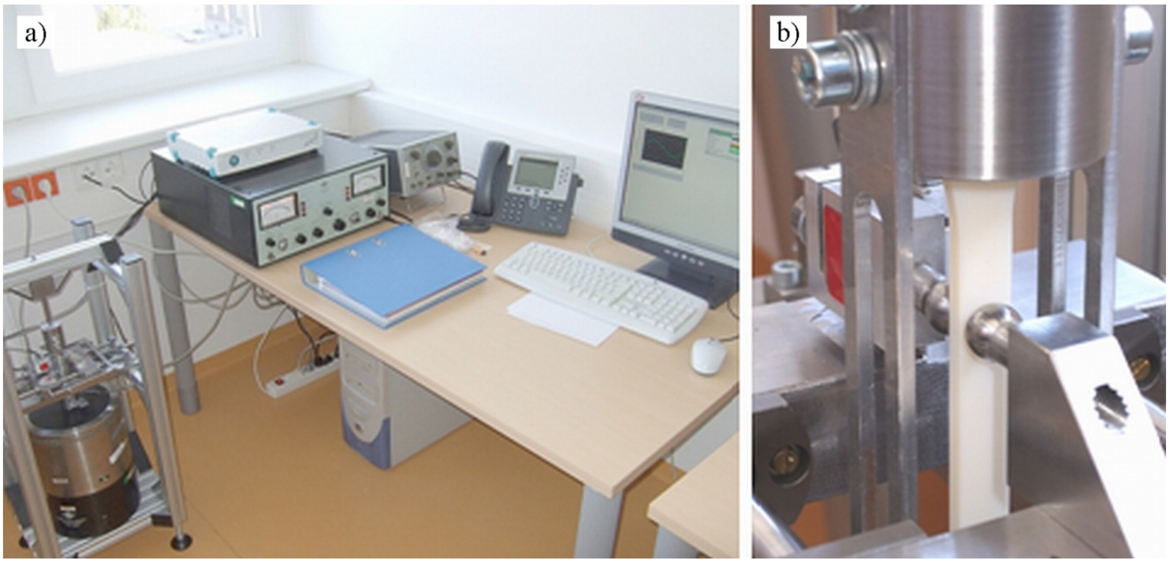

Fig. 1.13: Fretting fatigue test system: instrumentation (a), fixture and local contact in set-up 2 (b).

There are two main difficulties in the process of the measurements. The tangential force measurement is the first one. In the first plans, a biaxial force transducer was built in, but due to the high relative movement of the contact ball on the sensor it was replaced by two standard force sensors. Measuring the tangential force together with the holder, we have to calculate the necessary force for accelerating and braking of the clamps, which is for a harmonic oscillation (Brüel & Kjær, 1998):

$$F_h = m \cdot (a - g) = m \cdot (D \cdot \omega^2 - g) = m \cdot (D \cdot 4 \cdot \pi^2 \cdot f^2 - g) = m \cdot \left(\frac{-d \cdot 4 \cdot \pi^2 \cdot f^2}{\sin(2 \cdot \pi \cdot f \cdot t)} - g \right) \quad (1.8)$$

where m is the holder mass, D is amplitude, $d=-D \cdot \sin\omega \cdot t=-D \cdot \sin 2\pi \cdot f \cdot t$ is the displacement, f is frequency and t is cyclic time.

The usage of two force sensors on the ball sides (one for the normal and one for the tangential force) looks the best solution for this problem.

The ISO Multipurpose Test Specimens (ISO 3167) fit well into the holders of the testing machines. The test specimen is always partitioned into two parts by the central contact area as it is visible in Figure 1.12.b. Depending on the direction of the holder movement there is a part which is under compression and the opposite is under tension at the same time. It could modify the results if the tangential forces are measured on the specimen side.

If the strength of the tested material is relatively high compared to the maximum reachable friction (tangential) forces, the compression and tensile stresses of the specimens have minor influence on fretting. As the ISO form is inefficient the work with elastomers, an alternative specimen holder was developed, as it is shown in Figure 1.14.

The testing region was narrowed by holes with 15 mm diameter to avoid additional deformations outside the process region, the elastomer specimens were reinforced on both sides.

With the fretting fatigue test system developed, the displacement is variable over the range of ±2mm, the maximum frequency is 50Hz and the maximum normal load is 250 N.

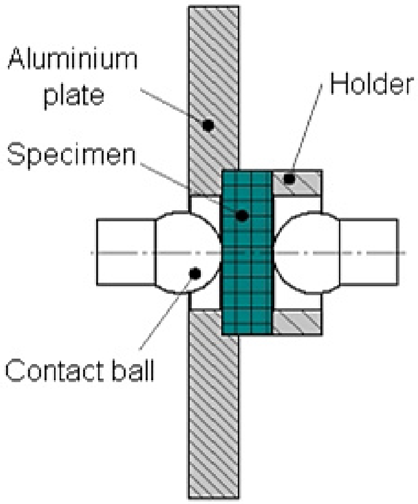

Fig. 1.14: Schematic representation of the contact situation / fretting setup.

1.3 Characterization of the bulk material behaviour and determination of parameters for material models

The investigated materials were produced and the exact composition was determined by the company partner, SKF Economos Austria GmbH (Judenburg, A) with the name of T-Ecopur® (TPU) and SKF Ecorubber-H® (HNBR). The main properties of both elastomers are summarized in Table 1.1.

Material property	DIN Standard	Unit	**T-Ecopur**	**Ecorubber-H**
Colour			Blue	black
Hardness	53505	Shore A	95 ± 2	85 ± 2
Density	EN ISO 1183	g/cm3	1,17	1,22
100% modulus	53504	N/mm2	≥ 12	≥ 10
Tensile strength	53504/53455	N/mm2	≥ 50	≥ 18
Elongation at break	53504/53455	%	≥ 450	≥ 180
Abrasion	ISO 4649	mm^3	15	90
Maximum service temp.		°C	110	150
Minimum service temp.		°C	-50	-25

Table 1.1: Main properties of the investigated elastomers (Economos, 2003).

T-ECOPUR® is modified for deep temperature applications, and should be used under severe climatic conditions and for applications in freezing plants. The material is based on a special polyol with deep glass transition temperature, and the pre-polymer is produced by with polycondensation. After the well-defined relaxation time it is cut to granulate, and its properties are improved by additives. At the end of the drying period the final products are made by injection moulding. To reach their optimal attributes, thermal conditioning between 100 and 110 °C is necessary.

SKF Ecorubber-H® consists Hydrogenated Nitrile Butadiene Rubber (HNBR) with moderate acrylonitrile (CAN). The material is mixed with carbon black and crosslinked by peroxide. The final product is produced by transfer-molding technology. Main applications of the SKF Ecorubber-H® material are special seals and sealing elements for crude oil and natural gas production, rotor seals for the automobile industry, and O-rings.

1.3.1 Test methods

1.3.1.1 Uniaxial tensile-compression tests

A servo hydraulic test system (MTS-858 Tabletop, MTS Systems GmbH, Berlin, D) was used for the uniaxial monotonic measurements under laboratory conditions (temperature 23℃, humidity 50%). The tests were carried out with dumbbell specimens (Ø15x20mm, see Figure 1.15) and with the following parameters:

Testing mode: displacement controlled
Testing speed: 0.01 [mm/s]

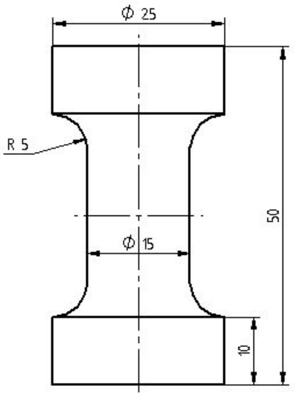

Fig. 1.15: Dumbbell testing specimen for the uniaxial measurements.

The uniaxial stretch and compression response under monotone test conditions are shown in Figure 1.16 up to engineering strains of 250 % and -50% respectively.

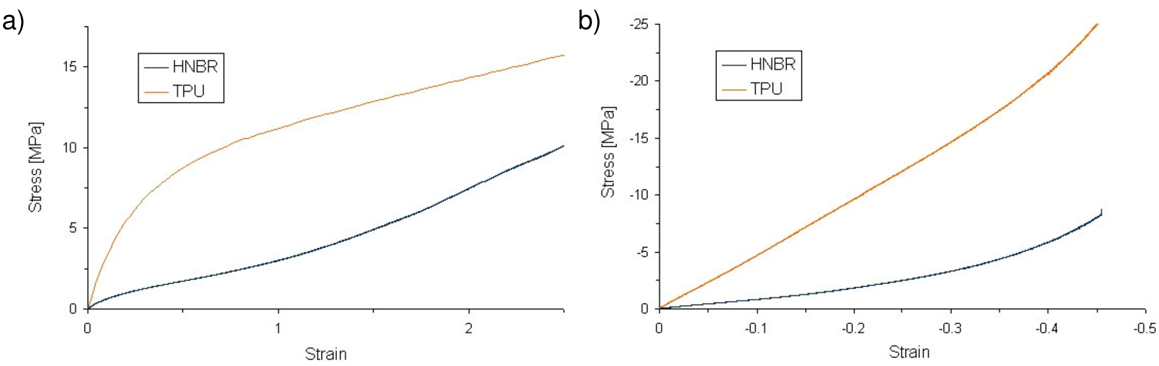

Fig. 1.16: Monotonic uniaxial tensile (a) and compression (b) tests.

The large strain behaviour is non-linear in both cases, because elastomers have an S-shaped stress answer due to the first reversible elastic stage and the final strain hardening resulting from molecular orientation. Overall, the TPU material has higher modulus due to the hard segment of the material and above the 100% value it has a linear relationship between the stress and strain with a somewhat lower modulus. On the other hand, strain hardening of HNBR begins at this strain level (100%), and the stiffness difference between the two materials decrease with higher strain.

1.3.1.2 Dynamic Mechanical Analysis (DMA)

Determination of the dependence of the elastic properties on the test amplitude (with f= 1 Hz) and the frequency (with ε= 0,25) under laboratory conditions (23℃ temperature, 50% humidity) are depicted in Figure 1.17. Both measurements were made on an ElectroForce 3450 test instrument (Bose, MN, USA) using the same specimen as described above.

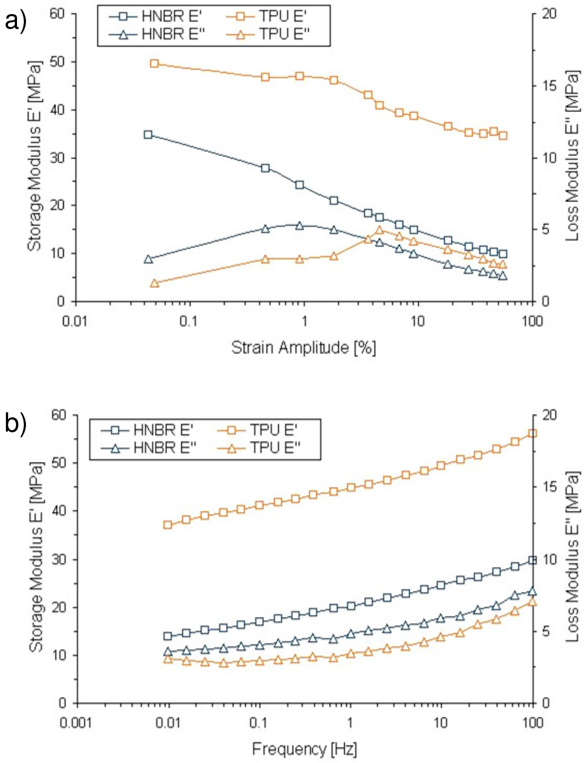

Fig. 1.17: Effect of the strain amplitude (a) and the frequency (b) on the elastomer properties.

The modulus change of the selected materials is shown in Figure 1.18 as a function of the temperature under the conditions f= 2 Hz and ε= 0,1 %.

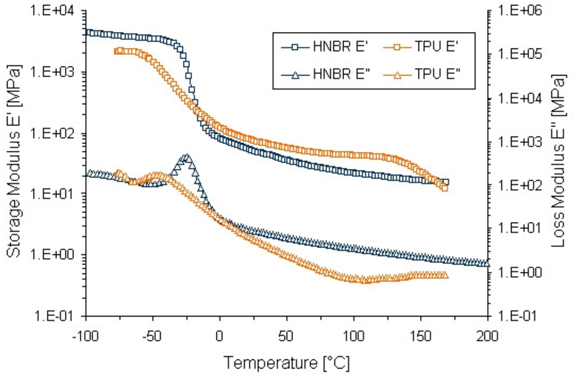

Fig. 1.18: Temperature dependent DMA curves.

1.3.2 Hyperelastic material models

For finite element modelling of the different test methods described in the following chapters of this thesis, the Ogden hyperelastic material model has been evaluated for both materials (Ogden, 1972). Like the other hyperelastic models, this model uses also the strain energy density function to describe the non-linear stress-strain behavior of the isotropic, incompressible and strain rate independent material, with the following equation:

$$W = (\lambda_1 \lambda_2 \lambda_3) = \sum_{i=1}^{n} \frac{\mu_i}{\alpha_i} \left(\lambda_1^{\alpha_i} + \lambda_2^{\alpha_i} + \lambda_3^{\alpha_i} - 3 \right) \qquad (1.9)$$

where λ_j (j=1,2,3) are the principal stretches, and μ_i, α_i are material constants. With three-term approximation, n=3, the material behavior can be described very accurately (Table 1.2).

TPU			**HNBR**		
i	μ_i	α_i	i	μ_i	α_i
1	8.575	0.907	1	2.329	1.340
2	0.003	6.336	2	0.021	5.989
3	0.029	-3.256	3	1.000	-3.473

Table 1.2: Material parameters of the Ogden third order hyperelastic model.

The evaluated models are stable for all basic stress states (uniaxial, biaxial, planar tension and compression), and the differences between the two materials are shown under uniaxial stretching in Figure 1.19.

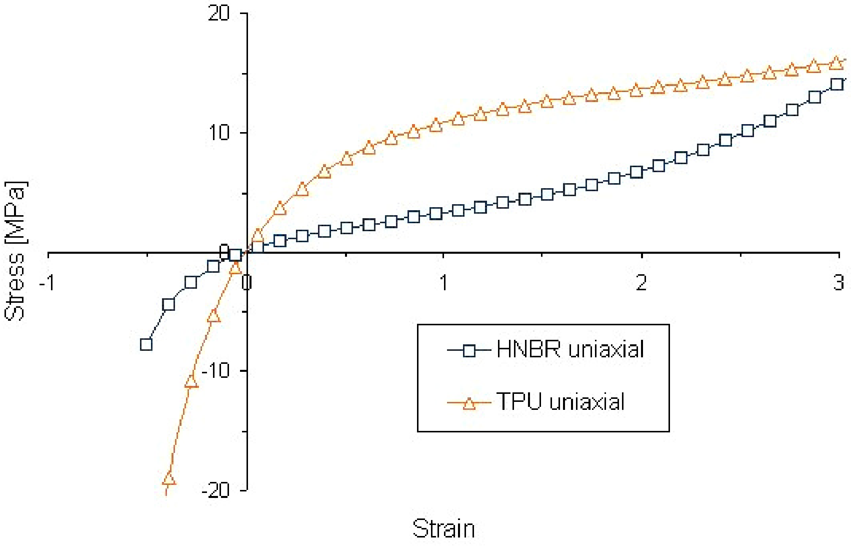

Fig. 1.19: Uniaxial stress-strain diagram of the Ogden hyperelastic models.

Description of material softening is possible with the built-in “Mullins” routine in the Abaqus FE software tool (version 6.7, Simulia, USA). For model evaluation, monotonic strain-controlled tests were performed up to 10 cycles on different strain levels with 0.01 mm/s testing speed. Nominal stress-strain curves are shown for both materials in Figure 1.20.

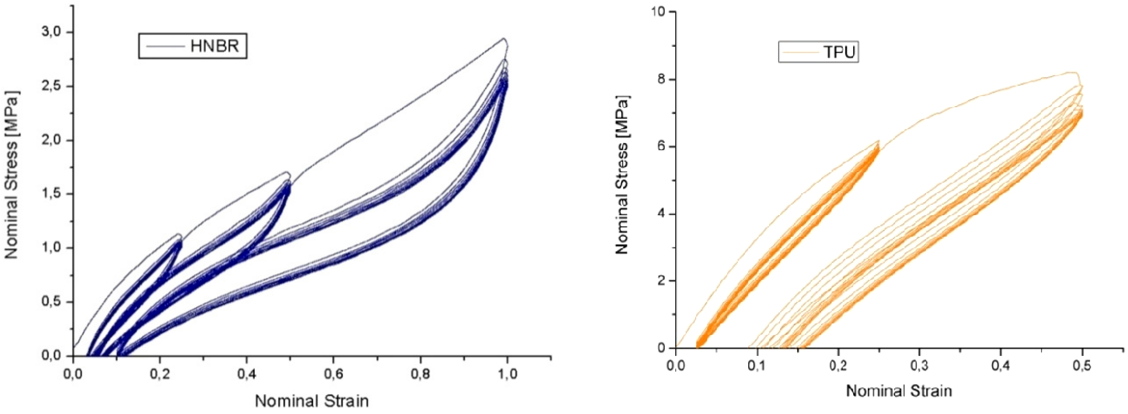

Fig. 1.20: Material softening in 10 cycles at strains of 0.25, 0.5 and 1 for HNBR (a) and TPU (b).

Mullins effect is described in Abaqus as damage parameter (η) of the deviatoric part of strain energy density ($\dot{U}_{dev}$) with the following formula:

$$\eta = 1 - \frac{1}{r} erf\left(\frac{U_{dev}^{m} - \dot{U}_{dev}}{m + \beta \cdot U_{dev}^{m}}\right) \tag{1.10}$$

where U_{dev}^{m} is the maximum value of $\dot{U}_{dev}$ at a material point during its deformation history; r, β, and m are material parameters; and erf(x) is the error function. The determined Mullins parameters are:

	TPU	**HNBR**
r	1.181	1.487
m	0.477	0.084
β	0.183	0.276

Table 1.3: Parameters of the Mullins model.

The evaluated model responses are shown in Figure 1.21. With Mullins effect the material stress response is the same as the Ogden model if no unloading was passed before at the given strain. Otherwise the upload corresponds with the unload curve till the maximum strain level in the material element history.

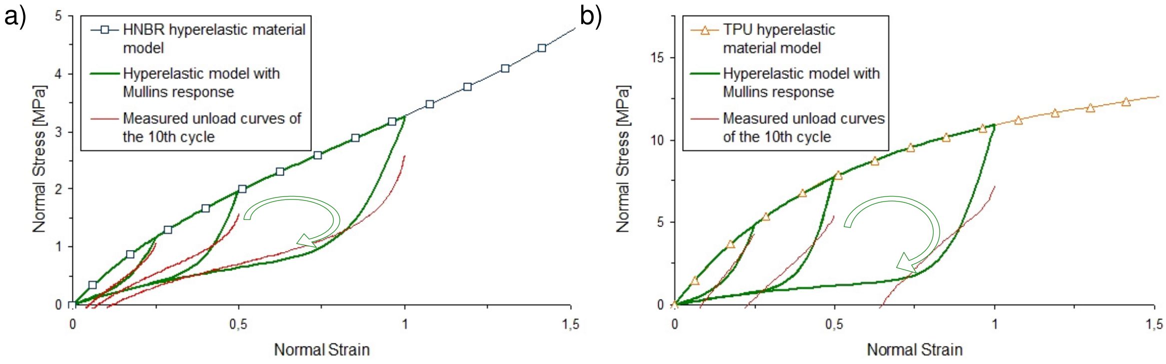

Fig. 1.21: Mullins response of the HNBR (a) and TPU (b) material model.

As the green curves show, this built-in Mullins routine is usable to define one kind of material softening, but the model of the commercial Abaqus software has some disadvantages in the usage for elastomer modelling:

- the material has to be free from stresses at ε=0 all the time, and
- it can produce hysteresis curve only in the first cycle for a given strain.

1.4 Fretting fatigue experiments and finite element analysis

Based on the results of preliminary experiments, set-up 2 was used in all further experiments of this study. In the first part of these experiments the sliding conditions were determined under different normal loads which were varied from 5 up to 50 N, at the frequency of 3 Hz, at room temperature and applying tangential displacement amplitudes from 0,025 to 1 mm. The aim of these short-term experiments (duration was less than 1 min) was to determine the influence of the normal load and tangential displacement on the sliding conditions for HNBR and for TPU and to define the corresponding sliding regimes.

Furthermore, 2D full-field strain analysis was performed together with creep compression and monotonic compression tests on the two materials. Moreover, local stress-strain states of the contact areas were determined by a finite element analysis and the simulations were compared with the results of the measurements of the sliding regimes.

Finally, in the second part the long-term fretting failure behaviour of the two elastomers was investigated under 30 N normal load and with tangential sliding displacements up to 1 mm. Failure analysis of the worn contact was carried out by conventional and by confocal microscopy and a functional model was proposed for both elastomer types investigated.

1.4.1 Determination of the sliding conditions and regimes

To define sliding conditions for both materials, the tangential load was measured as a function of the normal load and the displacement amplitude, and the hysteresis curves of the materials were plotted. In the process of the hysteresis cycle analysis, we have to attend to some special conditions of this test method. Depending on the position and on the movements, the measured tangential load consists not only of the friction load. During the fretting measurement of steel materials, the unwanted strain of the test fixture (compliance of the test system) plays an important role (Fouvry, 1996). However, for elastomers another problem exists: below and above the contact area there are always a strained and a compressed zone, which produce measurable hysteresis curves with the smallest displacements also. Determination of an exact value of the friction force is not simple with these parameters, because the ball is pushed deeply into the surface, which has a rising effect on the measured values together with a change of the velocity. Due to these two influences, after the curves reach the sticking force of that displacement range, no well determinable peak value (sticking) or constants load (sliding) was observed.

The measured hysteresis curves were corrected by the subtraction of the inertial forces. These corrected hysteretic curves of the HNBR specimens are shown with constant normal load in Fig. 1.22a and with constant displacement amplitude in Figure 1.22b. Some indications of gross slip like behaviour are observed on both diagrams. Using 10 N normal loads a material specific tangential sliding displacement was determined with about 0,2 mm amplitude. The same effect is visible under at 0,3 mm amplitude when the value of the normal load was reduced from 30 to 20 N (see Fig 1.22b).

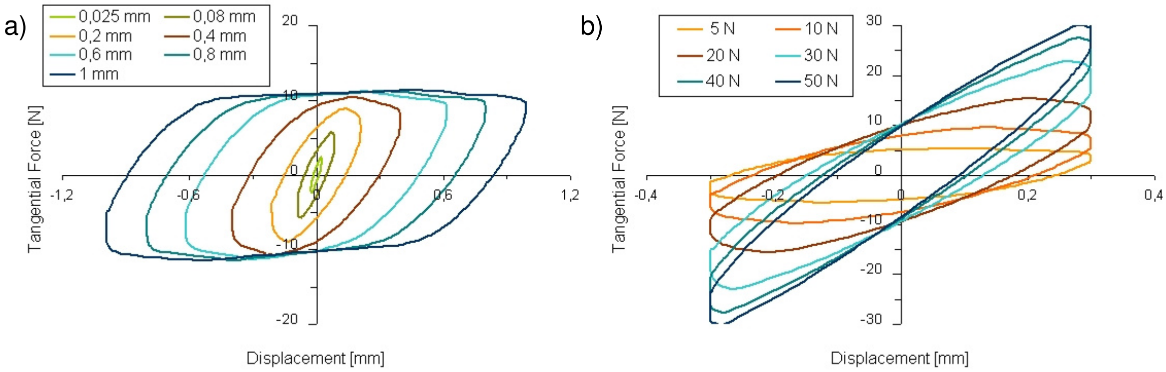

Fig. 1.22: Tangential force-displacement hysteretic curves of HNBR material under constant normal load of 10 N (a) and at constant amplitude of 0.3 mm (b).

The same diagrams are shown in Figure 1.23 for the TPU material. Comparing these curves with Figure 1.22 the following observations are made:

- The same normal force results in higher tangential force values for HNBR.
- The same tangential displacement results in similar tangential force values for both materials, but significantly higher hysteresis loops for TPU.

- Due to the complexity of the contact, these hysteretic curves consist of several separated regimes.

These regimes will be used for the detailed analysis of the sliding process in terms of an RCFM curve.

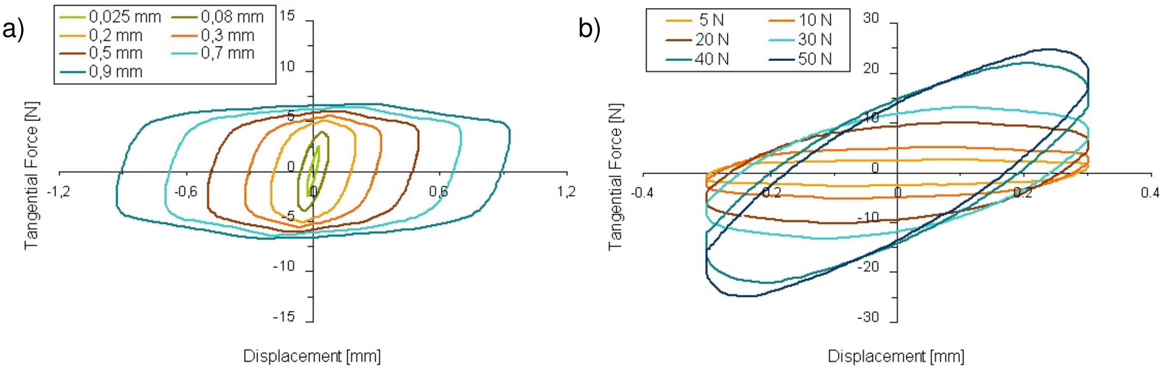

Fig. 1.23: Tangential force-displacement hysteretic curves of TPU material under constant normal load of 10 N (a) and at constant amplitude of 0.3 mm (b).

To construct the RCFMs of both materials, six different normal loads were selected and the displacement amplitudes were changed from 0.1 to 1 mm. The schematic representation of the data reduction method is shown in Figures 1.24 and 1.25.

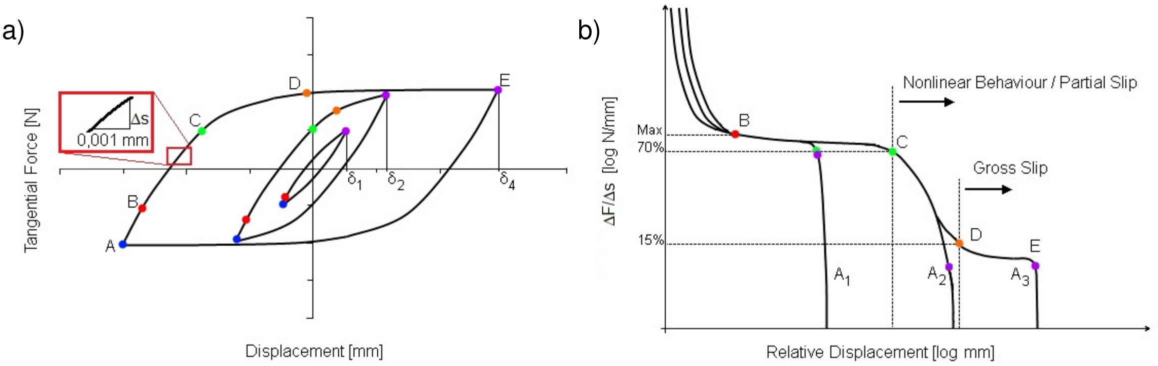

Fig. 1.24: Limit points of the linear, the non linear, and the sliding regimes on the hysteresis curves (a) and determination of these points on the ΔF/Δs-displacement diagram (b).

The slope of the tangential force-displacement curve (ΔF/Δs) was taken from the measured curves (e.g., from Figure 1.22a) after every 0,001 mm tangential movement of the specimen at a specific normal load and displacement amplitude (see in Figure 1.24a). The initial part (between points A and B) is followed by a linear behaviour (from B to C or E), where the force tangent is nearly constant as it is shown in Figure 1.24b.

If a non-linear part of the curve is observed (e.g., from point C to D), the slope value drops down on the same line independently from the displacement amplitude. In the region of the sliding contact expected it becomes almost zero (e.g., from point D to E). The maximum value of the displacement amplitude is defined by the point E, where the slope changes its sign.

The sliding regions have been determined on the exponential fits of the force tangent curves between the B and D points. The limit of the nonlinear behaviour is defined by 30% drop of the maximum force slope value. In the same way the limits of the gross slip with 85% value decrease are selected (see in Figure 1.25a). With these points we are able to draw material specific RCFM curves (Fig 1.25b).

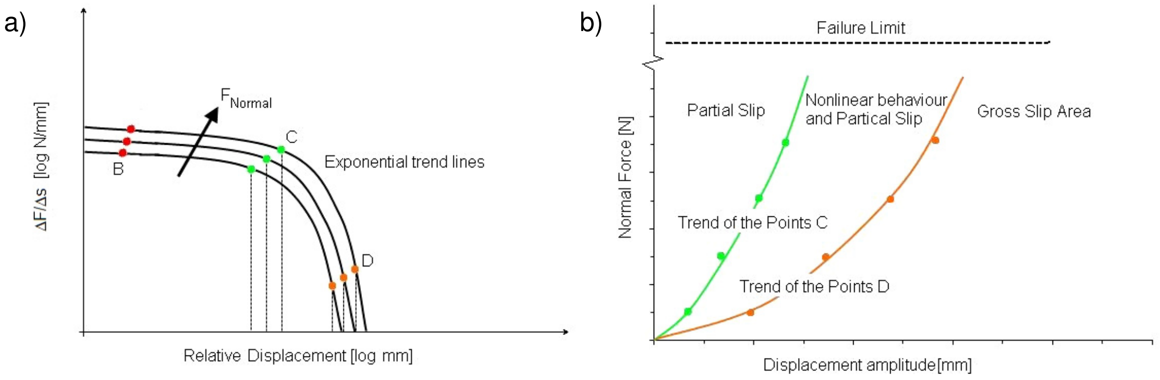

Fig. 1.25: Exponential trend lines of the force tangent (a) and the evaluation of the Running Condition Fretting Map (b).

A measured change of the force slope under 10 N normal load together with an exponential trend line and the position of the calculated C and D points is shown in Figure 1.26. To determine the Running Condition Fretting Map, the normal load and the displacement amplitude were changed. Based on the measured values, three regions were defined:

- Assuming linear elastic material behaviour, where the tangential forces are directly proportional to the displacements, the region of Partial slip was determined.

- The second region describes that displacement range at the given normal load, where the relationship between the tangential force and the specimen movement is not linear.
- Gross slip (sliding) is that region, where the tangential forces have a well defined maximum and minimum.

Furthermore, it has to be noted here that the friction coefficient has a huge dependence not only on the environment (temperature, wear type, velocity, counterpart, geometry etc.), but also on the testing time or wear distance (Verheyde, 2009; Gódor, 2009).

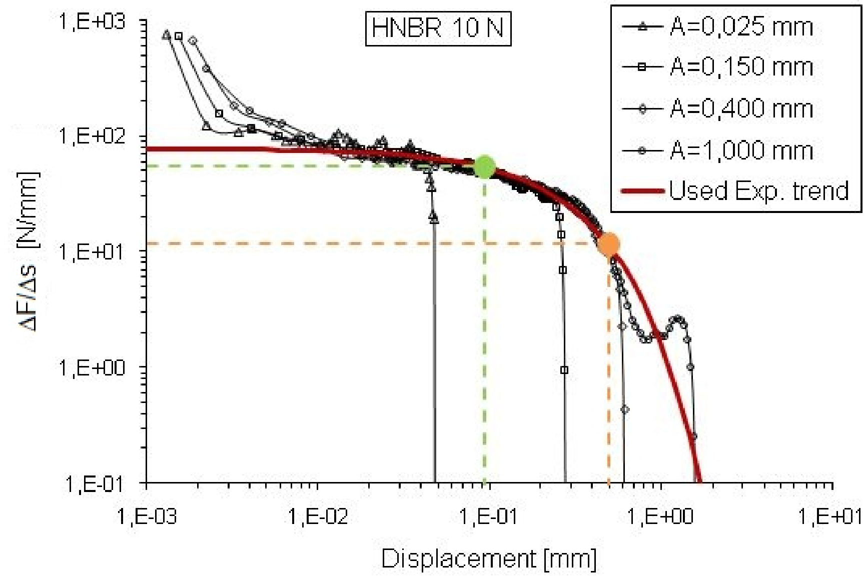

Fig. 1.26: Slope values of the tangential force-displacement curves of the HNBR material under 10N normal load with four different displacement amplitudes.

The Running Condition Fretting Maps determined for HNBR and TPU materials are shown in Figure 1.27. Due to the higher modulus of the TPU materials both limit curves of the partial slip and the nonlinear behaviour belong to lower displacements at the same normal force level. Furthermore, due to the lower coefficient of friction of TPU, the gross slip area is significantly larger than in the case of HNBR.

Determination of the widely used Running Condition Fretting Maps in this chapter was based on the method of the tangential force change as a function of the tangential displacement for both elastomers investigated. With the described fretting regimes, the testing parameters of the different material responses can be predicted.

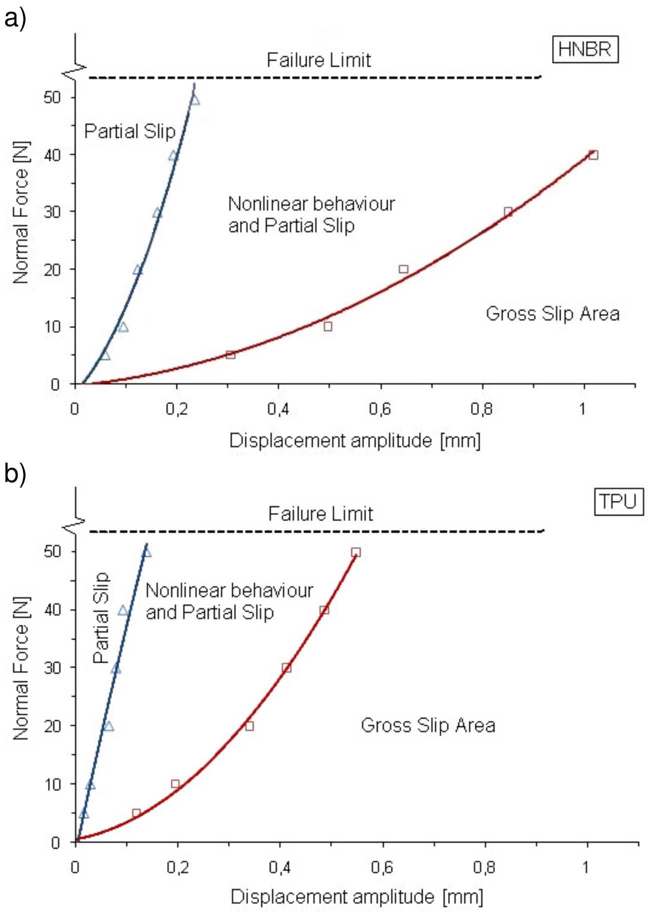

Fig. 1.27: Running Condition Fretting Map of the HNBR (a) and TPU (b) materials.

1.4.2 Characterization of the normal deformation behaviour under double side sphere contact

1.4.2.1 2D strain analysis

Additional measurements were performed on a Universal-Microtribometer (UMT-2, CETR, USA) for characterizing the contact zones and for determining the local strain distributions for the two elastomeric materials. Two cylinders with the same diameter as the balls of the fretting experiments were pressed together and a full field 2D strain analysis was carried out on the sides of the elastomer specimens. The strain distribution in the HNBR specimen is shown in the horizontal (x) and in the vertical direction (y) under 400 N load in Figure 1.28. Because of the low stiffness of the material, here the two contact regions blend into each other, producing a nearly constant ε_y local strain distribution across the specimen.

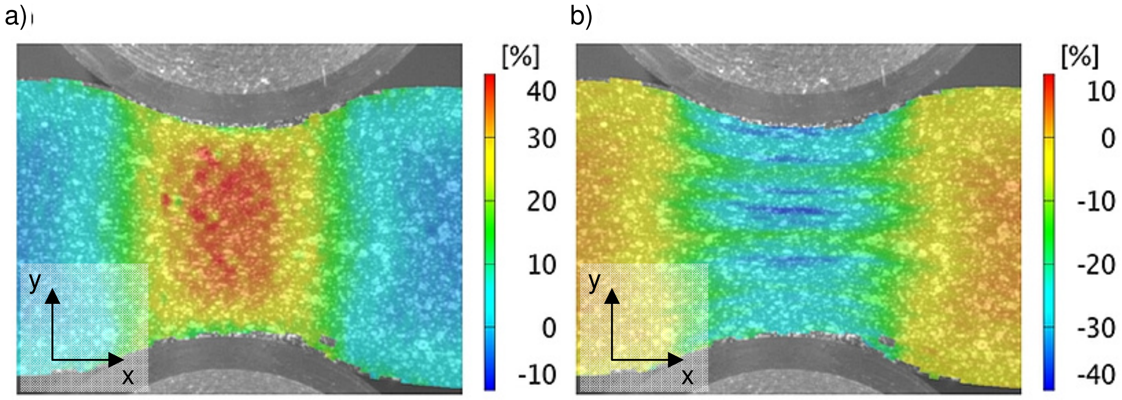

Fig. 1.28: Strain distribution of the HNBR specimen: ε_x (a) and ε_y (b).

The strain distribution of the TPU specimen is shown in the horizontal (x) and in the vertical direction (y) under the same load in Figure 1.29. The maximum local strain in the direction of the applied pressure (ε_y) is in the contact area and decreases to the middle of the specimen (see Figure 1.29b).

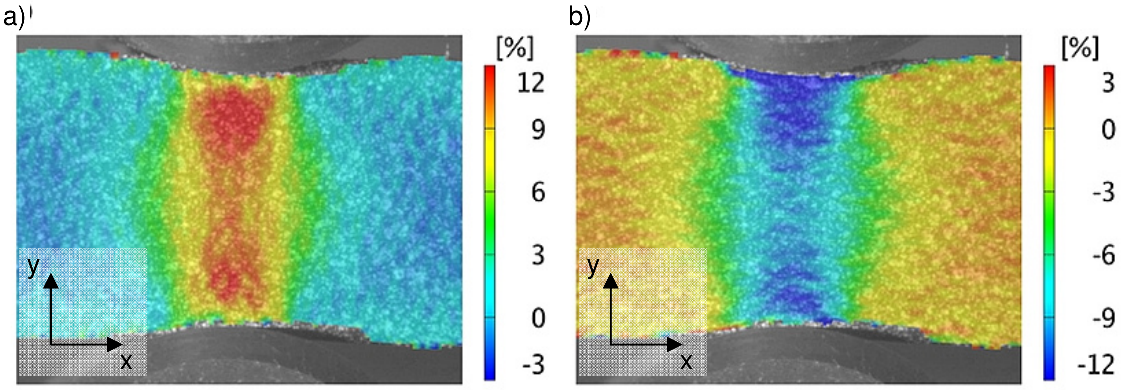

Fig. 1.29: Strain distribution of the TPU specimen: ε_x (a) and ε_y (b).

These strain distributions in the contacting materials represent the behaviour under unidirectional loading. Due to the friction between the cylinder and the rubber plate, shear stresses can already develop uniaxial loading conditions. The development of the shear strains can be deduced from the change of the horizontal strain component, ε_x across the specimen in the images shown below.

The main result of these investigations is the comparison of the material behavior under multiaxial contact loading situations. As clearly seen in Figures 1.28 and 1.29 the HNBR reveals higher indentation under the same load as TPU. This difference also shows in the significantly higher ε_x and ε_y strain components in the full-field strain analysis images.

1.4.2.2 Compression and creep tests

To characterize contact configuration realized in the fretting testing machine, further measurements were performed. To determine the contact mechanical behaviour monotonic compression and creep compression tests were performed on both materials using the tribometer system. The set-up corresponds to the existing fretting fatigue test system: the metal balls have the same diameter, and the material properties and dimensions of the specimens are also the same as in the fretting measurements. Hysteretic normal force-displacement curves of the monotonic compression tests by steel balls are shown in Fig. 1.30a.

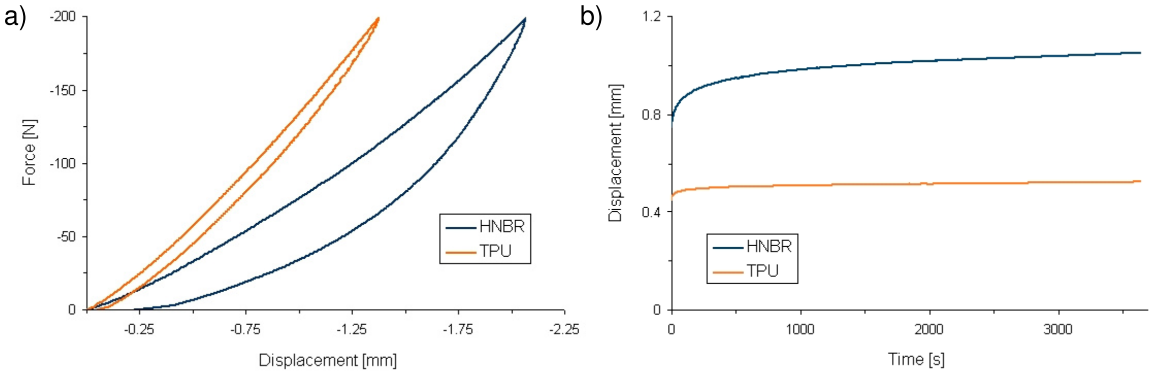

Fig. 1.30: Compression (a) and creep (b) tests of the HNBR and TPU materials.

The results of the creep measurement with 50 N normal load and with 1 hour testing time are seen in Fig. 1.30b. As expected, both elastomer types reveal time dependent deformation behaviour, and HNBR shows significantly higher local indentation displacement values than TPU.

1.4.2.3 Finite element simulation

To describe the strain distributions and to localize the maximum stresses, the test was simulated in the Abaqus (version 6.7, Simulia, USA) finite element simulation software (Figure 1.31), using the parameters calculated for an Ogden type hyperelastic material model in section 1.3.2.

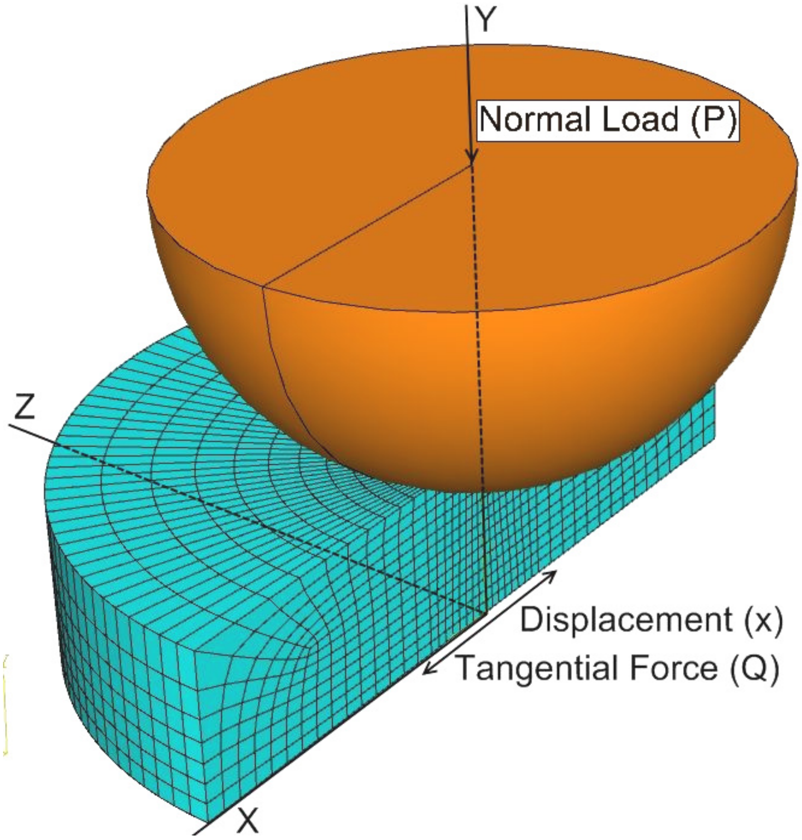

Fig. 1.31: Fretting model for the finite element simulations.

The contact was defined as “hard contact” with 30 N normal load, and the tangential behaviour with “penalty” friction, where the Coefficient of Friction (COF) was 0,95 for HNBR and 0,55 for TPU.

Figure 1.32 shows schematically the steps and phases of the simulations.

- The first step (Step I) is an initial period, where the contact between the ball and the specimen was built up in displacement control mode.
- Step II sets the required normal load of the test in force controlled mode.
- The tangential oscillation of the elastomeric specimen is in Step III. Within Step III Phase 2 was defined after the first minimum of the tangential cycle and will be closely investigated in this chapter.

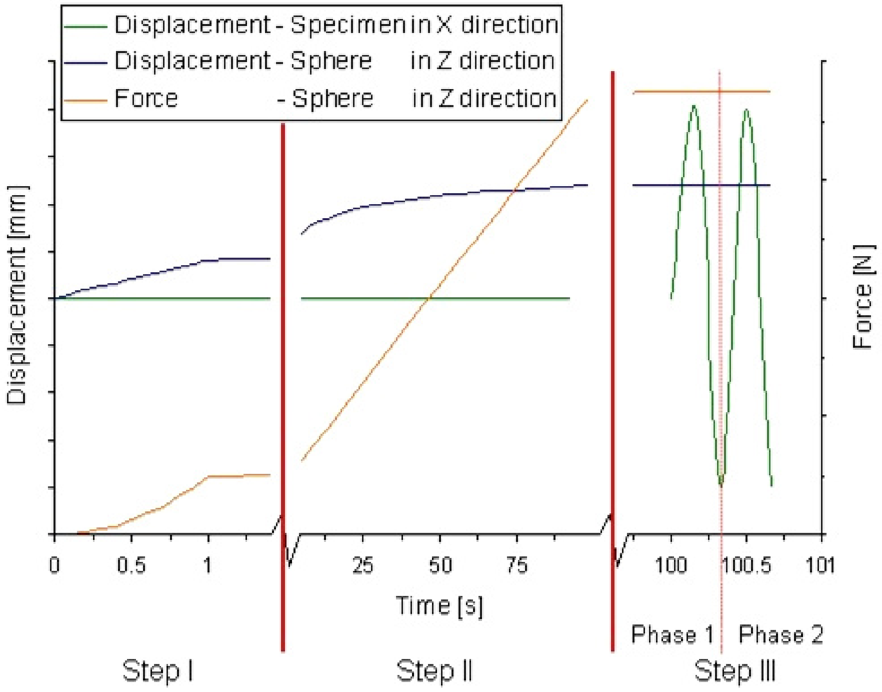

Fig. 1.32: Configuration of the finite element simulation steps.

The simulated results of three amplitudes are compared with the real test force-displacement curves in Figure 1.33. Because the material model does not contain hysteresis, there is always an offset between the real and the measured loading and unloading curves. Furthermore, the slopes of the tangential force-displacement curves reveal also differences, which reflect the difference between the real shear modulus and the shear modulus used in the material model.

The cross symbols located on the simulated hysteretic curves represent selected stages of the simulation. These stages are depicted in Figure 1.34 and 1.35.

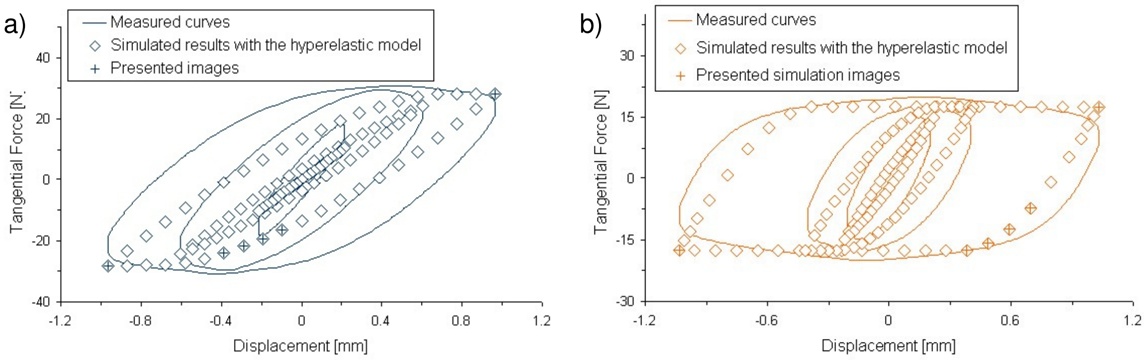

Fig. 1.33: Comparison of the measured and the simulated tangential force-displacement response for HNBR (a) and TPU (b) with three different displacement amplitudes.

The points at the upper right end of the curves correspond to Figure 1.34a and 1-35a. Due to the use of a time-independent hyperelastic material model, the simulation with the highest displacement amplitude describes also the stages of those stress-strain distributions where no gross slip occurs. The von Mises stresses of the HNBR material are shown in the image series of Figure 1.34.

The first position of one way movement after a gross slip is visible in Figure 1.34a, where the stretching and the shear stresses of the pulled side of the specimen are relevant. The friction forces produce a shear (τ_{xy}) concentration as a ring form in Fig. 1.34b, c and d at the limit of the gross slip region (Tur, 2003). The complete surface can not slide together, there is always a region in the contact area which is sticking. in spite of that, the tangential force is constant independently from the movement magnitude (Figure 1.34f). The maxima of the von Mises stresses have different values on the images: while the red element means ~5MPa on Figure 1.34b, and at the peak displacement points (Figure 1.34a and f) it is ~8.1MPa.

Similar behaviour of the TPU material is presented in the pictures of Figure 1.35. The initial state after a gross slip period is visible in Figure 1.35a, where the pressures with the stretching forces are dominant. Because of the friction forces the shear (τ_{xy}) concentration is observable in Fig. 1.35b on the Z directional contact edges, parallel with the specimen movement.

The next two images (Figure 1.35 c and d) also show a circle formulation of the shear stresses on the contact border at the limit of the gross slip region. The contact area has smaller diameter, but the von Misses stresses are less concentrated in all position compared to the HNBR material model. The maximum (red) value means ~6.8MPa in Figure 1.35e and 5.1MPa in Figure 1.35b.

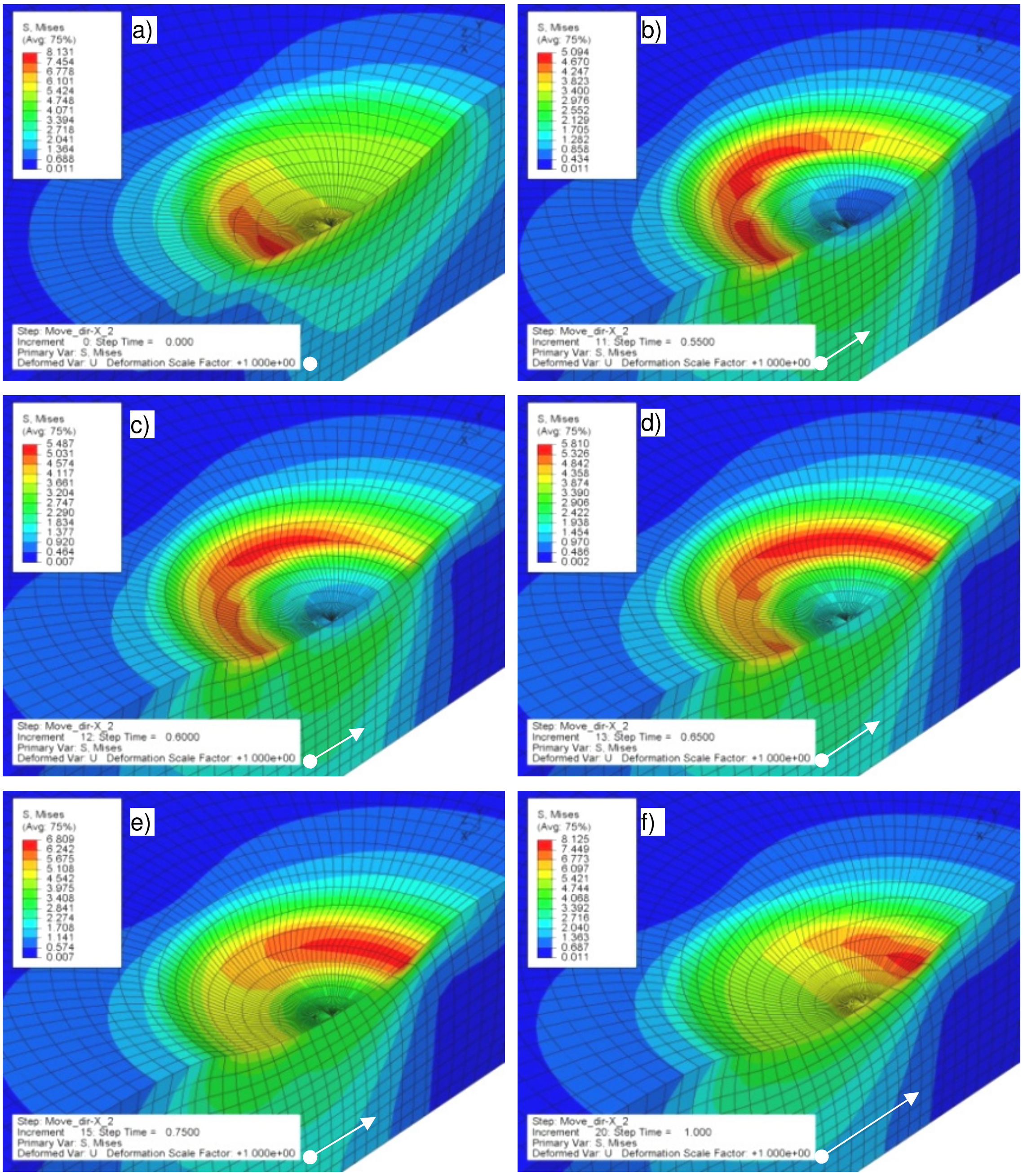

Fig. 1.34: Mises stress in the Abaqus simulation of HNBR material at different displacement points: 1mm (a), -0.1mm (b), -0.2mm (c), -0.3mm (d), -0.5mm (e), -1mm (f).

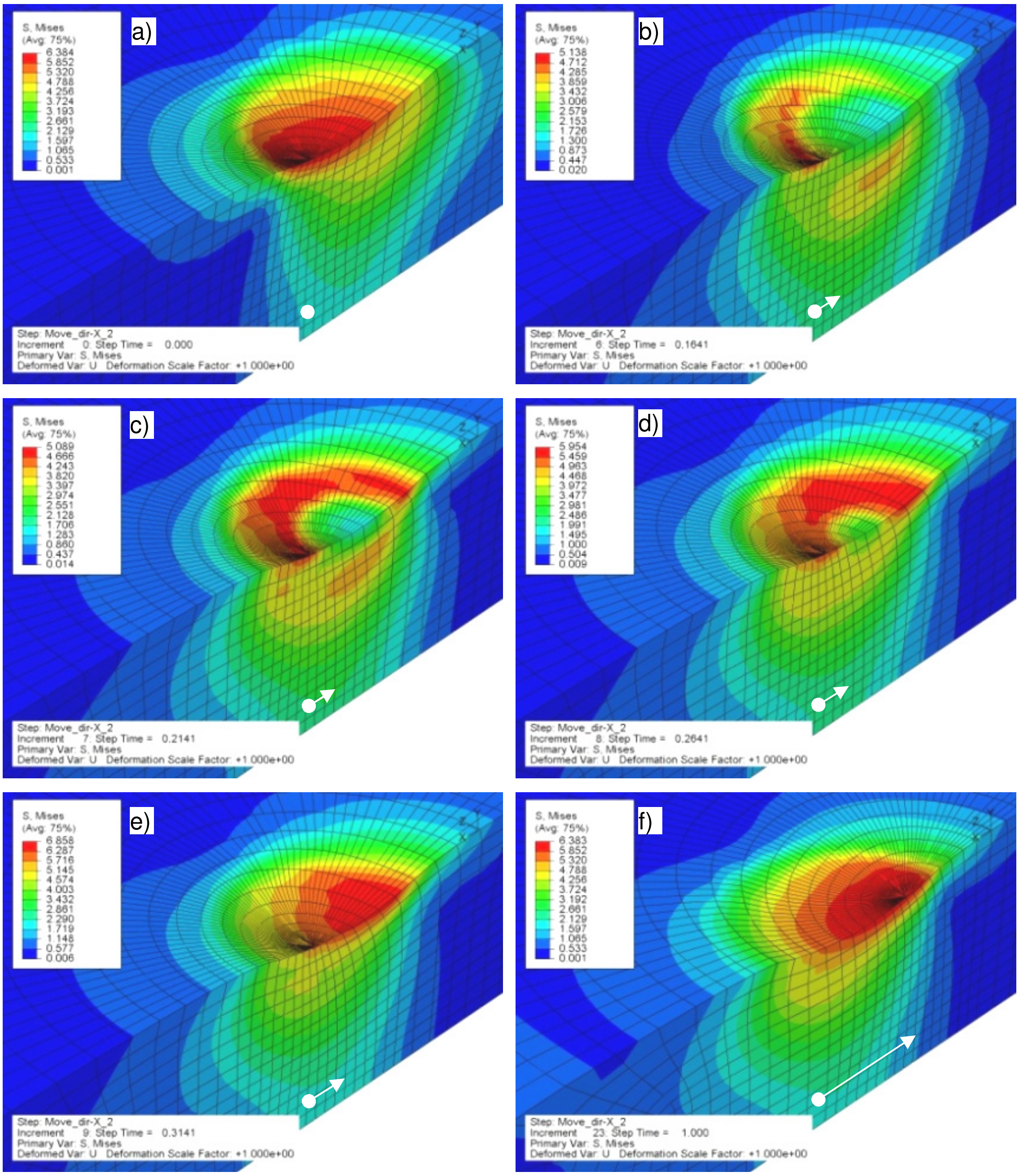

Fig. 1.35: Mises stress in the Abaqus simulation of TPU material at different displacement points: 1mm (a), 0,7mm (b), 0,6mm (c), 0,5mm (d), 0,38mm (e), -1mm (f).

Two different methods have been used to determine the stress-strain states for both materials.

- In the first part the middle line of the contact area in the movement direction (X axis) was investigated, and the contact lengths and the main stress changes were plotted and compared.

- Secondly three well defined points were chosen in the contact area and their stress states are shown depending on the displacement amplitude as a function of time (1 cycle).

The contour of the contact surface of the HNBR material simulation is shown in Figure 1.36a and b at the maximum displacement points. The changing of the contact area between these peak positions is visible in Figure 1.36c. The distance between the contact points, a, is seen in Figure 1.36c and is approximately 3.6mm during the specimen movement (tangential displacement range of 2mm). A 0.8mm shift of the contact edges was observed, dividing the investigated area into two sections, one of which is always in contact with the sphere, and the second where the contact is only periodical.

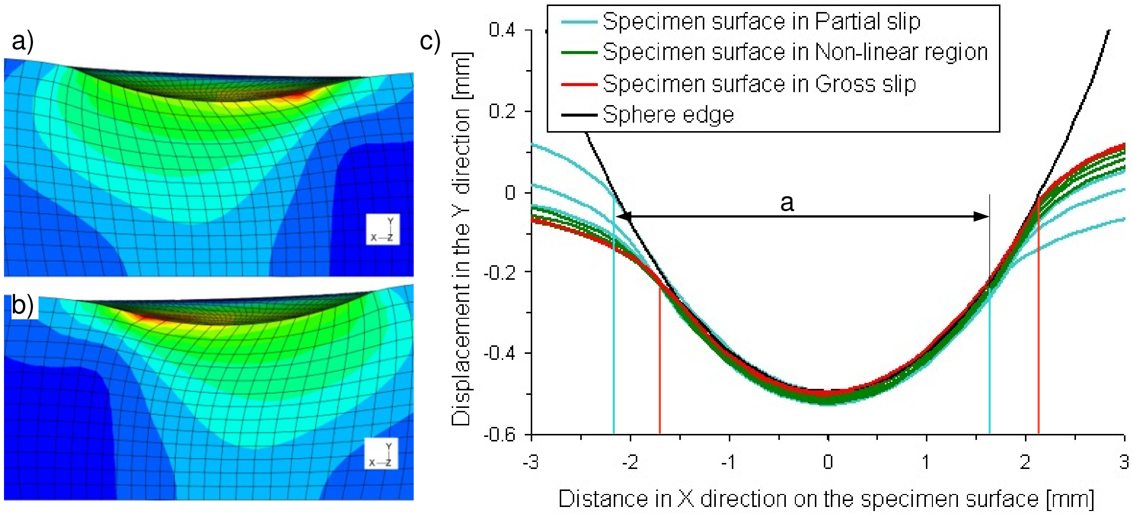

Fig. 1.36: Start (a) and end (b) position of the investigated HNBR simulation and the change of the contacting areas (c) under 2 mm specimen movement (A = 1 mm).

The same evaluations are shown for the TPU material in Figure 1.37. Due to the larger stiffness, the distance between the contact points is smaller, a=3.1mm, and stays nearly at the same position around the steel balls. Due to the smaller indentation depth of the sphere, the specimen needs less force to move. Consequently, the von Mises stress has lower values at the tangential displacement maximum with a lower gradient of the stress concentration compared to the HNBR simulation. This phenomenon can be clearly seen with size of red coloured rings, which are larger for TPU.

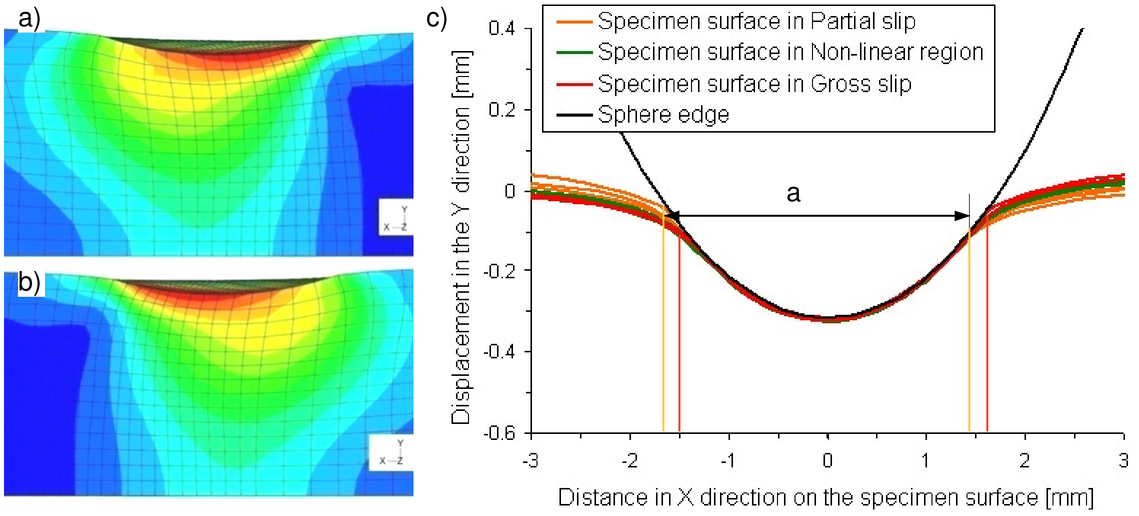

Fig. 1.37: Start (a) and end (b) position of the investigated TPU simulation and the change of the contacting areas (c) under 2 mm specimen movement (A = 1 mm).

Similar to Figures 1.34 and 1.35, the stress components σ_x and the shear stress components τ_{xy}, τ_{xz} were also determined in the simulation. A representative example of these results is shown in Figure 1.38. The slip stages (described in section 1.4.1) were derived from the simulations with the hysteresis shown in Figures 1.33a to 1.33b for HNBR and for TPU, respectively.

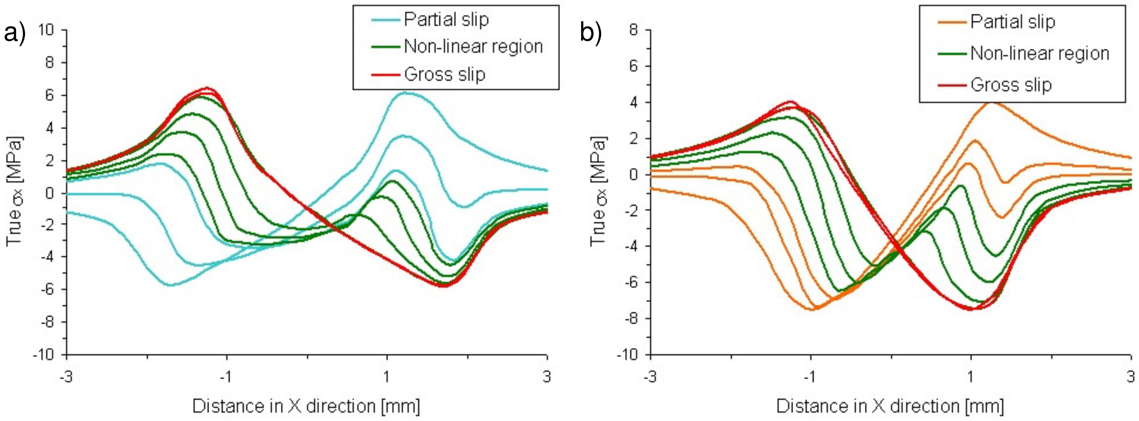

Fig. 1.38: $\sigma_{x\ true}$ of the contact area along to the specimen surface in the movement direction for HNBR (a) and TPU (b) material model.

Values of σ_x of both materials are shown along the investigated line in Figure 1.38, where the distribution has no change during the gross slip region. At the contact borders the stress has the same magnitude for compression and for stretching depending on the direction of specimen movement. The effect of the deeper dent and the higher friction coefficient is visible on the higher maximum value of the HNBR simulation. The τ_{xy} shear stress has a quite different distribution as Figure 1.39 shows. The shear stresses in the contact region oscillate locally (between their maximum and minimum values). The peak values are nearly the same for both materials. While the TPU model has well defined maximum and minimum points, HNBR has nearly equal stress on 50% of the contacting surface.

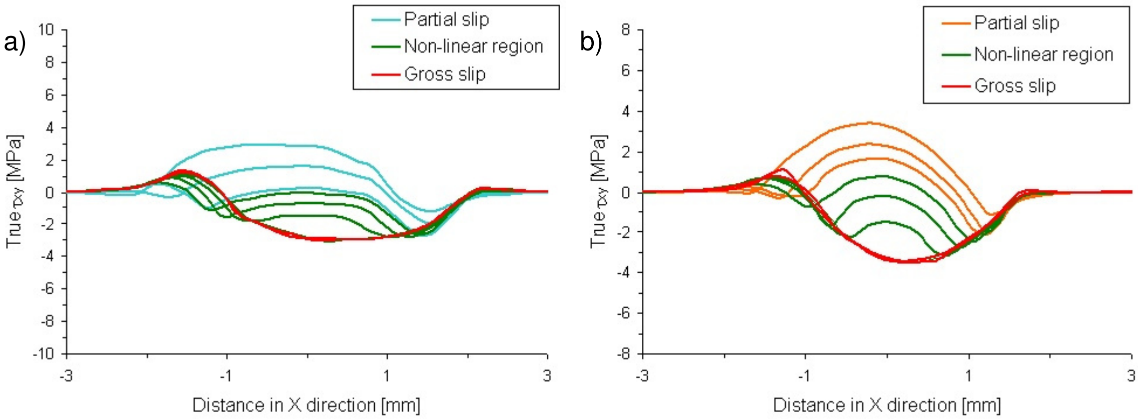

Fig. 1.39: $\tau_{xy\ true}$ of the contact area along to the specimen surface in the movement direction for HNBR (a) and TPU (b) material model.

Selected points at the interface are shown in Figure 1.40a for HNBR and in Figure 1.41a for the TPU model. Both figures contain diagrams (b), which show the paths of defined points under different displacement amplitudes. The sticking and sliding states are represented by points and curves, and the length of the sliding distance was defined for further analysis purposes (Figure 1.40b and 1.41b).

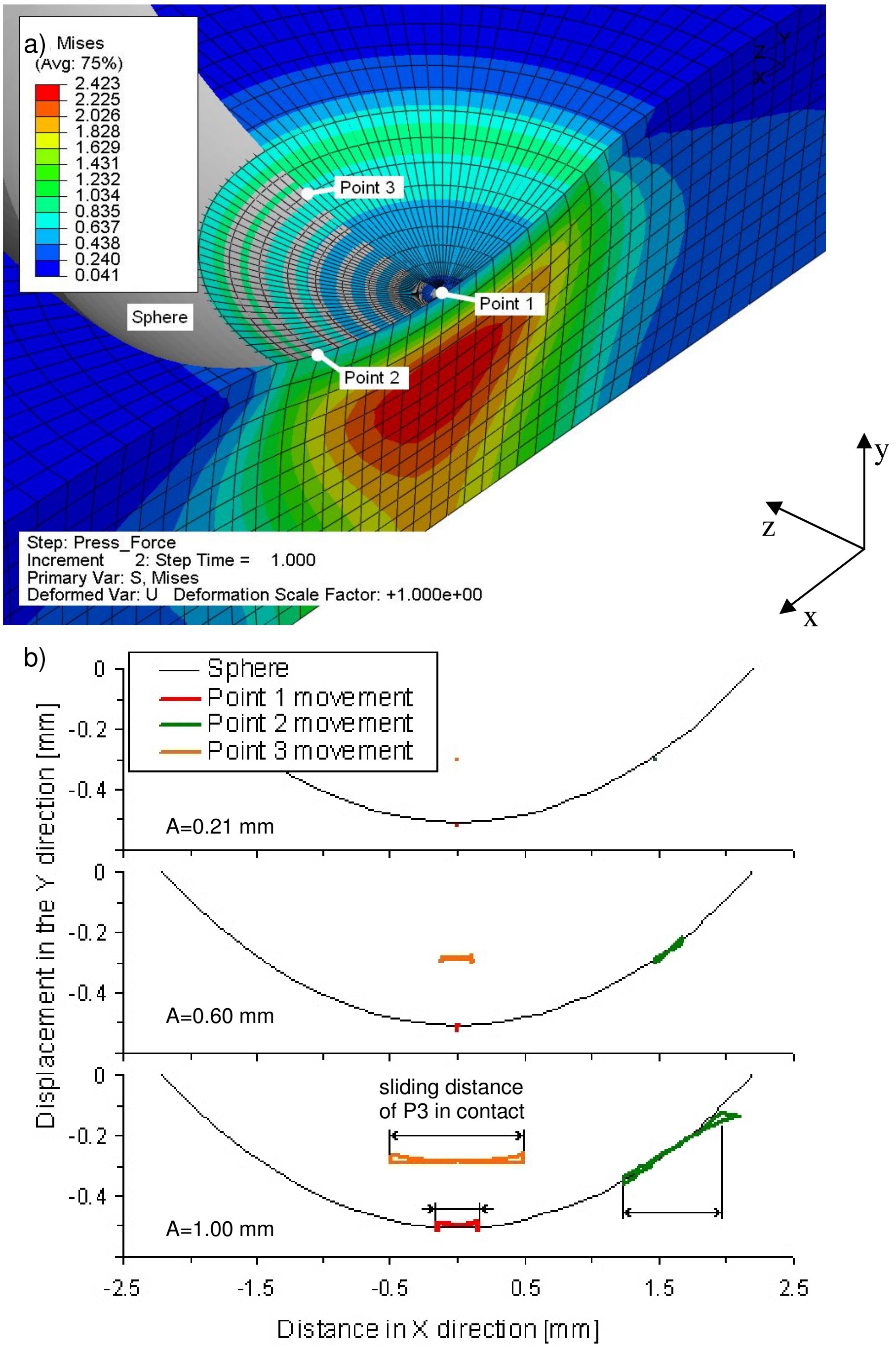

Fig. 1.40: Position of the selected points on the HNBR specimen surface after normal loading (a), and their movements in the X-Y direction as a function of the displacement amplitude (b). (Point 1 and 2 is in the plane of sphere contour, Point 3 is out of plane.)

These three points describe areas where the relevant stress states are different, and the material response varies significantly, depending on the distribution and size of the nominal and shear stresses and on the type of contact.

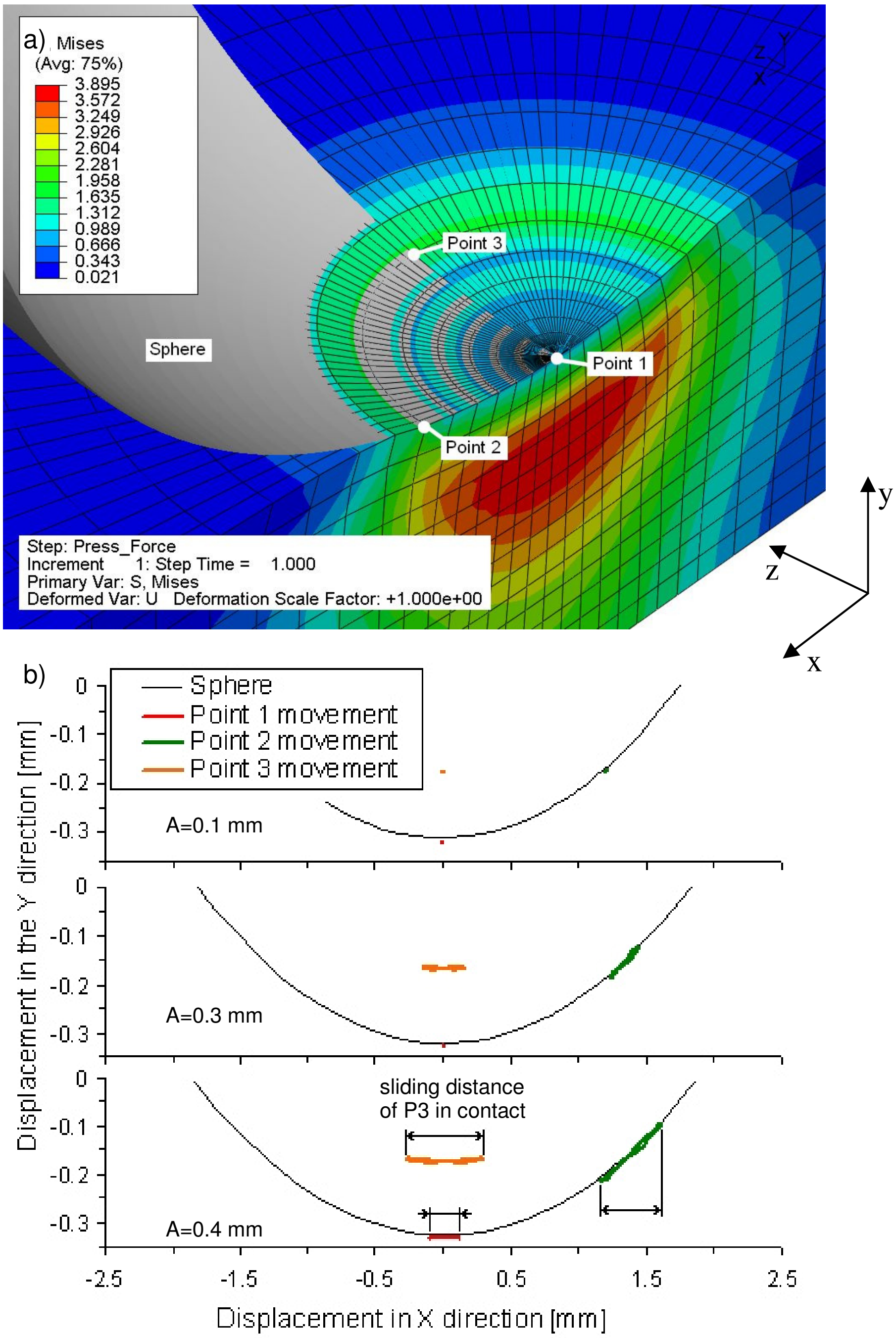

Fig. 1.41: Position of the selected points on the TPU specimen surface after normal loading (a), and their movements in the X-Y direction as a function of the displacement amplitude (b). (Point 1 and 2 is in the plane of sphere contour, Point 3 is out of plane.)

The main stress in the middle area (Point 1) is the shear generated by friction under the ball, which has a saw-tooth form with the properties of R=-1 and τ_{xymean}=0 (Fig. 1.42). The magnitude of the shear stress is related to the displacement amplitude up to the limit of gross slip.

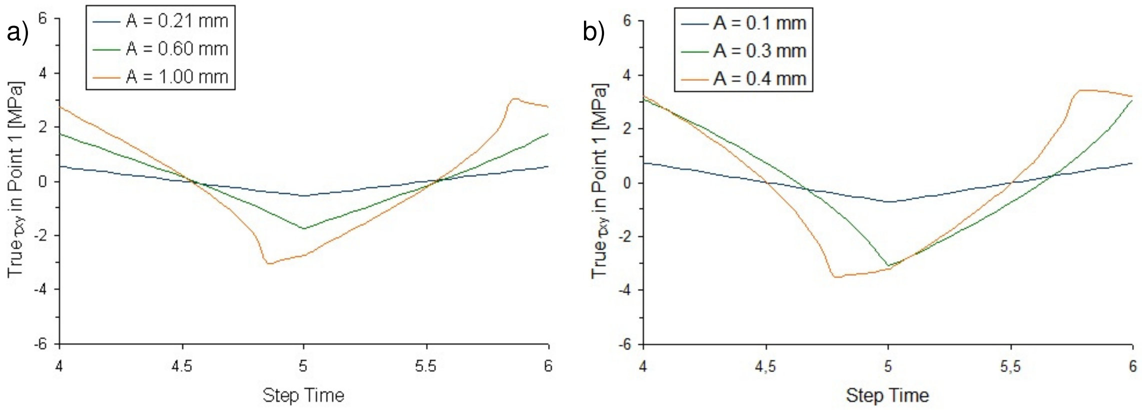

Fig. 1.42: Change of τ_{xy} in Point 1 during one cycle for HNBR (a) and TPU (b).

In Point 2 - which is located mostly in the sliding domain -, the nominal stress in the movement direction dominates together with shear forces, when contact is exist (Figure 1.43 and 1.44). HNBR has slightly higher tensile strain, the TPU simulation has slightly more one directional compression and shear stresses in this area.

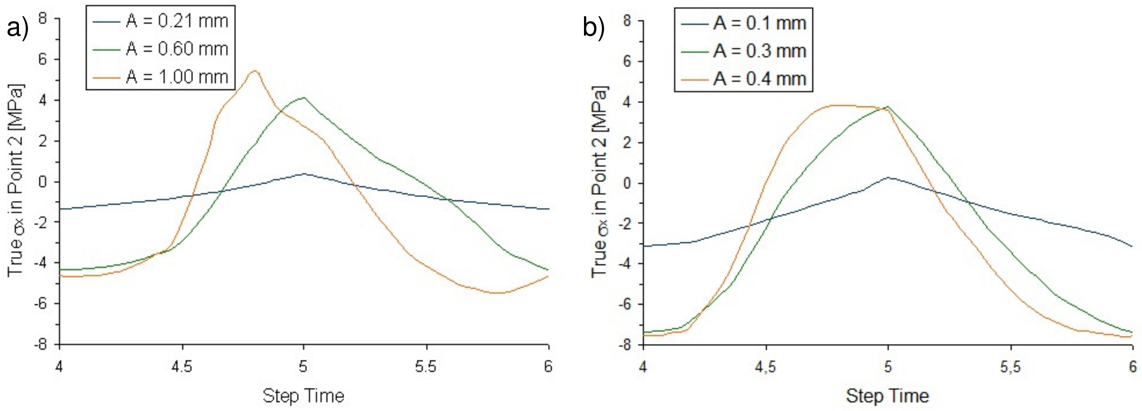

Fig. 1.43: Change of σ_x in Point 2 during one cycle for HNBR (a) and TPU (b).

The peak values occur before local gross slip behaviour, which depends on the dent depth and also on the contact borders, so cannot be determined directly from the measured displacement-force diagrams.

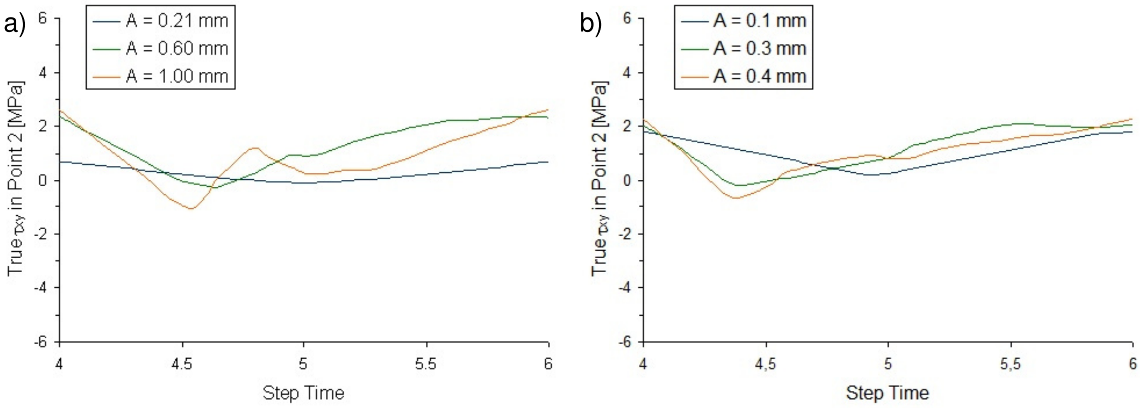

Fig. 1.44: Change of τ_{xy} in Point 2 during one cycle for HNBR (a) and TPU (b).

Point 3 is positioned at the same distance from Point 1 as Point 2, but perpendicular to the specimen movement. The σ_x (Figure 1.45), τ_{xy} and τ_{xy} values exhibit also periodicity change with momentary maximum value.

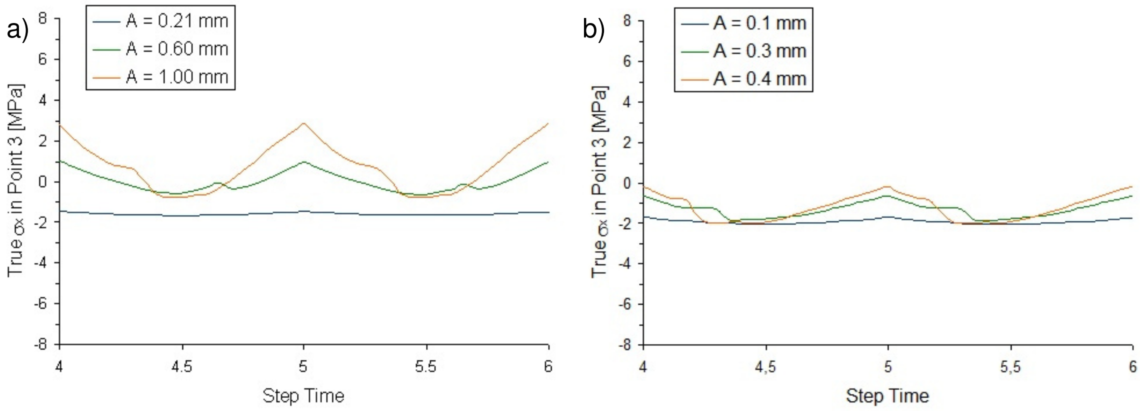

Fig. 1.45: Change of σ_x in Point 3 during one cycle for HNBR (a) and TPU (b).

All investigated stress components reveal lower peaks than in Point 1 and in Point 2, but more directional relevant cyclic shear stresses exist (Fig. 1.46 and 1.47).

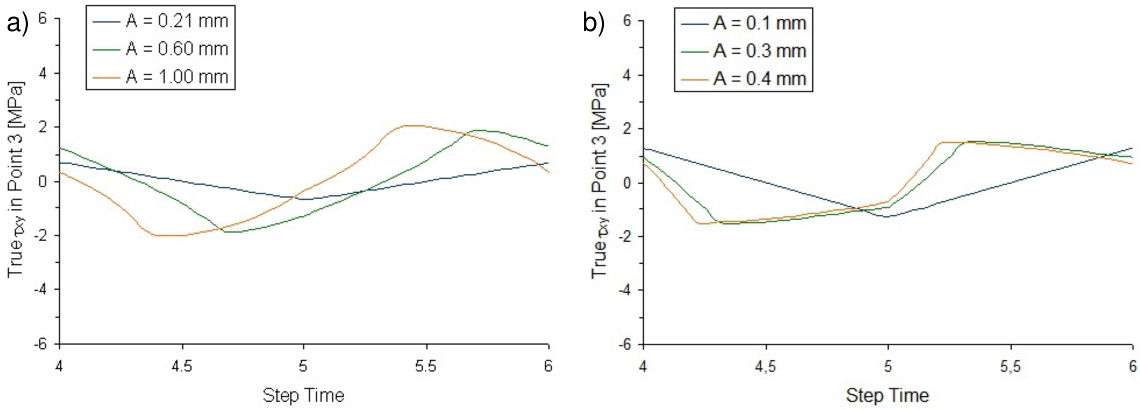

Fig. 1.46: Change of τ_{xy} in Point 3 during one cycle for HNBR (a) and TPU (b).

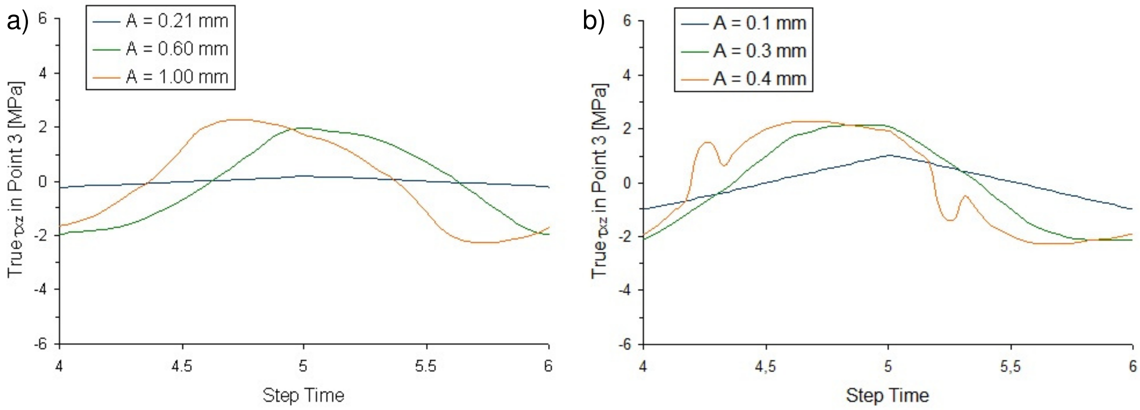

Fig. 1.47: Change of τ_{xz} in Point 3 during one cycle for HNBR (a) and TPU (b).

The maximum values of the diagrams above were determined and used to construct the simulated shear stress maximum vs. contact sliding distance in contact relationships for the 3 locations defined previously.

In addition to the determination of the relevant stress components, strain components were also determined the vicinity of the same points. These curves are shown in Figures 1.48 to 1.51 for comparison.

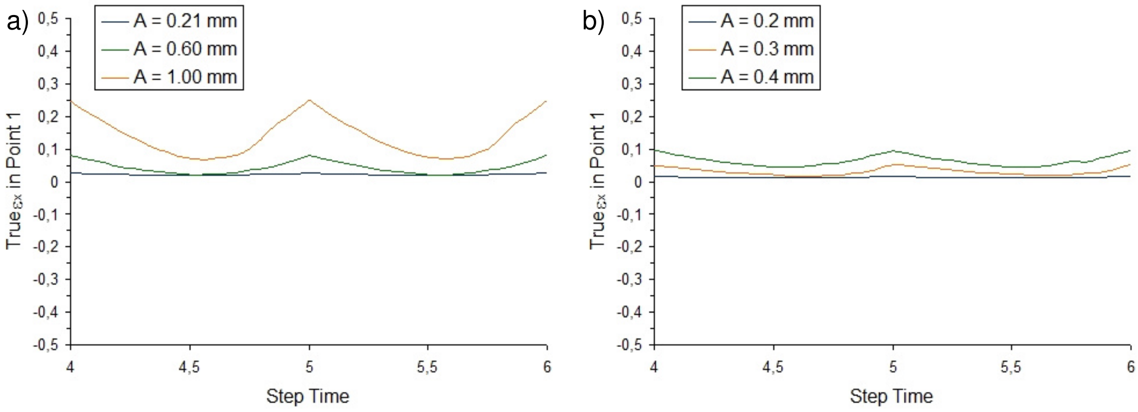

Fig. 1.48: Change of ε_x in Point 1 during one cycle for HNBR (a) and TPU (b).

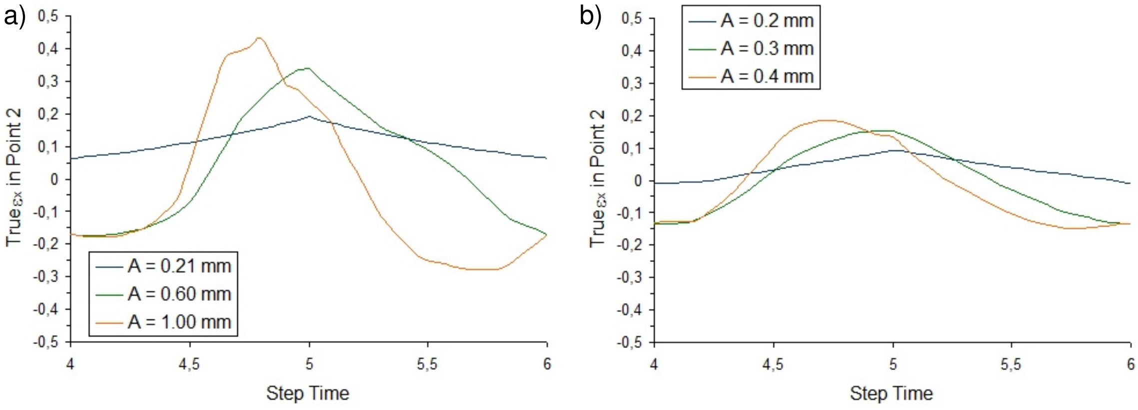

Fig. 1.49: Change of ε_x in Point 2 during one cycle for HNBR (a) and TPU (b).

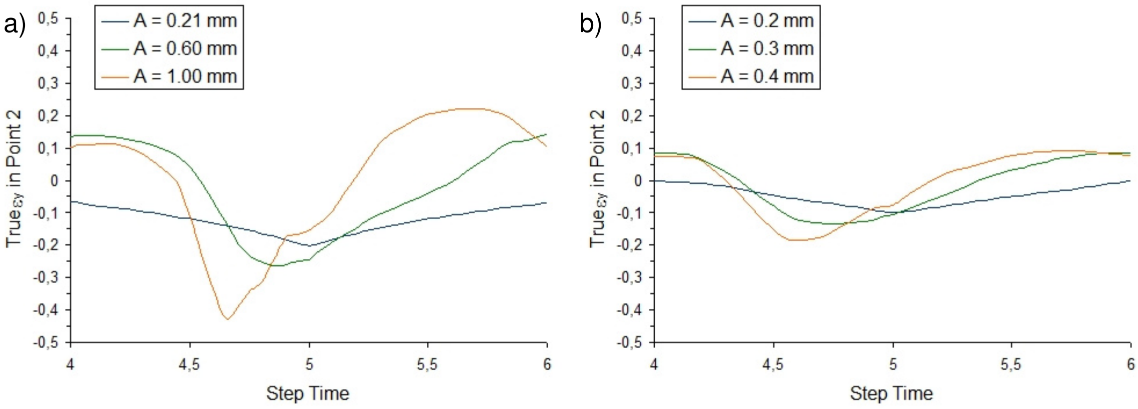

Fig. 1.50: Change of ε_y in Point 2 during one cycle for HNBR (a) and TPU (b).

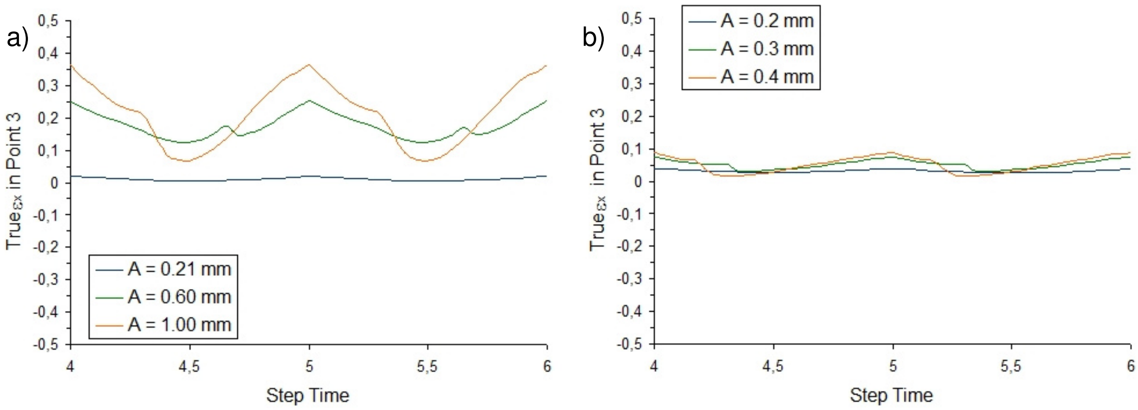

Fig. 1.51: Change of ε_x in Point 3 during one cycle for HNBR (a) and TPU (b).

It is concluded based on these simulation results that both the spatial and the temporal distribution of the stress and strain state of this simple ball-on-plate contact is very complicated for elastomeric materials revealing highly non-linear deformation behaviour.

1.4.3 Failure behaviour of the fretting fatigue test

In the second part of this chapter, the long-term fretting failure behaviour of the two elastomers was investigated. These tests were carried out at room temperature (23℃), under 30 N normal load with 3 Hz frequency with different force amplitudes up to about 500000 cycles (corresponding to appr. 2 days test duration).

Light microscope images of the worn HNBR surfaces are shown in Figure 1.52. With the smallest amplitude in the partial slip region (see Fig. 1.52a) no visible degradation was observed, only slight indentation was created at the contact zone by the material creep (compression set of the rubber under multiaxial test conditions). With the amplitude of 0.2 mm low abrasive wear paths are visible on the sides of the circles in the direction of movement (Figure 1.52b). Although, the gross slip limit was determined at tangential displacement amplitude of 0.85 mm, material loss in the middle region of the contact areas was recognized already at displacement amplitudes higher than 0.5mm (see Figure 1.52c, d and e). The material particles are moved from the contact zone and the debris is visible on the border of the worn contact area.

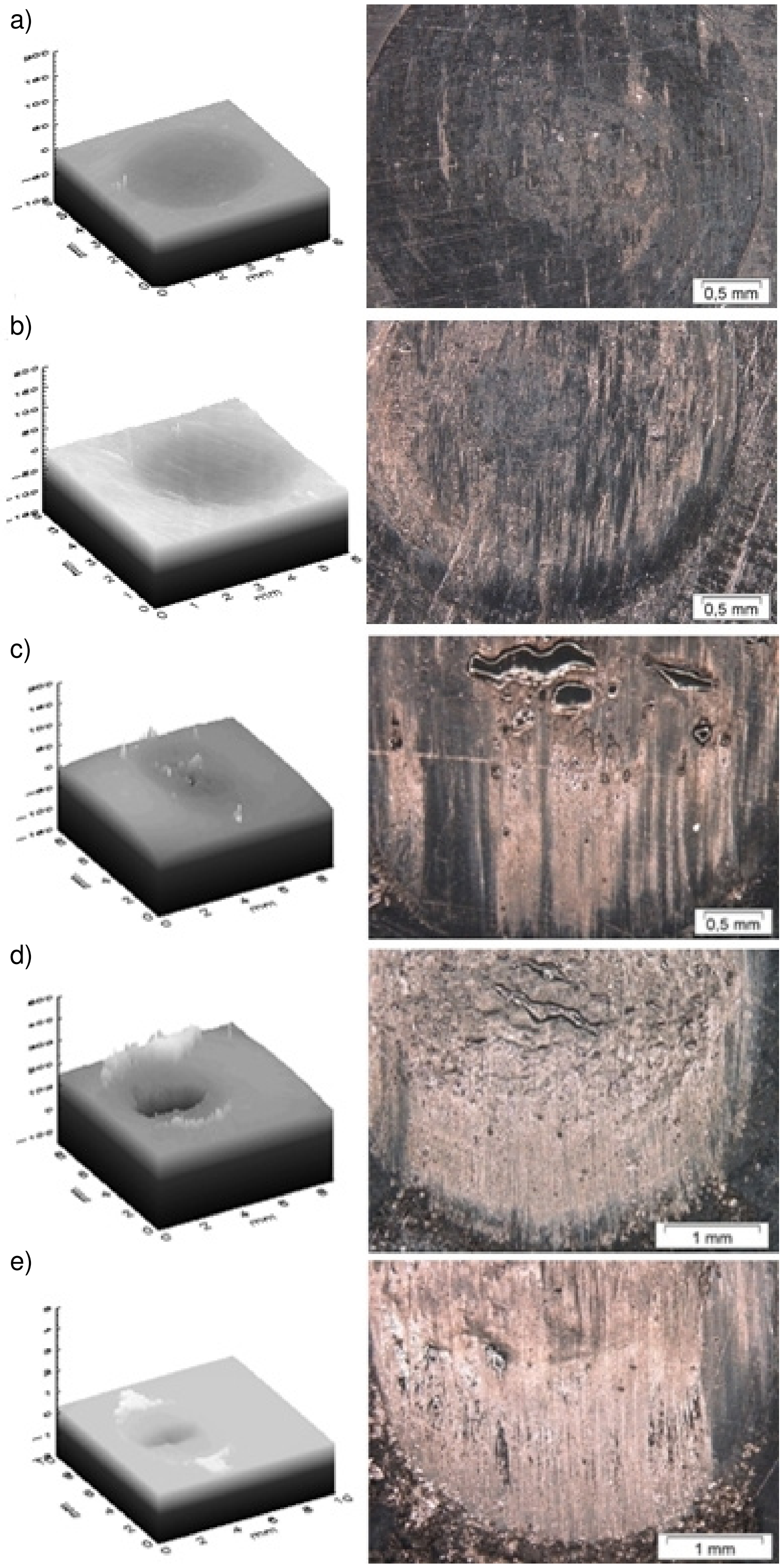

Fig. 1.52: Confocal microscope images (left) and light microscope images (right) of the worn HNBR surfaces with 30 N normal load at displacement amplitudes of 0.1 mm (a), 0.2 mm (b), 0.5 mm (c), 0.75 mm (d), and 1 mm (e).

Furthermore, the surface change by local indentation has been measured by a confocal microscope (MicroProf Vision, Fries Research & Technology GmbH, Bergisch Gladbach, D) and surface topography images are shown for various tangential displacement values in Figure 1.52 for HNBR surfaces (Berger, 2006). Profiles were taken in the middle of the contact field into the direction of the tangential displacement. These profiles are visible in Figure 1.53a along with the depths of the indentations as a function of the amplitude used.

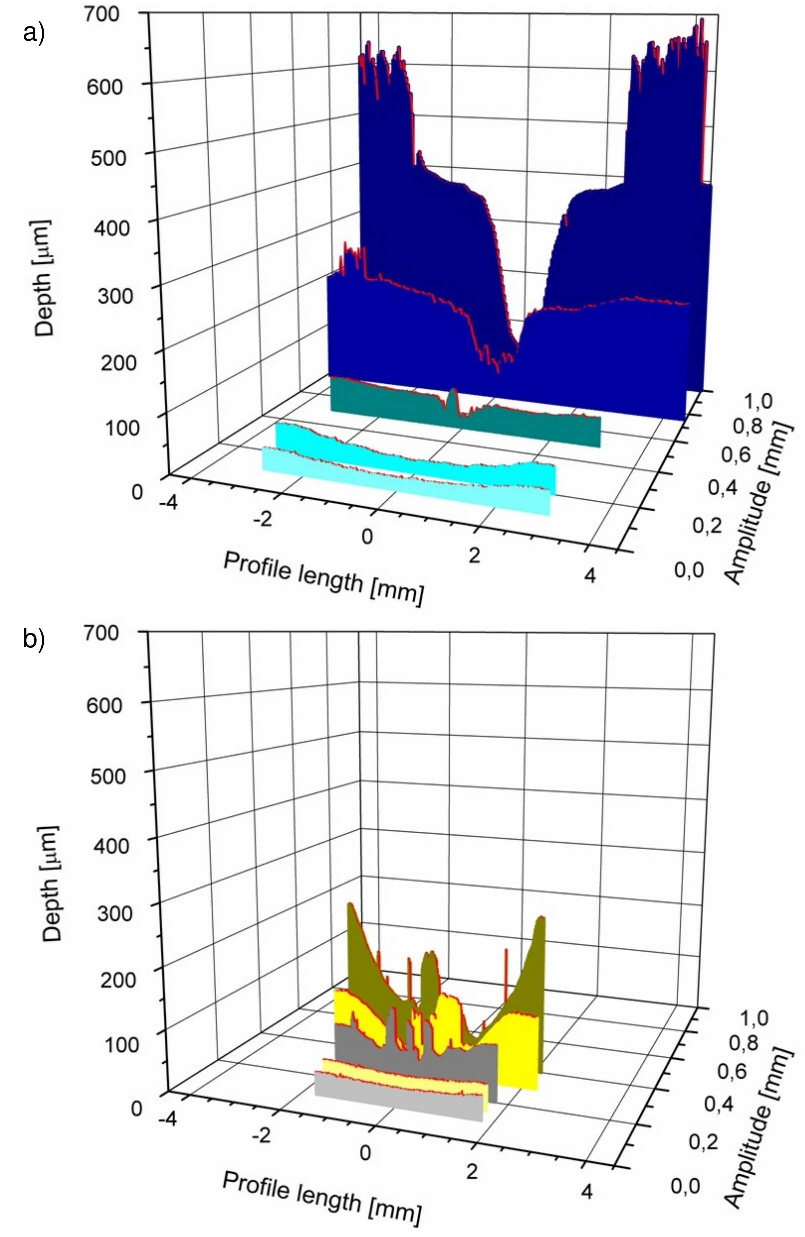

Fig. 1.53: Indentation depth and length of the HNBR (a) and TPU (b) material in function of the amplitude under 30 N normal load.

The profiles of the two lowest amplitudes do not show any degradation. The abrasion areas in the contact centres have the double width of the test amplitudes. The contact borders are well visible between the debris on both sides (see Figure 1.53a with the displacement amplitude of 0.8 and 1 mm).

Scanning electron microscope images (SEM, DSM 962, Carl Zeiss AG, Germany) of the HNBR surface for the 0.2 mm amplitude measurement shows a ring-like wear path formation in the partial slip area (Figure 1.54a). Moreover, small cracks were observed in the normal direction of the specimen movement as it is seen in Figure 1.54b. In the same direction less frequent small crack initiation is visible in the middle range of the contact surface; examples of these micro-cracks are shown in Figure 1.54c. In this range the material sticking is dominant.

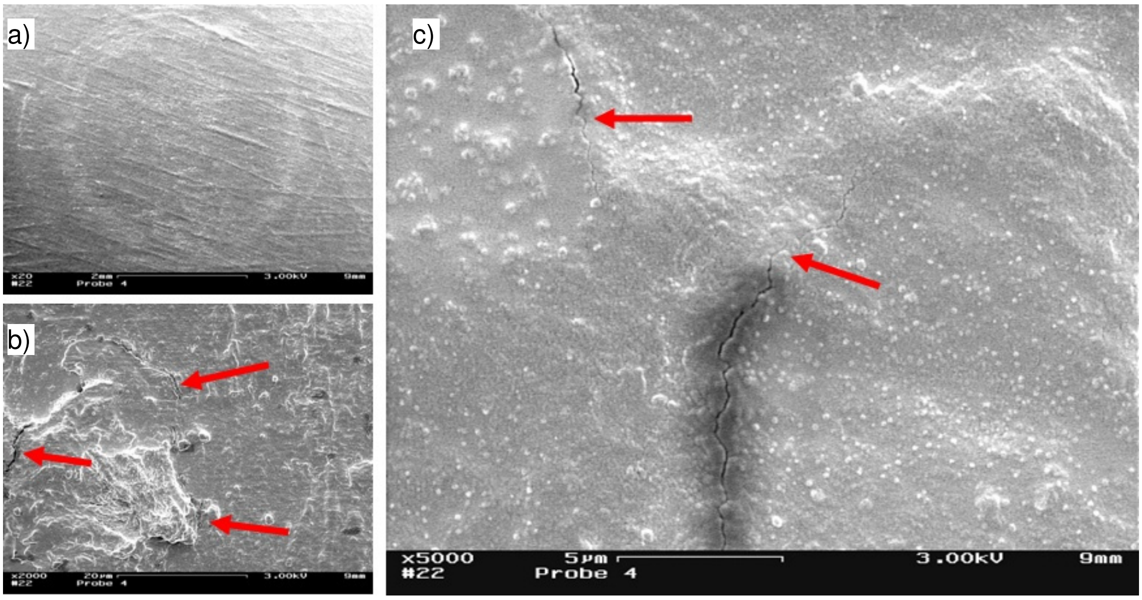

Fig. 1.54: Electron microscope images from the HNBR surface tested with 0.2 mm amplitude: 20x (a), 200x from the sliding (b) and 5000x magnification from the middle area (c). Arrows denote micro-cracks.

After crack propagation, the small particles removed leave the specimen surface producing pits (see Figure 1.55a) in the middle of the contact zone like the crater-like formation observed also by Karger-Kocsis (Karger-Kocsis, 2010).

In sliding region the abrasive wear dominates (see Figure 1.55b), where blisters and other imperfections in the material assist to the further crack formations (see Figure 1.55c).

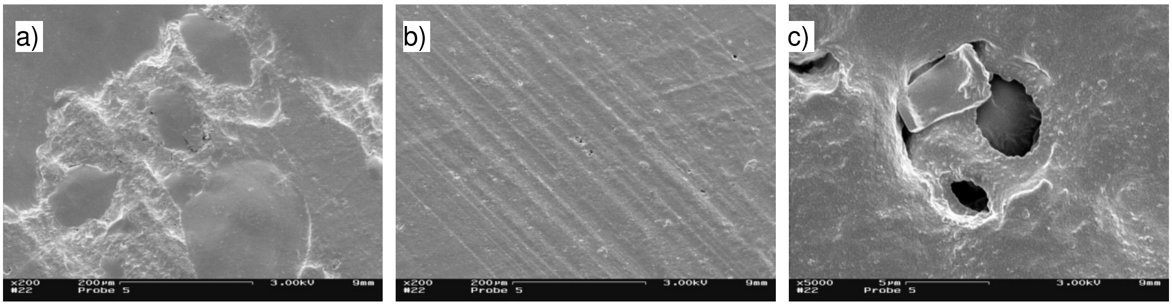

Fig. 1.55: Electron microscope images from the HNBR surface tested with 0.5 mm amplitude: 200x magnification from the central region (a), 200x (b) and 5000x magnification from sliding region (c).

The confocal microscopy and light microscopy images of worn surfaces of the TPU specimens are shown in Figure 1.56. In the partial slip region, the material loss has a ring form, where the width of these rings depends on the test amplitudes (Fig 1.56a and b).

The same effect is observable in the non-linear region of the RCFM. However, the removed material cannot leave the contact area and produces wavy forms in the center of the contact (Fig 1.56c and d). Thus three different wear behaviours were observed:

- partial slip dominates in a ring formed wear zone around the steel ball in the specimen,
- in the transition states the worn material aggregates in the middle of the contact zone and causes there some billows (Figure 1.56c and d),
- with gross slip the removed material parts are moved out from this contact area and huge wear was determined (Figure 1.56e).

The measured depth and length of the worn areas as a function of the displacement amplitude are plotted in Figure 1.53b with the same scale as for the HNBR material for comparison, and the amount of removed material under different displacement amplitudes is well visible.

The behaviour of TPU also can be described with the SEM images. Due to the combination of the high adhesion and friction forces, which results in high shear stresses, waviness is formed on the material surfaces, like the Schallamach waves (Schallamach, 1971; Xu, 2010) in micrometer scale as it is shown in Figure 1.57.

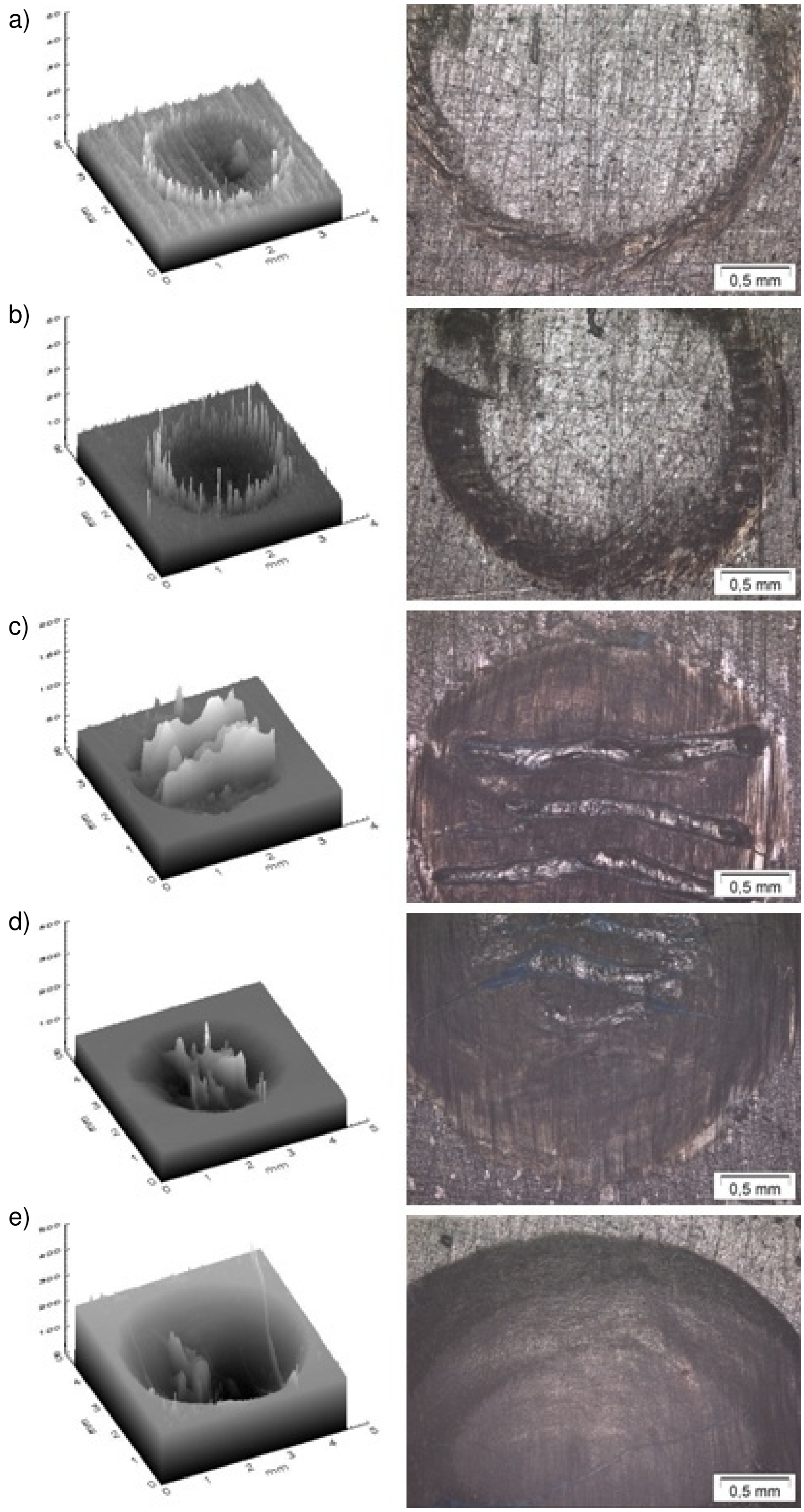

Fig. 1.56: Confocal microscope images (left) and light microscope images (right) of the worn TPU surfaces with 30 N normal load at displacement amplitudes of 0,05 mm (a), 0,1 mm (b), 0,2 mm (c), 0,3 mm (d), and 0,4 mm (e).

During the continuous sliding motion the peaks of these waves are torn, but due to the small sliding amplitudes the debris particles cannot move out from the contact area and get noodle forms (Martínez, 2010). Small debris particles are moving into the middle of the contact area and are building a new material layer there (Figure 1.58). A similar effect is visible in the partial slip region in Figure 1.59.

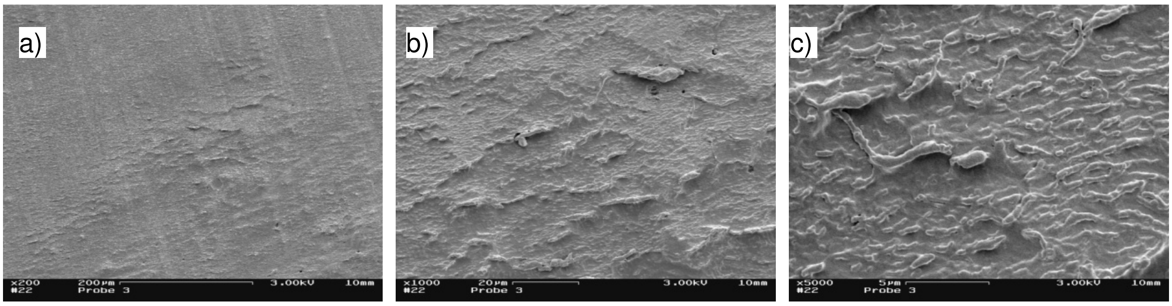

Fig. 1.57: Electron microscope images with the magnification of 200 (a), 1000 (b) and 5000 (c) from the TPU surface in the slip area of the measurement with 0,3mm displacement amplitude.

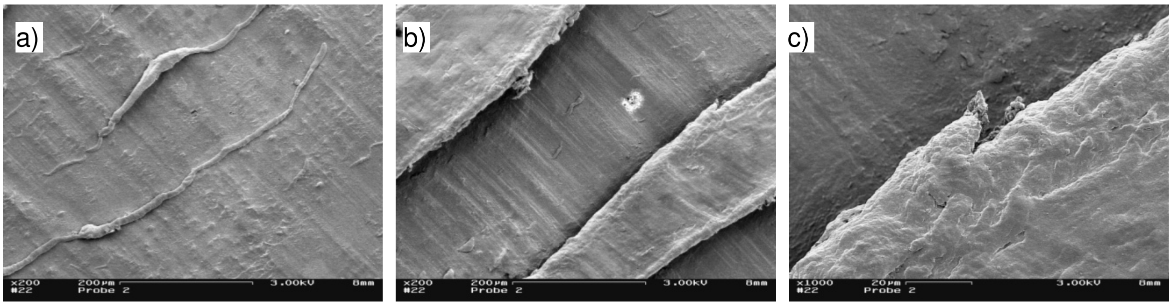

Fig. 1.58: Electron microscope images with the magnification of 200 (a and b), 1000 (c) from the TPU surface in the slip area (a) and in the middle zone (b and c) of the measurement with 0,3mm displacement amplitude.

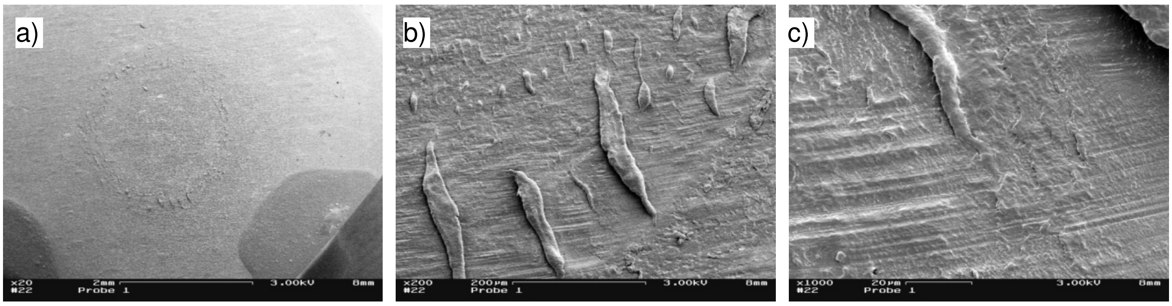

Fig. 1.59: Electron microscope images with the magnification of 20 (a) 200 (b) and 1000 (c) from the TPU surface of the measurement with 0,1mm displacement amplitude.

1.5 Summary and conclusions of the fretting fatigue results

To characterize the material response under fretting contact, a novel test system was developed based on a magnet shaker. Although the accurate setting of this set-up is extremely difficult, the set-up worked successfully during the measurements of this study.

To predict the region of interests of the various presumable fretting behaviours in the displacement - normal load diagrams, HNBR and TPU grade elastomers were investigated and Running Condition Fretting Maps were determined for both study materials in short-term fretting experiments.

Furthermore, to get more details about the strain distributions in the materials and to describe their creep and compression behaviour, some additional measurements were performed on a tribometer.

Simultaneously, to describe the different stress areas and the sliding displacements of the plane-sphere contact, finite element simulations of the HNBR and TPU material were carried out with the Abaqus software.

Moreover, the long-term fretting fatigue failure behaviour of the two elastomers was characterized by applying one normal load over a wide tangential displacement range. The worn contact surfaces were analyzed with confocal, light and electron microscope images.

The results of the short and long-term experiments, the simulations and the failure analysis can be summarized with the help of the sliding regimes depicted in the RCFMs:

- In the partial slip region in the middle of the contact zone, TPU does not reveal any failure. The shear stress in the tangential direction was determined by the FE simulation in the range of appr. ±0.8 MPa. This area is surrounded by a ring shaped wear zone. Surface waviness was observed to form in this region and the contact interfaces were moving against each other, which resulted in large scale sliding. Furthermore, a highly complex multiaxial stress state (a combination of normal and shear stress values in two directions) was observed in the corresponding FE simulations. In contrast, the HNBR material does not show any significant wear in this regime. According to the FE simulation all peak values of the relevant stress components are below 0.6 MPa. The created dent was produced by creep. However, somewhat unexpected were observed by small micro-cracks in the middle of the contact zone as well as at the ring.

- In the nonlinear-partial slip domain the simulated stresses increased until they reached their maxima at the limit of gross slip. The torn TPU materials were removed from the sides, the particles were deposited in the middle of the contact zone and warping was formed during the tangential oscillations. Depending on the size of the sliding interface, abrasive wear was observed for the HNBR specimens. In the stuck middle zone crack formations were observed at the smallest amplitude. The formation of the micro-crack was followed by the occurrence of micro-craters and the debris particles moved out of the contact area. The intensity of this process depends on the tangential amplitude, which produces deep macroscopic craters in the middle of the contact zone.
- This material behaviour becomes more pronounced for the HNBR material in the gross slip region. The TPU material response is different in the gross slip regime. The debris particles are able to leave the contact area, and the shear induced adhesive wear results in a smooth indentation dent.

The reliable construction of the Material Response Fretting Map under different loading conditions is a challenging task. Figure 1.60 shows two examples of wear behavior of the HNBR materials observed in other experiments. While typical wear may be observed in Figure 1.60a, a combination of wear and fretting fatigue is shown in Figure 1.60b. These examples clearly demonstrate that in addition to the test and boundary conditions investigated and to the failure types observed, a high number of additional conditions might exist and other failure types with different kinetics may be observed in these experiments.

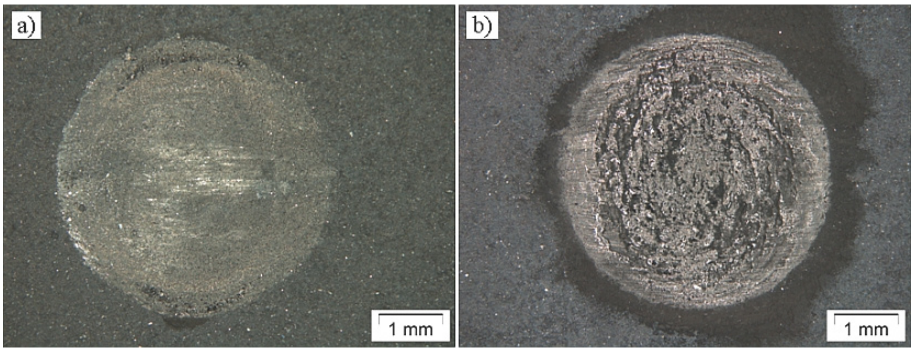

Fig. 1.60: Abrasive (a) and fretting wear (b) on the HNBR material surface.

Fretting behaviour models of the TPU and HNBR materials

The determination of the investigated elastomer behaviours under sphere-plane fretting conditions started with the description of the sliding regimes in section 1.4.1. Three different regimes were defined, where various material responses were expected. Under a chosen (30 N) normal load, one displacement amplitude of the sliding regime was analysed by a finite element simulation with the developed hyperelastic material models (section 1.3.2). The simulations have the following terms:

- the materials are incompressible,
- the material is in a stress free state at the $\varepsilon=0$ point,
- the model is valid for room temperature,
- the model does not contain a viscoelastic effect (time/frequency independent),
- the model does not show hysteresis or a Mullins effect, and
- the contact is defined by a constant friction coefficient without time dependency or adhesion.

In the contact areas three well defined locations were selected and their relevant stresses for one cycle were plotted (Point 1, 2 and 3). At the same normal load fretting fatigue measurements were performed for both materials with five different displacement amplitudes.

The specimen surfaces were analyzed by light, confocal and electron microscope images and the materials showed varying fretting response:

- Under gross slip conditions both materials show dominant abrasive wear which is the effect of the behaviour under high displacement amplitudes described below.
- The TPU material shows wave formation wear in the partial slip domain due to the shear stresses, and the removed particles remain in ring formation around the intact sticking area, or with higher amplitudes move to the contact centre and build warping there.
- With small oscillations the HNBR material shows no degradation. With higher amplitudes, cracks, which produce craters, are observable. The debris is moving to the contact side where, due to the sliding, abrasive wear is also noticeable.

These conclusions are summarized quantitatively in Table 1.4, where the “Simulated\Slide” column shows the X directional sliding length in contact of Point 1, 2 and 3 for a cycle.

The measured displacement amplitudes were compared with those of the simulations, where the tangential forces have the same maximum (and minimum) limits. Only in one case, amplitude differences could be detected - the HNBR fretting test with 0.5mm amplitude showed 0.6 mm in simulated results. The observed material response of the elastomer specimens at the specified locations is connected with the relevant simulated stresses.

Sliding distance in contact vs. simulated maximum shear stress values of Table 1.4 are plotted for both materials in Figures 1.61 and 1.62. The sliding distances of the sphere contact were correlated with the maximum shear stresses for both materials. The different symbols represent the different failure types observed in these specific loading situations. The material has to have a shear upper limit, where no failure can be observed independently of the sliding length (for example with the use of air bushing). Then, due to the enlargement of the shear stress cracks are produced on the surfaces, which together with the slide may cause crater formations. With higher displacement the stiffness of counterpart is decisive, producing abrasive wear. Under the minimum shear limit no degradation can be observed. While under sticking contact the shear stress is proportional to the specimen displacement (tangential forces), under sliding it depends on the magnitude of the adhesive forces (correlated to the COF, normal pressure, temperature or lubrication etc.).

Material	**Tests**		**Simulated**							
	Ampl. [mm]	**Wear type observed (P1-P2-P3)**	**Ampl.** [mm]	**Slide** [mm]	**P 1**	**Point 2**		**Point 3**		
					τ_{xy} [MPa]	σ_x [MPa]	τ_{xy} [MPa]	σ_x [MPa]	τ_{xy} [MPa]	τ_{xz} [MPa]
HNBR	0.2	micro cracks	0.21	0	± 0.6					
		abrasive / micro cracks		0		+ 0.5 - 1.2	+ 0.7 - 0			
		abrasive / micro cracks		0				- 1.3 - 1.4	+ 0.7 - 0.6	± 0.2
	0.5	craters	0.6	0	± 1.8					
		abrasive		0.3		± 4.1	+ 2.4 - 0.2			
		abrasive		0.4				+ 1.1 - 0.5	± 1.9	± 2
	1	abrasive / craters	1	0.25	± 3					
		abrasive		0.75		+ 5.5 - 4.6	+ 2.6 - 1.2			
		abrasive		1.1				+ 2.9 - 0.7	± 2	± 2.2
TPU	0.1	no degradation	0.1	0	± 0.8					
		waviness		0.05		+ 0.1 - 3.1	+ 1.8 - 0			
		waviness		0.05				- 1.7 - 1.8	± 1.5	± 1
	0.3	waviness	0.3	0	± 3					
		abrasive / adhesive		0.25		+ 4 - 7.3	+ 2 - 0.2			
		waviness		0.3				- 0.6 - 1.7	± 1.7	± 2.1
	0.4	abrasive / adhesive	0.4	0.25	± 3.5					
		abrasive / adhesive		0.5		+ 4 - 7.5	+ 2.2 - 0.7			
		abrasive / adhesive		0.6				+ 0 - 1.8	± 1.8	± 2.1

Table 1.4: Summary of determined material responses and simulated relevant stresses under fretting condition.

A similar material response map is shown for the TPU material in Figure 1.62. The waviness formation was observed between the abrasive wear and the failure free area, where the size and the amount of the debris are related to the quantity of the sliding in contact.

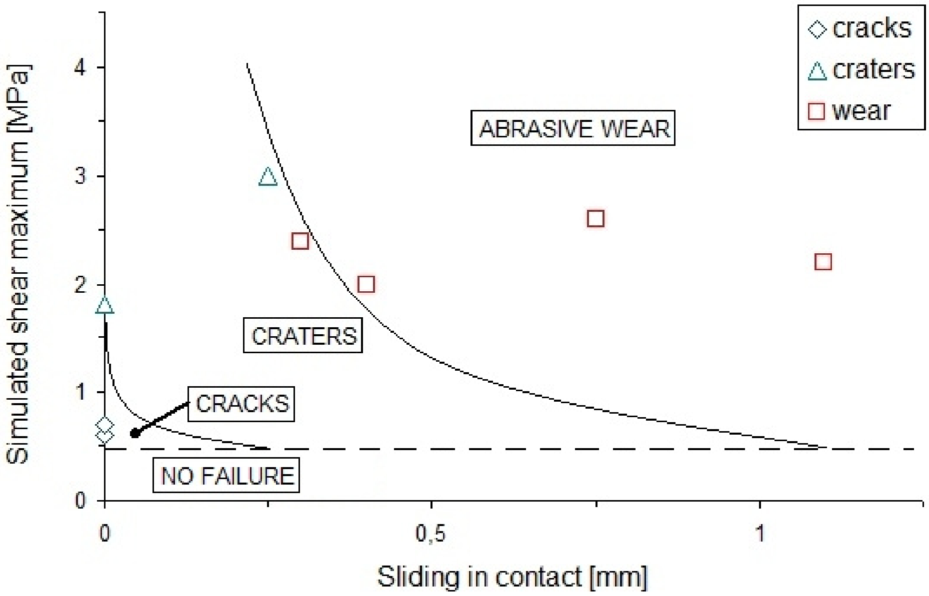

Fig. 1.61: Contact failure behaviour of HNBR at different simulated shear stress levels as a function of the sliding distance.

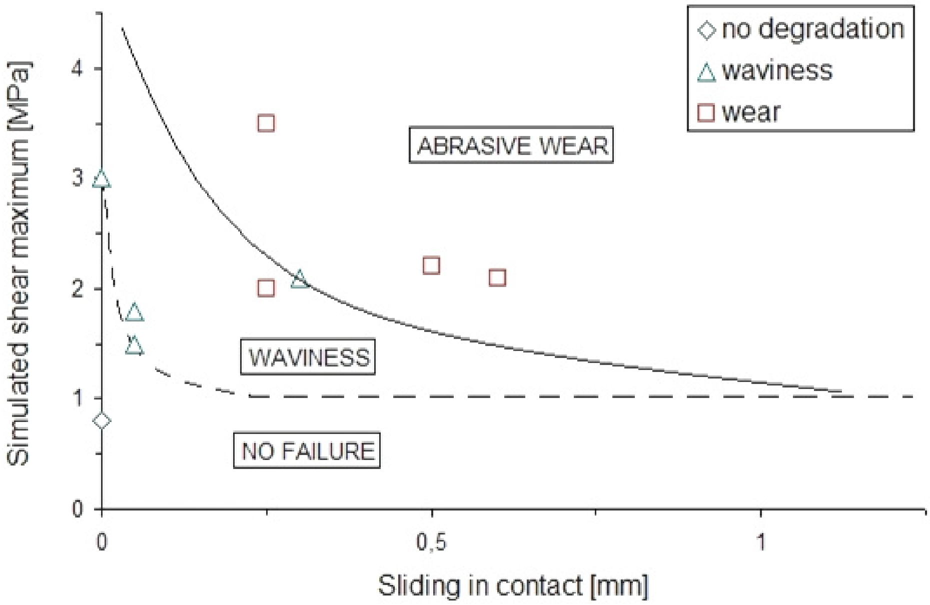

Fig. 1.62: Contact failure behaviour of TPU at different simulated shear stress levels as a function of the sliding distance.

These models are compared with the results of the bulk fatigue experiments and the conclusions drawn are described in section 3.6.

References

D.K. Baek, M.M. Khonsari (2006): „Fretting behavior of a rubber coating: Friction characteristics of rubber debris", Wear 261, pp. 1114-1120.

G.R. Berger (2006): „Untersuchungen zur Abformung geometrischer und stochastischer Strukturen an Spritzgießformteilen", PhD thesis, Institute of Plastics Processing, Montanuniversität Leoben, 2006, Chapter 2.2.

B.J. Briscoe, A. Chateauminois, T.C. Lindley, D. Parsonage (1998): „Fretting wear behaviour of polymethylmethacrylate under linear motions and torsional contact conditions", Tribology International 31, pp. 701-711.

Brüel & Kjær (1198): „Introduction to Shock & Vibration", Lecture note, BA 7674-12.

A. Chateauminois, B.J. Briscoe (2003): „Nano-rheological properties of polymeric third bodies generated within fretting contacts", Surface and Coatings Technology 163-164, pp. 435-443.

K. Dang Van (1993): „Macro-micro approach in high-cycle multiaxial fatigue" in D.L. McDowell, R. Ellis: Advances in Multiaxial Fatigue, ASTM, Philadelphia, pp. 120-130.

J.G. Drobny (2007): „Handbook of Thermoplastic Elastomers", Hardcover, Plastic Design library.

M.C. Duborg, A. Chateauminois, B. Villechaise (2003): „In situ analysis and modeling of crack initiation and propagation within model fretting contacts using polymer materials", Tribology International 36, pp. 109-119.

SKF-Economos Austria GmbH: „Material Data", 03/2003

T.N. Farris, G. Harish, C. Tieche, T. Sakagami, M.P. Szolwinski (2000): „Experimental tools for characterizing fretting contacts", Solid mechanics and material engineering Series A 43, pp. 374-383.

S. Fouvry, Ph. Kapsa, L. Vincent (1995): „Analysis of sliding behaviour for fretting loadings: determination of transition criteria", Wear 185, pp. 35-46

S. Fouvry, P. Kapsa, L. Vincent, K. Dang Van (1996): Theoretical analysis of fretting fatigue cracking under dry friction for fretting loading conditzions", Wear 195, pp. 21-34.

S. Fouvry, P. Kapsa, L. Vincent (1996): „Quantification of fretting damage", Wear 200, pp.186-205.

M. Godet (1984): „The third body approach: a mechanical view of wear", Wear 100, pp. 437-452.

Q. Guo, W. Luo (2002): „Mechanisms of fretting wear resistance in terms of material structures for unfillef engineering polymers", Wear 249, pp. 924-931.

G.M. Hamilton (1983): „Explicit equations for the stresses beneath a sliding spherical contact", Proceedings of the Institution of Mechanical Engineers 197C, pp. 53-59.

H.R. Hertz (1895): „Ueber die Beruehrung elastischer Koerper (On Contact Between Elastic Bodies)," Gesammelte Werke (Collected Works) 1, Leipzig (G)

D.W. Hoeppner (1992): „Mechanisms of fretting-fatigue and their impact on test methods development", ASTM-STP 1159, pp. 23-32.

P.L. Hurricks (1970): „The mechanism of fretting: a review", Wear 15, pp. 389-409.

I. Gódor, J. Schiffer, F. Grün, Z. Major, T. Schwarz (2009): „Einige Gesetzmäßigkeiten über das tribologische Verhalten von ungefüllten und gefüllten TPU-Materialien", GfT Tribologie-Fachtagung, 21-23 September 2009, Gottingen, Germany.

S. Jagels (2006): „Oilfield Engineering with Polymers 2006", London, UK, paper 15.

J. Karger-Kocsis, D. Felhös, D. Xuc (2010): „Mechanical and tribological properties of rubber blends composed of HNBR and in situ produced polyurethane", Wear 268, pp. 464–472.

R.N. King, T.C.Lindley (1981): „Fretting fatigue in a 3 ½ Ni-Cr-Mo-V rotor steel", D. Francios, Vol. 4, pp. 631-640.

A. Krichen, M. Kharrat, A. Chateauminois (1996): „Experimental and numerical investigation of the sliding behaviour in a fretting contact between poly (methylmethacrylate) and glass counterface", Tribology International 29, pp. 615-624.

A. Krichen, Ch. Bradai, A. Chateauminois, M. Kharrat (1999): „Surface damage pf poly(methylmethacrylate) under fretting loading", Wear 230, pp. 146-155.

J.F. Lamethe, P. Sergot, A. Chateaumoinois, B.J. Briscoe (2003): „Contact fatigue behaviour of glassy polymers with improves toughness under fretting wear conditions", Wear 255, pp. 758-765.

F.J. Martínez, M. Canales, J.M. Bielsa, M.A. Jiménez (2010): „Relationship between wear rate and mechanical fatigue in sliding TPU–metal contacts", Wear 268, pp. 388-398.

J.F. Matlik, T.N. Farris (2003): „High frequency, high temperature fretting fatigue investigations", 44th AIAA/ASME/ASCE/AHS Structures, Structural Dynamics, and Materials Conference, 7-10 April 2003, Norfolk Virginia.

R.D. Mindlin, H. Deresiewicz (1993): „Elastic spheres in contact under varying oblique forces", Archive of Applied Mechanics 63, pp. 402-412.

R.W. Ogden (1972): „ Large Deformation Isotropic Elasticity - On the Correlation of Theory and Experiment for Incompressible Rubberlike Solids", Proceedings of the Royal Society of London, Series A, Mathematical and Physical Sciences 326, No. 1567, pp. 565-584.

C. Petiot, L. vincent, K. Dang Van, N. Maouche, J. Foulquier, B. Journet (1995): „An analysis for fretting-fatige failure combined with numerical calculation to predict crack nucleation", Wear 181-183, pp. 101-111.

H. Proudhon, S. Fouvry, G.R. Yantio (2006): „Determination and prediction of the fretting crack initiation: introduction of the (P, Q, N) representation and definition of variable process volume", International Journal of Fatigue 28, pp. 707-713.

A. Schallamach (1971): „How does rubber slide?", Wear 17, pp. 301–312.

T.A. Stolarski, S.M. Hosseini, S. Tobe (1998): „Surface fatigue of polymers in rolling contact", Wear 214, pp. 271-278.

M.P. Szolwinski, Th.N. Farris (1996): „Mechanics of fretting fatigue crack formation", Wear 198, pp. 93-107.

M. Tur, J. Fuenmayor, J.J. Ródenas, E. Giner (2003): „3D analysis of the inluence of the specimen dimensions on fretting stresses", Finite Elements in Analysis and Design 39, pp. 933-949.

L. Vincent, Y. Berthier, M. Godet (1992): „Testing methods in fretting fatigue: a critical appraisal", ASTM STP 1159 on standardization of fretting fatigue test methods and equipment, West Conshocken, PA: American, Society for Testing and Materials, pp. 33–48.

B. Verheydea, M. Romboutsa, A. Vanhulsela, D. Havermansa, J. Menevea, M.Wangenheimb (2009): „Influence of surface treatment of elastomers on their frictional behaviour in sliding contact", Wear 266, pp. 468–475.

O. Vingsbo, M. Soderberg (1988): „On fretting maps", Wear 126, pp. 131-147

R.B. Waterhouse (1972): „Fretting Corrosion", Pergamon Press, Oxford, pp. 4-5.

R.B. Waterhouse (1981): „Fretting Fatigue", London: Applied Science.

B.U. Wittkowsky, P.R. Birch, J. Domínguez, S. Suresh. (1999): „An apparatus for quantitative fretting-fatigue testing", Fatigue and Fracture of Engineering Materials and Structures 26, pp. 469-78.

D. Xu, J. Karger-Kocsis (2010): „Rolling and sliding wear properties of hybrid systems composed of uncured/cured HNBR and partly polymerized cyclic butylene terephthalate (CBT)“, Tribology International 43, pp. 289-298.

Z.R. Zhou, L. Vincent (1995): „Mixed fretting regime", Wear 181-183, pp. 531-536.

2. ANALOG TRIGGERED IMAGE ACQUSITION SOFTWARE

2.1 Introduction and objectives

Due to the low stiffness, the nonlinear mechanical behaviour, the temperature dependence and the anisotropy, strain measurements of polymeric materials require special considerations and techniques compared to metals. The exact determination of the strain level of a stretched polymer bears several problems, like the high strain for strain gages or the distinct stress concentrations under the fixing points of strain transducers. Non-contact optical methods have several advantages (non-contacting measurements, image acquisition for post mortem analysis and for process automation, more strain directions etc.) and are frequently used for the strain measurement of polymeric materials (Brown, 1999; Jerabek, 2010). The disadvantages of this type of systems are the price, the difficult set-up and the camera resolution dependence. The images of the specimen surface are taken by camera and then the software measures the strain between two marks based on the contrast change. Increasing the number of marks it is possible to measure more displacements simultaneously, or painting small dots, speckle structures on the whole surface, it is possible to measure the total strain distribution on the surface of the material. Using two calibrated cameras, the strain can also be determined in the third dimension (GOM, 2004).

As one of the objectives of this thesis was to improve fatigue test methods for elastomeric materials by simultaneous damage characterization, a test set-up using a video extensometer and a novel image data acquisition procedure was developed and implemented, as described in this chapter. The fatigue test methods are then described in chapter 3. The optical strain measurement system must fulfil two main functions:

- to continuously measure the strain during cyclic loading between the gage marks under uniaxial conditions and
- to detect and follow the crack initiation and crack extension process.

Even though the exact detection of the contour of the specimen is not easy, the strain can be measured in longitudinal as well as in transverse direction, and both true stress and strain values might be calculated. Furthermore, in most cases the cameras used in these conventional video systems run with a precise time trigger, controlled by their own hardware and software tools and were successfully applied in many material testing applications under static and monotonic loading conditions (Casarotto, 2005; Sasso, 2008; Jerabek, 2010).

However, for fatigue experiments performed under cyclic loading and over a wide frequency range and over a long time period, the synchronization between the analogue output signals of the testing machine (force and/or displacement) and the image acquisition software became more difficult. The perfect synchronization between the output signals and the camera image is the prerequisite of the application of physically based data reduction methods (e.g., true stress and strain curves).

Hence, in addition to the existing optical measurement and software tools, cyclic tests require a specially designed software tool, which allows for a precise image acquisition for optical measurements. The particular objective of this research task was the development of a modular image data acquisition software tool which is suited for an automatic data recording and for a precisely timed image acquisition and recording over a couple of days during cyclic loading experiments.

2.1.1 About LabVIEW, software and hardware requirements

The software package developed for optical strain measurements have been written in LabVIEW 7.1 (National Instruments Corporation, Austin, TX, USA), which is built on the graphical (“G”) programming language. Basic features of the software are the special pre-defined modular structure, and an easy graphical editing. Under the Windows operating system the executable LabVIEW programs are called as “Virtual Instruments” (“VI”s), and theirs program codes are the block diagrams. See manual for more detailed information about the structure, features and programming of LabView (LabVIEW ™ User Manual, 2003). The following hardware and software have been applied in the optical extensometer:

- LabVIEW 7.1 (National Instruments, NI)
- Data acquisition module (NI DAQmx)
- Image handling modules (NI IMAQ Vision and IMAQ for IEEE 1394 2.0)
- Measurement & Automation Explorer (NI)
- Firewire CCD (Charge Coupled Device) camera (Dolphin F201B)
- Firewire PCI card
- A/D Converter (NI BNC-2110)
- IMAQ Data acquisition PCI card (capable for analogue triggering, NI PCI-6251M)

2.1.2 Calibration and camera setup

Different forms of optical distortions are shown in Figure 2.1. It is not possible to remove the different forms of optical distortions from the acquired pictures with one camera (Figure 2.1). The calibration should be done with an image file, where the distances for both directions are exactly defined between the pixels. To determine the distance of the pixels a lattice from circles could be used. The saved image is modified with an algorithm by the IMAQ Vision Builder software, which places the circle onto the lattice points, creating the calibration file for the further measurements (IMAQ Vision for LabVIEW User Manual, 2000).

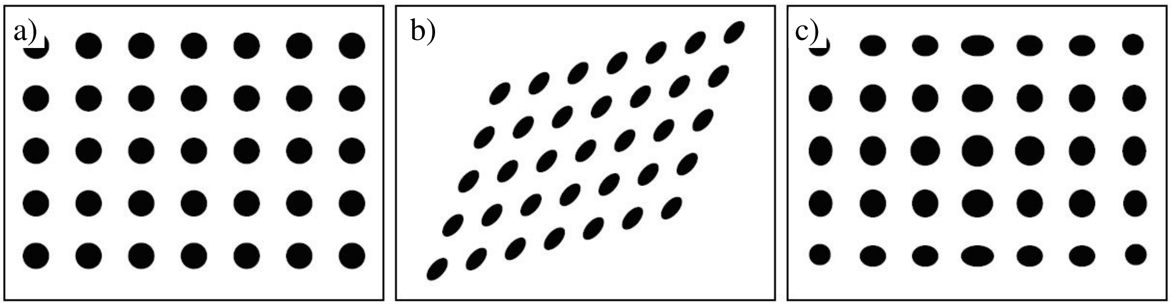

Fig. 2.1: Perfect image (a), perspective view (b), nonlinear distortions (c).

To set the camera properties, we can control the acquired pictures by the Measurement & Automation Explorer software. Taking the histogram diagram of the image, we have to set the lights of specimen surface, the brightness and shutter speed of the camera to hold the number of the totally white and black pixels minimum, otherwise we lose sensitivity in the edge detections.

2.1.3 Determination of the measured distances

The most important part of the optical measurement is the edge detection and the definition of the distances. Detection of the edges is in connection with the pixel brightness, where the intensity of absolute black is 255 and full white is 0. The characteristic of an average edge is shown in Figure 2.2a. To define the Gray Level Intensities we have to define a searching area (Region of Interest – ROI), where the pixel profiles are determined with the given “Scan Direction” and “Subsampling Ratio” - distance between two “Search Lines” in pixel (Figure 2.2b).

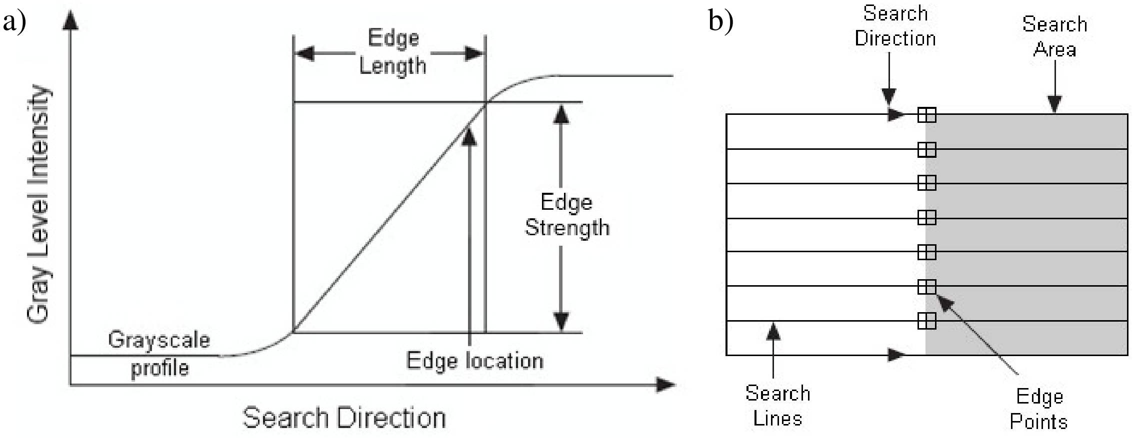

Fig. 2.2: Edge modelling (a) and settings of the gray level detection (b).

To calculate the contrast value in one location, the average intensity of more pixels has to taken starting from the half of the “Steepness” and with the length of the “Width” parameter as it is shown in Figure 2.3a. The edge will be determined in that point, where the intensity difference of the two “width” area is equal with the “Contrast” setting. To increase the sensitivity and precision of the process, all pixels are dissolved into 12 sub-pixels, where the intensity levels are Spline interpolated from the neighbour pixels. Figure 2.3b shows an example from the measurements, with the location of the edge-point found.

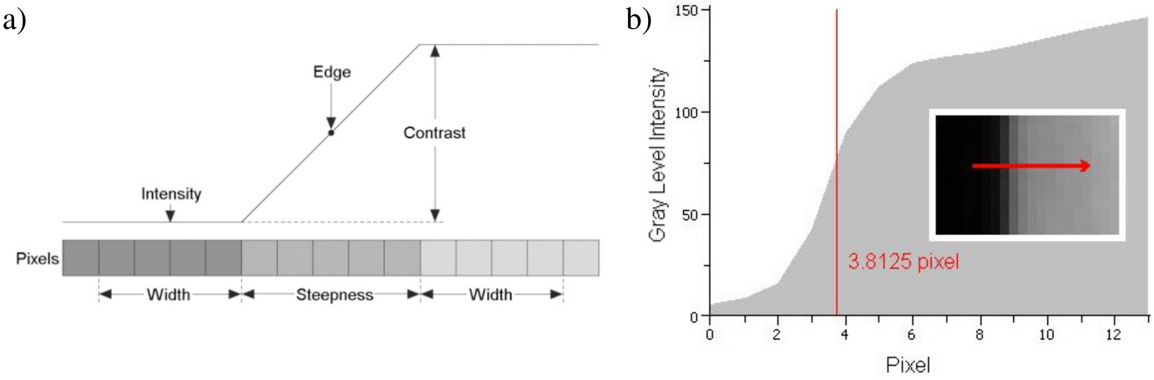

Fig. 2.3: The edge detection method (a) and a real example (b).

2.1.4 Preliminary stage of the video extensometer evaluation

The main stages of the optical measurement with CCD cameras are: the calibration, the image acquisition, the measurement and the evaluation of the data. In previous work by the author several modules have been created for different tests and are described in detail: creep, displacement (or force) and strain controlled measurements (Vezer, 2004). The calibration and the evaluation processes are the same for all types of material tests (except the strain controlled mode), only the image (and data) acquisition process needs a different procedure. There are more motivations to separate the image acquisition from the measurement:

- Because of the huge time demand of the image evaluation, taking it out increases the software frequency dramatically. In one program cycle the hard disk write requires the most time then.
- Development of separate software for strain measurements facilitates use with image series which have been saved with other devices (e.g. high speed camera), or combination with other tools (e.g. for full field strain analysis).
- Simplier menu system, easier programming.

2.1.4.1 Features of the image acquisition software

Based on the considerations above a video extensometer system was developed and implemented for various applications depending on the requirements of the specific test type:

- The first one was created for creep measurements, where only the time has to be saved with the images. Due to the really slow testing speed, the user is able to use filtering methods and different time steps for the image saving in the same measurement with 6 cameras parallel. A representative screen of the user interface is shown in Figure 2.4.

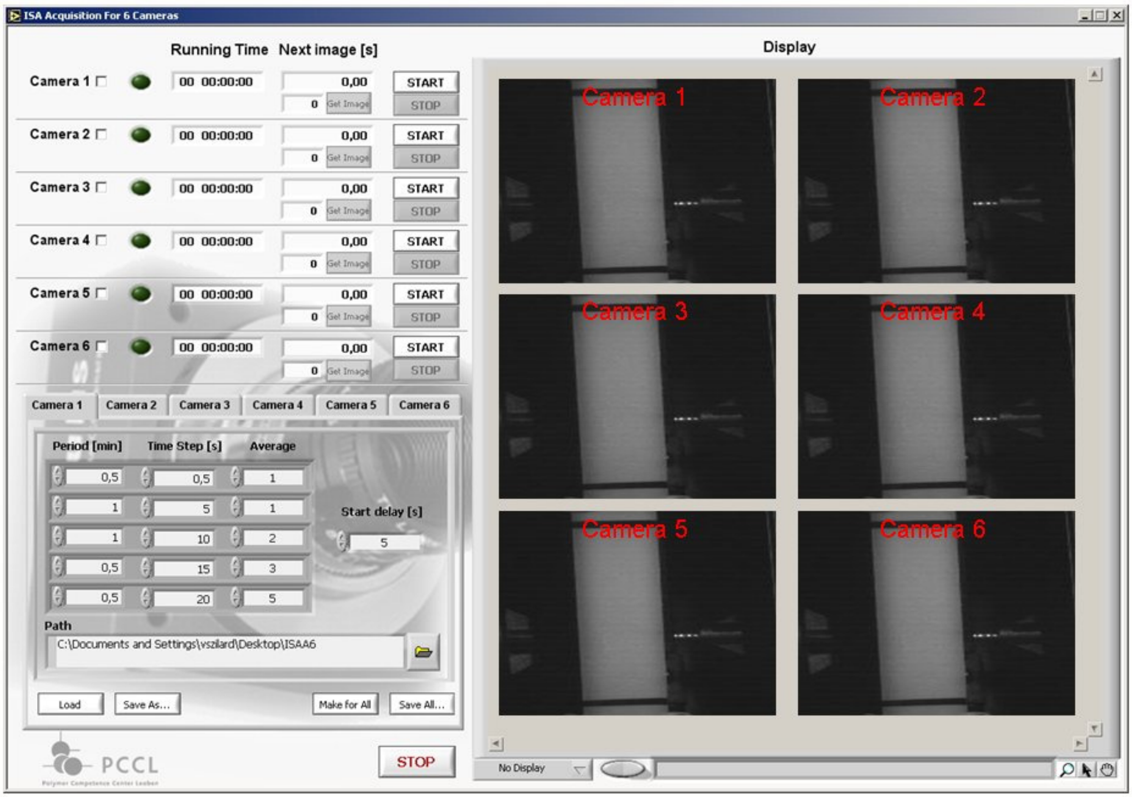

ISA Acquisition For 6 Cameras

	Running Time	Next image [s]	
Camera 1 ☐	00 00:00:00	0,00	0
Camera 2 ☐	00 00:00:00	0,00	0
Camera 3 ☐	00 00:00:00	0,00	0
Camera 4 ☐	00 00:00:00	0,00	0
Camera 5 ☐	00 00:00:00	0,00	0
Camera 6 ☐	00 00:00:00	0,00	0

Period [min]	Time Step [s]	Average
0,5	0,5	1
1	5	1
1	10	2
0,5	15	3
0,5	20	5

Start delay [s]: 5

Path: C:\Documents and Settings\vszilard\Desktop\ISAA6

Fig. 2.4: User interface of the image acquisition software for creep measurements with 6 cameras.

- For monotonic tensile and compressive tests to evaluate the test results, the software has to include the data acqusition process for the analogue signal of the force and global displacement values. This modification for one camera measurements can save more input signals together with the images and run much faster than the first one (~15Hz).

- Speed of the quickest version depends on the camera sampling rate, but it is applicable only for short testing period. In this case the images are saved to a memory buffer and transferred to the hard disk after finishing the data acquisition.

2.1.4.2 Determination of displacement and strain

The user interface for determining distances between the gage marks is shown in Figure 2.5. The green rectangles represent the different ROI-s where the edge (yellow) points have to be found, red lines are the fitted edges and the blue lines are the measured distances. On the top left corner is the grey level intensity of one ROI, which shows the black marker on the specimens with a valley.

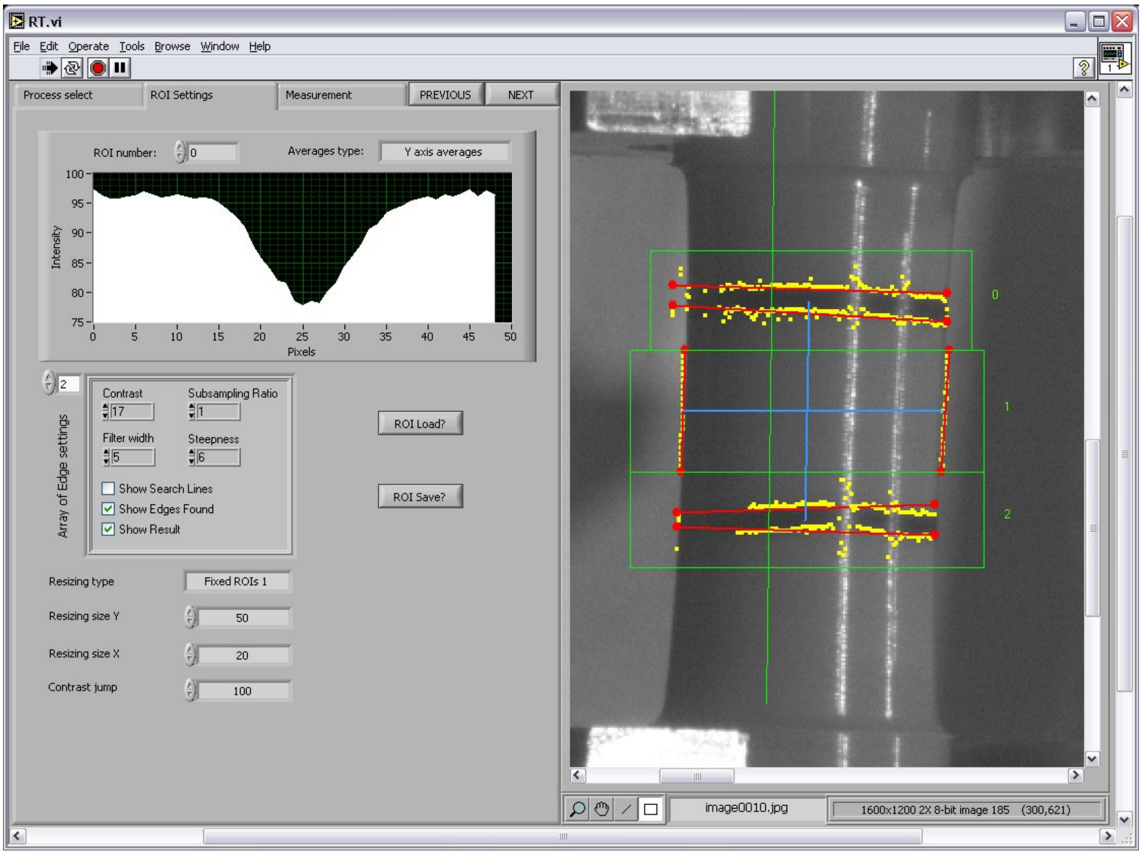

ROI number: 0

Averages type: Y axis averages

Array of Edge settings: 2

Contrast: 17

Subsampling Ratio: 1

Filter width: 5

Steepness: 6

☐ Show Search Lines

☑ Show Edges Found

☑ Show Result

Resizing type: Fixed ROIs 1

Resizing size Y: 50

Resizing size X: 20

Contrast jump: 100

image0010.jpg

1600x1200 2X 8-bit image 185 (300,621)

Fig. 2.5: User interface of the image measurement software.

2.2 Development of image acquisition software for cyclic tests

Because the evaluation of the saved images is possible with different specialized software (e.g. Aramis system, GOM, 2004), we focused on the image acquisition process to optically measure deformations and crack growth during cyclic tests. There are two possibilities:

- On one hand we could increase the acquisition speed at the expense of the resolution. It could be useful, when we are interested in the material response of one cycle, but it causes lot of unnecessary pictures and enhanced costs with long time tests.
- On the other hand, taking one photo in every cycle at the same position makes the images comparable with each other. Depending on the type of the stress (stretch or compression), we have to acquire the pictures exactly at the peak or at the valley of the displacement to capture the maximum strain, where the failures of the specimens are easily visible. For this exactly timed image acquisition a new method has been developed.

The software timing alone is not able to take pictures from a fast moving specimen in every cycle at the same position, because synchronization of the sequences of the camera, the testing machine and the software is difficult. Hence, we need to develop and apply a multi-function system, which is compatible with the existing testing machines or measuring tools. Therefore a special data acquisition card has to be used, which can generate a TTL trigger output signal when the input analog signal (e.g., force or displacement) reaches a specified value. This process is called “analog triggering” and was used in our software tool.

The system configuration is shown in Figure 2.6. The outputs of the test data (such as the displacement and force signals) of the testing machines (MTS 858 Polymer Test system and MTS 831 Table Top system) are connected to data acquisition card (NI PCI-6036E and BNC-2110) of the computer. We are able to set this special PCI card by the software in advance. After the configuration, this hardware can work with its own precise clock, independent from the state of the running program. At the moment where the input analog signal reaches a specified value, the acquisition card creates an output trigger signal. With this external trigger a previously prepared firewire CCD camera (Dolphin F201B) can take a precisely timed image from the measured specimen.

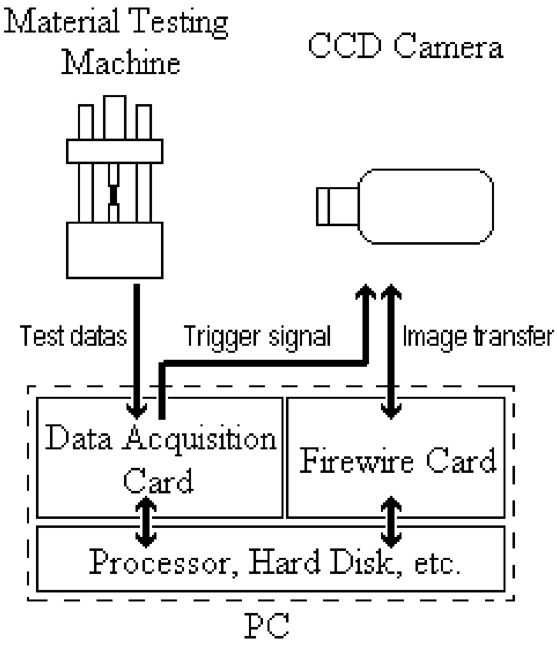

Fig. 2.6: System configuration for analog triggered image acquisition.

2.2.1 Program requirements

Due to the special requirements of the fatigue tests, the image acquisition software has to realize the following functions:

- To measure and compare the saved pictures, the images have to be acquired at the maximum strain (at the highest possible displacement point) of every cycle without any system stop. The possible maximum test frequency was defined at 50 Hz.
- The adjustable timing parameters of the data and images are especially important to manage the available free hard disk space. Sometimes a constant time distance is necessary, in other cases, the amount of images decreases or increases in the course of the experiment.
- A failure detection procedure enables automatic mode. In this case the software has to save the data from the last cycles retroactively.

The displacement maximum (or minimum) is also the best position for the image acquisition, as the low velocity improves the sharpness of the images, we can use less light, (which means less thermal radiation) with the same shutter speed of the camera. Because the hardware is not able to detect the maximum point of an analog signal, (which is near to impossible on a noisy curve in real time), only the crossing of the value on a rising or falling edge, we have to use different trigger processes for the displacement controlled and to the force controlled measurements. In the first case, the acquisition card generates the trigger with a delay of one quarter of the total cycle time from that point where the displacement signal reaches the mean value on the rising edge, as it is shown in Figure 2.7a.

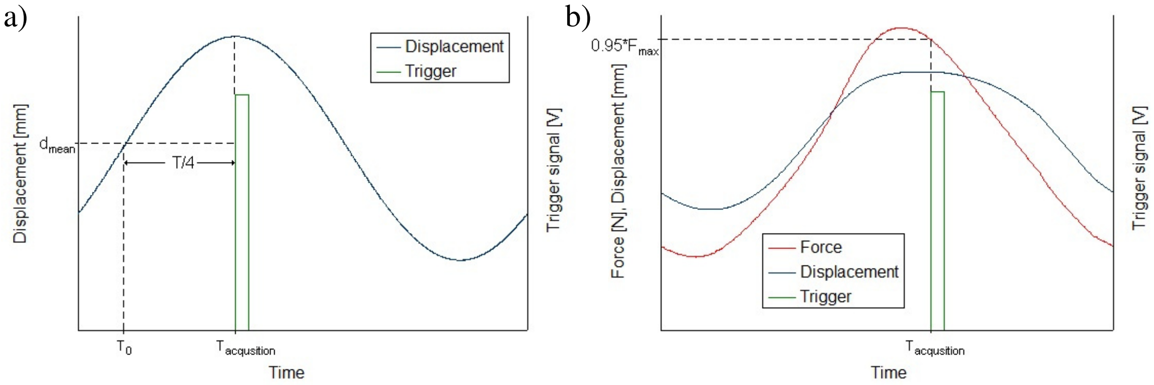

Fig. 2.7: Schematic representation of analog triggered image acquisition; displacement control (a), and force control (b).

However, the displacement is not symmetric using force controlled mode, so the trigger signal has to be created at a predefined point. Most of the time the 95% of the maximum force on the falling edge (Fig. 2.7b) was found to be the best solution, where the gradient is already high enough for a clear detection, but the specimen is still near to peaks (or valleys). Although that point is not exactly the displacement maximum, it does not affect the required results: the image acquisition time is always at the same position, which is saved, so they are measurable and comparable.

2.2.2 Program structure and modules

A representative screen of the user interface and the block diagram is shown Figure 2.8.

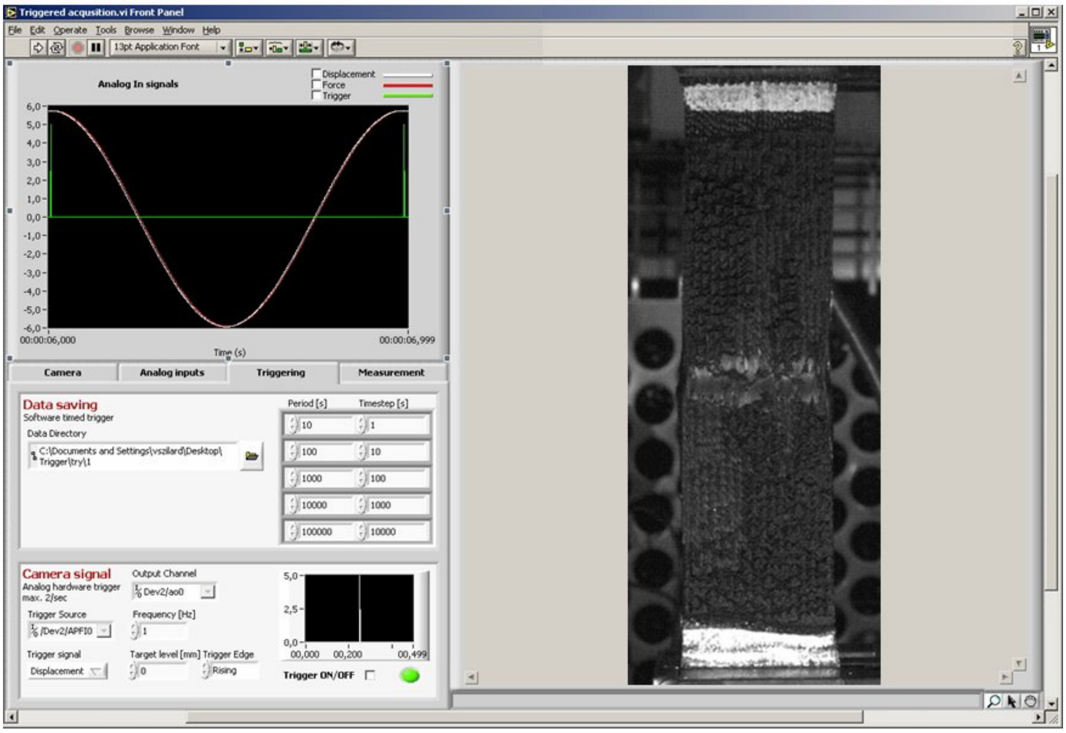

Software timed trigger

Data Directory: C:\Documents and Settings\vszilard\Desktop\Trigger\try\1

Period [s]	Timestep [s]
10	1
100	10
1000	100
10000	1000
100000	10000

Analog hardware trigger max. 2/sec

Output Channel: Dev2/ao0

Trigger Source: /Dev2/APFI0

Frequency [Hz]: 1

Trigger signal: Displacement

Target level [mm]: 0

Trigger Edge: Rising

Trigger ON/OFF ☐

Fig. 2.8: User interface of the software.

The following processes run parallel in the software:

- One program loop controls the user interface.
- Trigger signal generation: The pre-programmed acquisition card waiting for that level of the incoming signal, where the trigger has to be generated. The next cycle of this part will start, when the current picture saving is done.
- Data acquisition: The time and the trigger signal together with the force and the displacement signals of the testing machine are written into a controllable size buffer.
- Image acquisition: The images are also stored into a buffer. The maximum speed of this process is 3 frames per second at a resolution of 1600*1200 pixels using a commercial PC.

- Image and data save: The images and the signals acquired can be saved on user demand. The time interval between two storages may be constant, logarithmic scale or custom-set. The program saves one data block with one image from the buffers, and the recording time is marked by a tick.
- Failure detection: When the force or the displacement reaches a predefined limit (corresponds to a specific degree of material failure), all images and data are saved from the buffers, and the program stops. Due to this function the software tool runs automatically without the presence of an operator.

2.3 Example for force controlled cyclic experiments

To demonstrate the capabilities of the software package developed, both force controlled (uniaxial tensile fatigue of un-notched specimens) and displacement controlled (de Mattia Tests, ISO 132:1999) cyclic tests were performed with test specific constant stress (R_σ) and strain ratio (R_ε) values, and were subsequently evaluated.

First, cyclic tests were performed on un-notched cylindrical tensile specimens in uniaxial loading situation. Similar tests are described in the literature by Abraham (Abraham, 2005). The loading was force controlled with the maximum value of 1400 N and with the stress ratio 0.1. The nominal specimen diameter was 12 mm and the length between the fixtures was 24 mm. Gage marks were applied using an ink marker on the surface of the specimens with a gage length of 10 mm.

Hysteretic stress-strain curves with the position of the image data acquisition (red dots) are shown in Figure 2.9.

The three stages of the deformation and failure process are shown in Figure 2.10 with the TPU specimen. While Figure 2.10a shows the first loading cycle, Figure 2.10b shows the last cycle before ultimate failure. The broken specimen parts are seen in Figure 2.10c. These images represents one of the most important features of the acquisition software, that is, crack initiation and crack propagation can be detected and followed precisely. This is due to the fact that the images are precisely recorded at the maximum strain values.

The determination of the longitudinal strain by the camera was based on the recognition of these marks and the continuous measurement of the distance between the marks during the loading cycles. The exact determination of the strain was performed after completion of the test. The difference between the global displacement measured by the LVDT of the testing machine and the optically measured strains is shown in Figure 2.11.

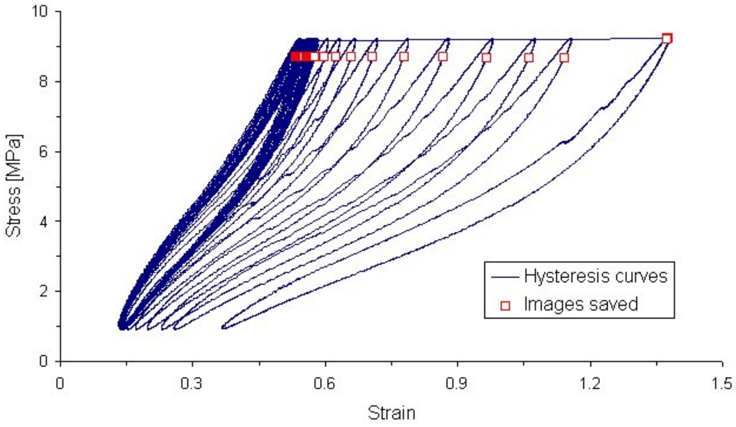

Fig. 2.9: Hysteretic stress-strain curves with the positions of the image data acquisition.

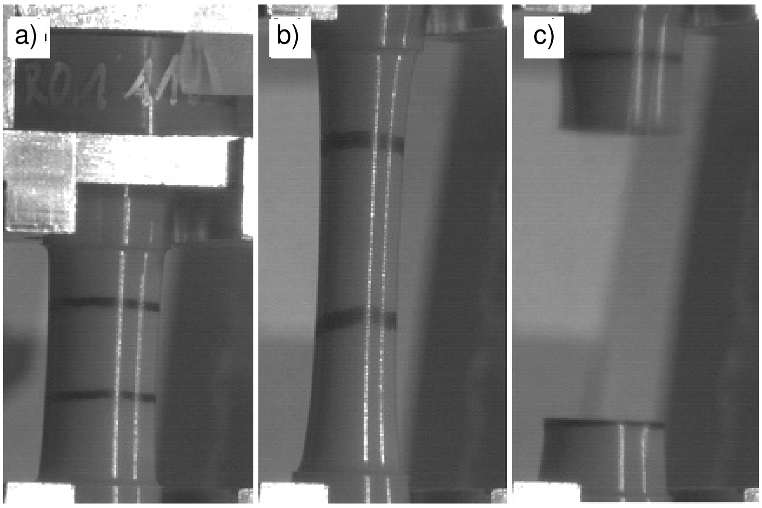

Fig. 2.10: Images from specimen fatigue stages.

At the start of the experiment, good agreement between the two strain values was observed; the difference between both values increases with increasing cycle number. The increasing slope of the curves indicates the start and evolution of the failure process. As failure is localized, only the local optical strain measurement provides the actual strain values.

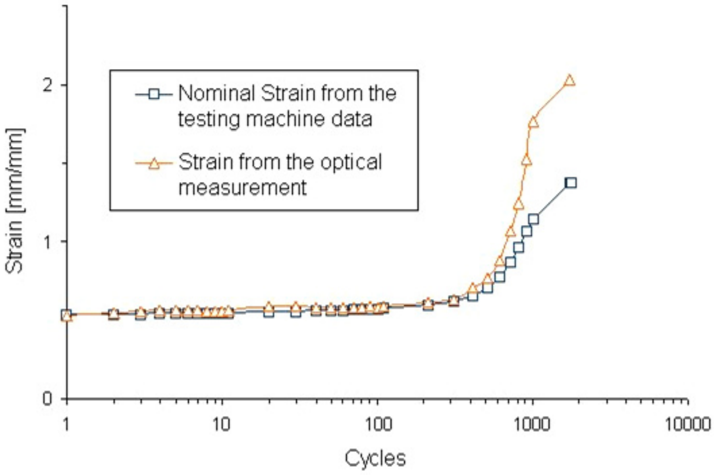

Fig. 2.11: Difference between the global strain calculated the by displacement measured using the LVDT signal of the testing machine and the optically measured strains.

2.4 Example for displacement controlled cyclic experiments

The de Mattia test is frequently used fatigue tests for the characterization of flex cracking and crack growth of non-conditioned thermoplastic rubber materials (ISO 132:1999). The vulcanized longish rubber specimen is loaded under displacement controlled cyclic load up to the maximum test amplitude of 57 mm and at a test frequency of 1 Hz. Figure 2.12 shows the trigger signal generation in the displacement valley points.

The damage and crack detection is based on visual observation and decision by the operator. After specified cycles the crack appearance (length and height of a semi-elliptical crack at the notch root surface) is classified from level 1 (occurrence of the first small cracks) to level 6 (the crack is longer than 3 mm in one direction). The measurement is documented in a chart and the averaged cycle number for the crack growth in class 3 is computed. However, due to the subjective determination of these crack levels the scatter of this test is very high and the reliability of the results is not sufficient for a clear distinction between similar material grades.

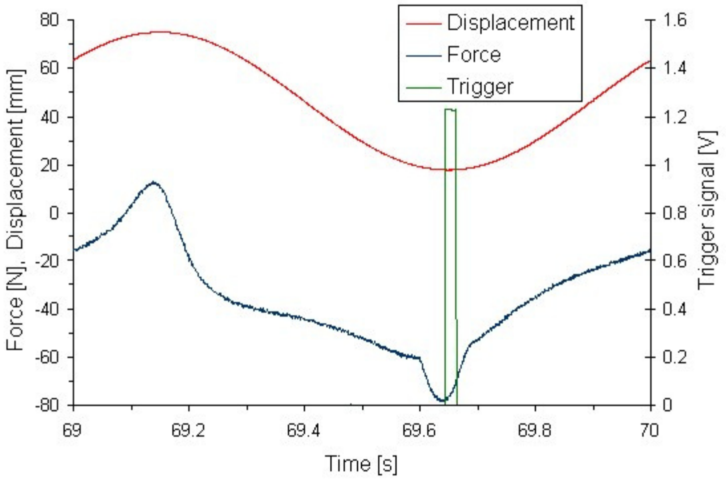

Fig. 2.12: Trigger generation for displacement controlled measurements.

The video extensometer with adequate image analysis can help us to reduce this scatter and provide more information about the crack initiation and growth process. Various stages of crack initiation and crack growth are shown in Figure 2.13.

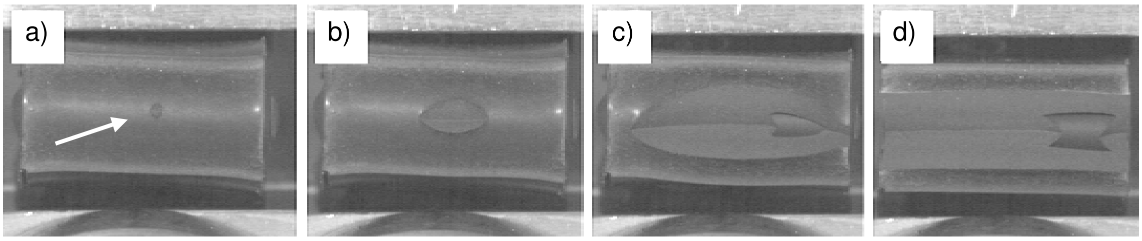

Fig. 2.13: Crack formation and propagation at the 57th (a), the 59th (b), the 60th (c), and at the 61st (d) cycle of the De Mattia test.

Crack initiation was observed after 57 cycles and is shown in Figure 2.13a. During crack propagation (from Figure 2.13b to c), in addition to the first crack, a secondary crack is also visible. In this case the standardized procedure would classify the crack as level 6 after 100 cycles. Using the software tool developed we are able to follow the details of crack initiation and growth so that drawing a distinction between different material grades becomes easier and more reliable.

2.5 Summary and conclusions

The characterization of the fatigue and fatigue crack growth behaviour of various engineering polymers is a challenging task. To gain more insight into the entire failure process and to properly characterize the fatigue behaviour of engineering polymers novel measurement and test methods are needed. The recent development of non-contact optical test methods, hardware and software tools provide big potential for this fatigue experiments. On a laboratory test specimen level the non-contact optical methods may provide more accurate strain information over a large deformation range (an important aspect in the testing of soft thermoplastics and elastomers) and the contact problems associated with conventional contact methods (i.e. adhesive specimen interaction at strain gages, local deformation and/or slippage of the mechanical extensometer tips and knife edges) can be avoided.

Conventional video extensometers were developed and mainly used for long-term static and for slow monotonic loading conditions. Furthermore, from a measurement technique point of view the main difficulty of the fatigue test lies in the periodically changing load and displacement signal during the test. Moreover, due to the inherent viscoelastic behaviour of the engineering polymers, a phase shift between the force and displacement signal exists. Hence, for a proper cyclic measurement the analog output signals of the material testing machines have to be synchronized with the image data acquisition of the video extensometer.

To achieve this and to support the characterization of engineering polymers under fatigue test conditions, a novel modular software tool was developed and implemented. This software tool consists of several modules which can be used both stand-alone or can be combined or used with external software tools. When applying this software tool the hardware can precisely trigger the image acquisition during the cyclic tests both for displacement and for force controlled loading at the maximum or minimum of the loading. Hence, a viscoelastic analysis of the force and strain signals is also possible. To demonstrate the capabilities of the developed software tool, two types of cyclic tests were carried out under displacement and force controlled loading conditions, as described in this chapter.

As these test examples have clearly shown, by applying this software tool it is possible to observe both the strain history and the kinetics of the failure of the specimens under cyclic loading conditions. Furthermore, due to the time consuming character of the fatigue tests, it is extremely important to save on operator time, which is also possible by applying this method. Moreover, with a proper combination of the image data acquisition and the strain measurement module, the software would allow to perform local strain controlled cyclic tests using both nominal and true strain values as control signal.

The software tool developed and described in this section is documented in the Appendix of this thesis. The CD/DVD contains all LabVIEW software modules along with a short manual for further applications.

References

F. Abraham, T. Alsuth, S. Jerrams (2005): „The effect of minimum stress and stress amplitude on the fatigue life of non strain crystallizing elastomers”, Materials & Design 26, pp. 239-245.

R. Brown (1999): „Handbook of polymer testing: physical methods”, CRC Press, pp. 229-232.

L. Casarotto. R. Tutscha, R. Rittera, H. Dierkeb, F. Kloseb, H. Neuhäuser (2005): „Investigation of PLC bands with optical techniques”, Computational Materials Science 32, pp. 316-322.

DIN ISO 132 (ISO 132:1999): „Rubber, vulcanized or thermoplastic – Determination of flex cracking and grack growth (De Mattia)”.

GOM (2004) - Gesellschaft für Optische Messtechnik GmbH: „Aramis User Manual”, Braunschweig, D.

M. Jerabek, Z. Major, R.W. Lang (2010): „Strain determination of polymeric materials using digital image correlation”, Polymer Testing 29, pp. 407-416.

National Instruments Corporation (2003): „LabVIEW User Manual”.

National Instruments Corporation (2000): „IMAQ Vision for LabVIEW User Manual”.

M. Sasso, G. Palmieria, G. Chiappinia, D. Amodioa (2008): „Characterization of hyperelastic rubber-like materials by biaxial and uniaxial stretching tests based on optical methods”, Polymer Testing 27, pp. 995-1004.

Sz. T. Vezér (2004): „Automatization of the strain controlled tensile test of polymers and theirs composites”, Diploma Thesis, Technical University Budapest, Department of Polymer Engineering.

3. CHARACTERIZATION OF THE BULK FATIGUE PROPERTIES

3.1 Introduction and objectives

The contact sections of the elastomer surfaces are exposed to dynamic stretching under multiaxial fretting conditions. The contact sliding and fatigue process was experimentally characterized and simulated as described in chapter 1. To establish well-founded relations between the surface and bulk fatigue behaviour, conventional force controlled uniaxial fatigue measurements were performed and are analysed in this chapter. The characterization of the bulk fatigue behaviour for both elastomer types can help to understand the reasons of fretting fatigue and is damage kinetics.

The characterization of the fatigue behaviour of rubber-like materials is still a significant research area (Mars, 2004). Even though a number of studies have already been published in this topic, there is a lack of an accurate description of damage accumulation under cyclic loading conditions, and the specific mechanisms are not well known either. This lack is due to the huge amount of time, which these experiments require and due to the complex interactions of environmental and material properties.

Three basic methods have been frequently used to determine the material fatigue strength of elastomers (Bauman, 2008). While the first two of these methods determine the fatigue life-time in terms of the cycles-to-failure (N_f) for a specified level of loading, the third uses crack growth rate (da/dn) and fracture mechanics parameters:

- The most traditional measurement type is the stress-number of cycles-to-failure method (nominal stress Wöhler curve), where the fatigue life-time estimation is based on the applied stress level only.
- The strain-life time diagrams show more details of the localized plastic deformation and are frequently used for low cycle (less than 10^3) fatigue investigations.

- The fracture mechanics approach assumes an existing crack. Crack growth is continuously measured, and the crack growth rate is calculated therefrom. The load in the vicinity of the crack tip is either described by the stress intensity factor or by the energy release rate, and these values are represented together with the crack growth rate in a kinetic diagram. Fracture mechanics fatigue tests are timesaving and frequently applied for a fast material comparison.

The following fatigue literature overview implicates a focus on the stress-based method in this chapter because it is the dominant loading mode under fretting contact.

The objectives of this chapter:

- Conventional force controlled cyclic experiments will be performed on both elastomer types and nominal stress based Wöhler curves will be determined.
- In addition to this conventional data reduction technique and to gain more insight into the kinetics of the failure process, the hysteretic curves will be recorded, analyzed and some relevant parameters along with their characteristic tendencies will be determined. The crack initiation will be detected by optical methods, and crack growth will be measured using the method described in the previous chapter (Chapter 2).
- Furthermore, displacement controlled uniaxial tensile test method using a novel smooth notched “Diabolo-type” specimen geometry along with an appropriate test set-up for cyclic loading will be developed and local strain based Wöhler curves will be constructed.
- Moreover, cyclic torsion tests applying the same specimen geometry and similar test configuration with axial displacement constraint will also be developed and implemented and shear stress based Wöhler curves will be constructed.
- Finally, all these methods will be applied to characterize and compare the fatigue behaviour of the HNBR and the TPU materials.

3.1.1 The stress-life method

The first description of the stress-life method for metals was published by Wöhler for railway axles (Wöhler, 1867). Nowadays the maximum stress limit determination of the infinite fatigue life has become the basic part of all fatigue analysis (Figure 3.1). This endurance limit (σ_e) is usually 35-50% of the tensile strength for most steels and copper alloys (Suresh, 1998). The relation between the stress level and the fatigue life has been described by Basquin for stress-controlled fatigue conditions (Basquin, 1910):

$$\sigma_a = \sigma'_f \cdot (2 \cdot N_f)^b \tag{3.1}$$

where σ_a is the stress amplitude, σ'_f is the fatigue strength coefficient, b is the fatigue strength exponent and $2N_f$ is the number of cycles to failure.

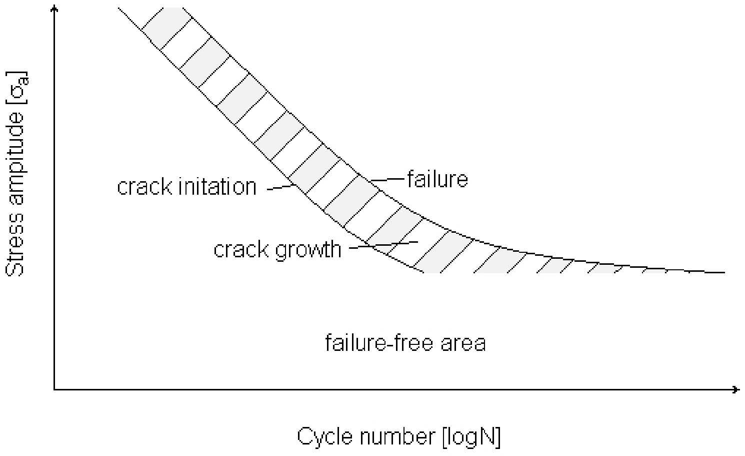

Fig. 3.1: General Wöhler diagram.

3.1.2 Fatigue life and damage accumulation theories

A comprehensive review of various fatigue damage accumulation models mainly for metallic materials is provided by Fatemi (Fatemi, 1998). This review contains the following main linear and non-linear damage accumulation models.

The earliest cumulative fatigue damage model is called the ‘linear rule’ and has been described by Miner (Miner, 1945). The mathematical form, where the damage denoted by D, the number of the cycles is n_i and the total cycles to failure is N_{fi} is written as:

$$D = \sum r_i = \sum \frac{n_i}{N_{fi}} \tag{3.2}$$

where i represents the stress level.

Failure occurs when the sum of the stress level dependent cycle ratio $\sum r_i=1$. The two stage linear damage model of constant load amplitudes separates the fatigue process into two stages, the first one due to the crack initiation ($N_I=\alpha N_f$), and the second one due to crack propagation: ($N_{II}=(1-\alpha)N_f$), where α is a life fraction factor (Grover, 1960).

The first non-linear model has been published by Marco and Starkey (Marco, 1954) and defines the damage as follows

$$D = \sum r_i^{x_i} \tag{3.3}$$

where x_i relates to the stress level. Based on other damage accumulation approaches, Bui-Quoc published his hybrid theory, which later has been adapted also for creep and also for fatigue damage conditions. The basic idea of this model was the continuous material strength reductions due to the crack growth inside (Bui-Quoc, 1975). All parameters are described with dimensionless ratios with respect to the endurance limit σ_{eo}.

$$D = \sum \frac{1-\gamma_e}{1-\gamma_{ec}} = \sum \frac{r}{\left(r + (1-r) \cdot \frac{\gamma - (\gamma / \gamma_a)^m}{\gamma - 1} \right)} \tag{3.4}$$

where $\gamma_e=\sigma_e/\sigma_{eo}$ is the instantaneous endurance limit, $\gamma_{ec}=\sigma_{ec}/\sigma_{eo}$ is the critical endurance limit to failure, $\gamma=\sigma/\sigma_{eo}$ is the applied stress ratio, γ_a and m are material constants.

Furthermore, also some more special theories based on fracture mechanics considerations are in summarized by Fatemi (Fatemi, 1998) for fatigue of metals, e.g. the double damage curve model or various crack growth damage approaches, which have been developed from linear elastic fracture mechanics. Moreover, based on Griffith's damage theory, Rivlin devised his tearing energy criterion, which was a specimen form independent approach for fatigue failure of elastomeric materials (Rivlin, 1953). He described the connection between the internal energy and required energy for new surface creation in crack growth processes. Greensmith determined the tearing energy for uniaxial tension, and Gent used this theory for his investigations of the fatigue behaviour (Greensmith, 1963; Gent, 1964). Many failure criteria are built on energy based damage models in present times (Kim, 2004; Lazzarin, 2008). It has been observed that, by using strain energy as a parameter, one is able to unify the damage caused by different types of loading. Determination of the energy states of material fatigue makes the evaluation of stress-strain hysteresis curves one of the basic tool for fatigue assessment.

3.1.3 Hysteresis analysis

During stress controlled dynamic fatigue measurements the form, the size, and the frequency of the applied stress signal has to be defined and controlled. The size parameters are the mean stress (σ_m) and the stress ratio (R). One of these two values has to be fixed for the fatigue test series to describe the material behaviour in a Wöhler diagram.

$$\sigma_m = \frac{(\sigma_{\max} + \sigma_{\min})}{2} \qquad (3.5)$$

$$R = \frac{\sigma_{\min}}{\sigma_{\max}} \qquad (3.6)$$

Stress-life theories focus on the crack nucleation with the help of the material history and try to describe the fatigue limit as a function of one mechanical property, like the maximum principal strain or the strain energy density (Mars, 2002). These values are determined from hysteresis cycles of the stress-strain curves as it is shown on Figure 3.2.

To describe the fatigue crack nucleation of elastomers, the maximum stretch ratio ($\lambda_{maxi}=\varepsilon_{maxi}+1$), the maximum principal stress and some further developed predictors (i.e., dynamic modulus, various energy parameters) are widely used (Verron, 2008; Woo, 2008). The change of the dynamic modulus, E* describes damage accumulation and has commonly been used as a failure criterion:

$$\left|E^*\right| = \left|\frac{\sigma_{\max} - \sigma_{\min}}{\varepsilon_{\max} - \varepsilon_{\min}}\right| \tag{3.7}$$

where $\sigma_{\max}$, ($\sigma_{\min}$) and $\varepsilon_{\max}$ ($\varepsilon_{\min}$) are the maximum (minimum) point of the stress and strain values in one cycle of the fatigue measurement (Altstädt, 1987; Zahnt, 2003).

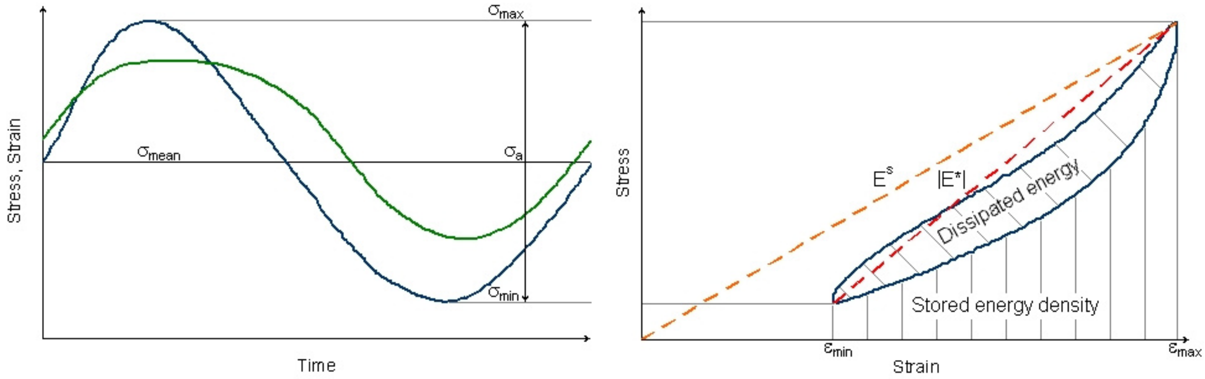

Fig. 3.2: Evaluation of the hysteresis curves from the stress-, strain -time diagram (hyperelastic material, $\sigma_a>0$, R>0).

Other approaches use the secant modulus, E^s to determine creep and damage accumulation (Hwang und Tan, 1989; Talreja, 2001):

$$E^s = \begin{cases} \dfrac{\sigma_{\max}}{\varepsilon_{\max}} & if \quad R < 1 \\ \dfrac{\sigma_{\min}}{\varepsilon_{\min}} & if \quad R > 1 \end{cases} \tag{3.8}$$

Damage can be determined by the reduction of this secant modulus, such as in dynamic creep, which is reflected by the secant modulus change when the mean stress is higher than zero. Not only the stress-strain limits, but also the forms of the loading and unloading curves are able to define some kind of fatigue damage of the tested materials. Furthermore, strain energy became also a predictor of the fatigue crack initiation (Beatty, 1964). The total strain energy density U_t is the elastic strain energy per volume unit of the material and can be calculated from the loading part of the hysteresis curves with the following equation:

$$U_t = \int_{\varepsilon_{\min}}^{\varepsilon_{\max}} \sigma \cdot d\varepsilon \tag{3.9}$$

The stored (recovered) energy, U_{st} is the integral of the unloading slope, and the dissipated (lost) energy, U_d is the closed area of the hysteresis curve:

$$U_{st} = -\int_{\varepsilon_{\max}}^{\varepsilon_{\min}} \sigma \cdot d\varepsilon \tag{3.10}$$

$$U_d = U_t - U_{st} \tag{3.11}$$

Strain energy density has successfully been implemented into several fatigue studies of rubbers (Oh, 1980; Grosch, 1988) for applications.

3.1.4 Softening Wöhler curve

Determinations of the fatigue limit for various polymeric materials have been provided by several authors of the research group based on the dynamic modulus method (Zahnt, 2003; Pinter, 2006). With the calculation of the instantaneous and the maximum value of the dynamic modulus ratio (E^*_i/E^*_{max}) a further development of this method is possible when the relation to the cycle number and to the applied stresses are defined. This is depicted in Figure 3.3a. Figure 3.3b shows the dynamic modulus as a percentage of the maximum value and as a function of the cycle number, which results in so-called softening Wöhler curves.

The determination of the dependence on the applied stress and the cyclic number, Wöhler curve can be defined at any dynamic modulus degradation as it is shown in Figure 3.4.

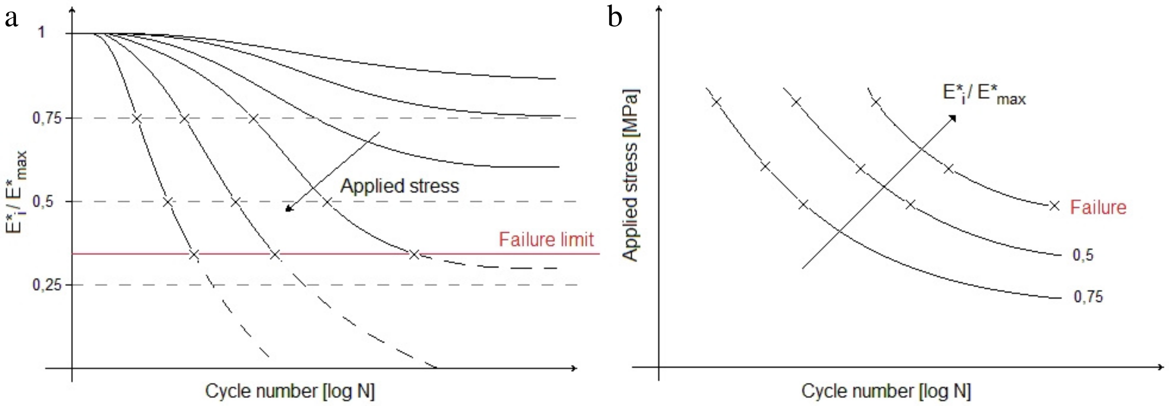

Fig. 3.3: Decrease of the dynamic modulus (a) and evaluated softening Wöhler curves (b).

Both the experimental details and the data reduction scheme of this method along with representative results are presented in section 3.2.2.6 for the fatigue tests of the TPU material.

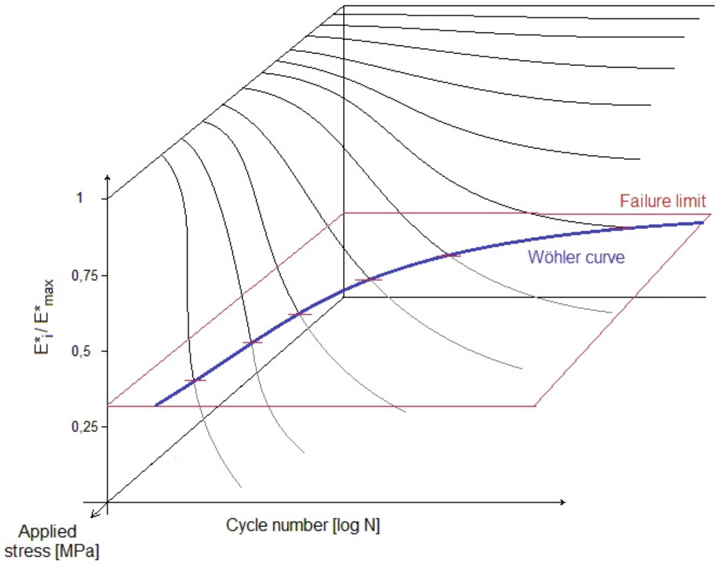

Fig. 3.4: Evaluation of the Wöhler curve at the given dynamic modulus change.

3.2 Stress controlled fatigue tests

3.2.1 Fatigue experiments

<u>Test specimens</u>

Cylindrical dumbbell test specimens were produced by SKF Economos (Judenburg, A) using a hydrogenised nitrile rubber (HNBR) in the investigations. The test samples have a nominal diameter of Ø14 mm and three different surface roughness values (OF1, OF2 and OF3) were manufactured on the material surfaces by turning with a length of 13 mm (Figure 3.6a). The surfaces were characterized by confocal microscopy (FRT, Bergisch Gladbach D). Surface topography images of the cylindrical surfaces for the various roughness levels are shown in Figure 3.5.

Similar fatigue experiments were carried out on a thermoplastic polyurethane (TPU) material. In this case specimens with only one surface roughness were tested. Due to the higher stiffness of the TPU, the cross section was reduced (nominal diameter of Ø 8 mm), and an additional shoulder was machined in the specimen as it is shown in Figure 3.6b. For the stress-strain calculation, the nominal gage length (l_0) was taken as 30 mm for the HNBR and 15 mm for the TPU specimens.

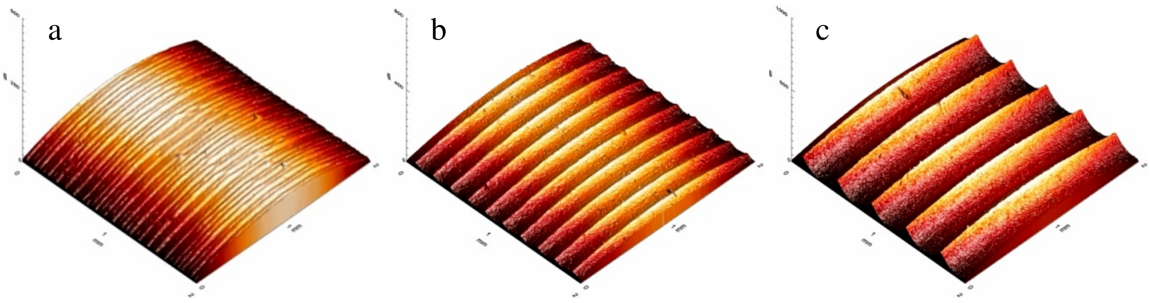

Fig. 3.5: Confocal scanning microscope images of the specimen surfaces; OF1 (a) with Ra=0.962 µm, OF2 (b) with Ra=3.954 µm, and OF3 (c) with Ra=8.257 µm.

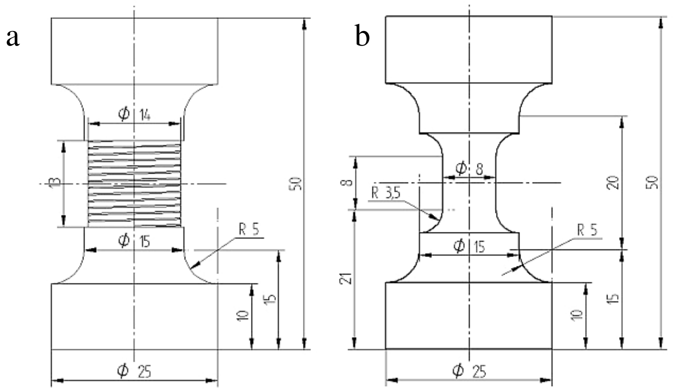

Fig. 3.6: Dimensions of the fatigue test specimens: HNBR (a) and TPU (b).

Test system and parameters

A servohydraulic test system (MTS-858 Tabletop, MTS Systems GmbH, Berlin, D) was used for the fatigue experiments. The tests were carried out with the following parameters:

Testing mode: force controlled
Temperature: 23 [℃]
Frequency: 1 [Hz]
Stress ratio ($R=\sigma_{max}/\sigma_{min}$): 0.1

Maximum force:	1200 [N]	σ= 7.8 [MPa]	for HNBR
	1500 [N]	σ= 29.7 [MPa]	for TPU
Maximum number of cycles:	$4{,}32*10^5$	5 days	for HNBR
	$8{,}64*10^4$	1 day	for TPU

Test methods

During the measurements the time, the cycle number, the displacement and the force values were saved in a logarithmic scale for the hysteretic analysis (Pinter, 2006). The data saved contains the last 10 cycles before failure, and with the developed analog triggered image acquisition software we are able to see the damage processes also. This software was described previously in detail by Vezér (Vezér, 2008) and in chapter 2 further details were provided along with additional applications. The stages of crack initiation and growth for HNBR are shown in Figure 3.7.

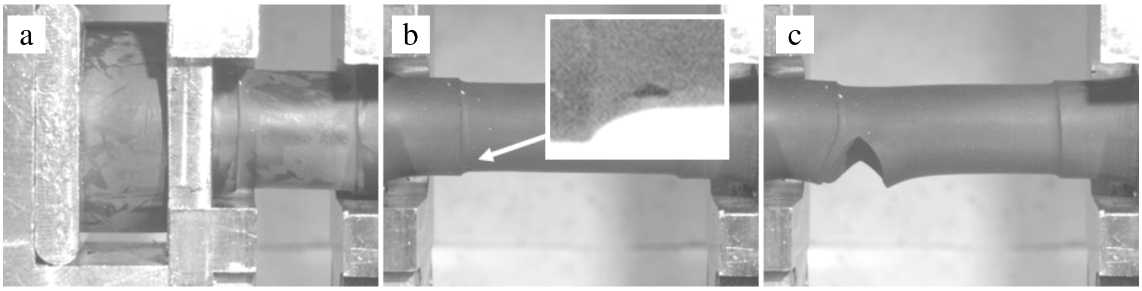

Fig. 3.7: Stages of the crack formation in a rubber specimen: stress free state (a), 10^4 cycles before the failure (b), last cycle (c).

To characterize the damage accumulation process (including visible and non visible crack formation) and to describe the change of the material attributes, the following values were calculated with the LabVIEW (NI, San Antonio, TX, USA) evaluation software:

- stress – strain and secant modulus – dynamic modulus
- strain energy density – dissipated energy density – stored energy density.

Finally, the data reduction of the force controlled fatigue experiments consists of the following elements:

- Fatigue surface analysis

- Construction of conventional Wöhler curves by using cycles to final failure, N_f values and proposal for a critical fatigue stress and/or life time estimation
- Detection of the onset of crack initiation and estimation of crack growth parameters by non-contact image analysis
- Analysis of the hysteretic behaviour

A novel softening-type fatigue analysis method based on the Wöhler-curve approach was also proposed.

3.2.2 Test results and discussion

3.2.2.1 Fatigue surface analysis

To determine reliably the surface roughness dependence of the fatigue behaviour, fatigue surfaces were analyzed by a stereo light microscope. Three different fracture types were observed and are depicted in Figure 3.8 for comparison. Crack initiation was observed on the specimen surface without a sharp edge of the cutting tool (Figure 3.8a), internal defects in the bulk material (Figure 3.8b) and crack initiation at the sharp notch caused by the cutting tool (Figure 3.8c). The internal failure has nearly the same ratio for all kind of surface roughness, 14% (OF1), 8% (OF2) and 8% (OF3) was perceptible.

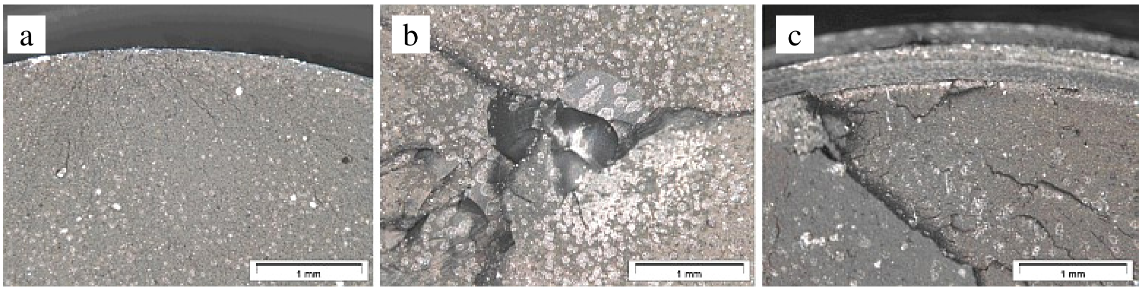

Fig. 3.8: Crack initiation types on the side (a), by a material failure (b), on the start position of the cutting edge (c).

There are significant deviations in these crack initiations which were caused by the production process (cutting tool). While every 5th piece of the OF3 samples (20%)

failed in this mode, OF1 reveals only one such failure (5%). Failure modes b and c (Figures 3.8 b and c) were considered as not relevant for fatigue behaviour of HNBR and were left out from further investigations.

	Mode a	Mode b	Mode c	Cracked at the clamps	∑
OF1	62 %	14 %	5 %	19 %	100 %
OF2	72 %	8 %	0 %	20 %	100 %
OF3	68 %	8 %	20 %	4 %	100 %

Table 3.1: Distribution of the investigated crack initiations with the different surface roughness tested.

3.2.2.2 Wöhler curves

Hence, the Wöhler curves were constructed using the first type of the fatigue behaviour. Based on these results, there is no clear effect of the surface roughness observable in the fatigue life times.

The combined Wöhler curve for all data points is shown in Fig. 3.9 with the following nonlinear fitting function:

$$\sigma_{\max} = 3.7137 + \frac{109.6656}{\sqrt{N_f}} + \frac{-625.8976}{N_f} \tag{3.12}$$

where N_f is the fatigue life time in cycles, and $\sigma_{\max}$ is the maximum stress of a cycle in MPa. The fitting function was selected due to its asymptotic character and revealed the best possible fit of the data points.

From equation 3.12, the fatigue life as a function of the maximum stress is:

$$N_f = \left(\frac{-1.252 \cdot 10^3}{\sqrt{(-2.504 \cdot \sigma_{\max} + 213.2419) \cdot 10^3} - 1.0967 \cdot 10^2} \right)^2 \tag{3.13}$$

The threshold value of the maximum uniaxial stress, where no failure will occur, is computed as:

$$\lim_{N_f \to \infty} \sigma_{\max}(N_f) = 3.73 \ [MPa] \tag{3.14}$$

Due to the trend of the data points determined, it was assumed that a distinct failure limit exists for HNBR. This assumption is supported by several literature data (Hirakawa, 1978; Mahmoud, 2007; Woo 2008).

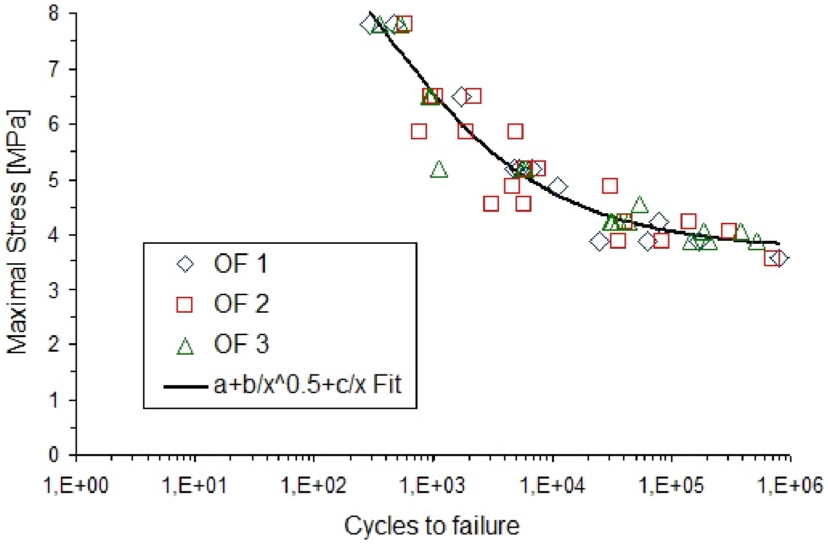

Fig. 3.9: Combined Wöhler diagram of the three different surface roughnesses.

It must be noted, however, that the quality and character of a number of Wöhler curves published (Abraham, 2005; Kim, 2004) does not allow for any clear statement in this question. For metallic materials the basic crystalline structure clearly determines the existence of the fatigue limits, it exists for body-centered-cubic metals (iron, chromium etc.) and does not exist for face-centered-cubic crystals (aluminium, copper etc.) (Berger, 2008). In contrary, due to the more complex microstructure of elastomers and due to the processing dependence of the material behaviour, no such distinction has been found. In addition to the mechanical loading induced failure, due to aging/degradation elastomeric materials may change their microstructure and mechanical behaviour over a long time. Hence an accurate forecast is extremely difficult.

In contrary to HNBR, the determination of the Wöhler curve for TPU was not successful using the method described above. Under similar cyclic loading conditions only one TPU specimen failed in one day. Under 1500 N maximum force (corresponds to a nominal stress of σ= 29.7 MPa), final fracture was observed after 1782 cycles. Hence, keeping the basic idea of the Wöhler curve but completing them with a material specific aspect, a novel softening-type Wöhler curve was developed and is described in section 3.1.4. The results of these experiments are explained in section 3.2.2.6.

3.2.2.3 Crack initiation

Figure 3.10 shows an example for the various stages of the observable crack propagation with the HNBR material. In virtue of the acquired images, saved and the calculated parameters (i.e., force-displacement, dynamic modulus, energy), rapid crack propagation was the representative failure behaviour for both elastomeric materials after long term cyclic loading.

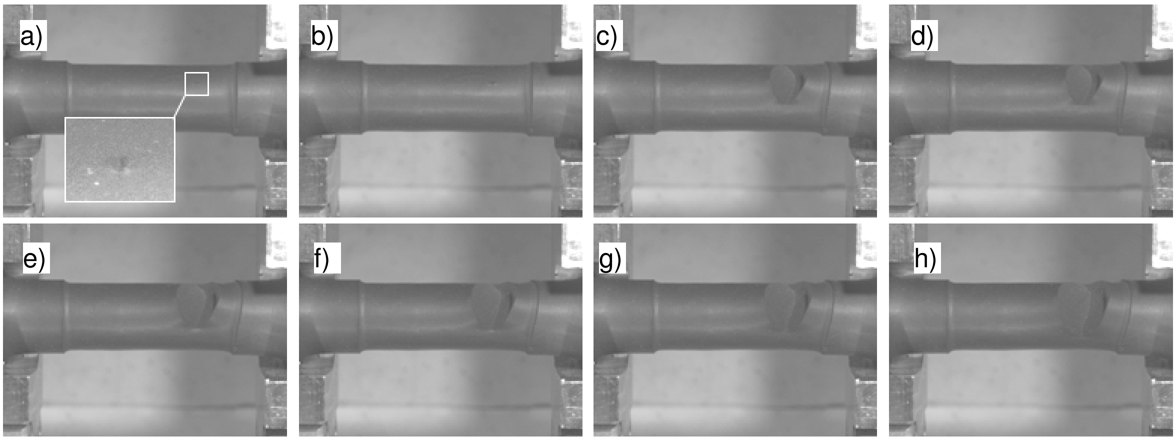

Fig. 3.10: Macroscopic crack propagation of the HNBR material under 4 MPa maximum stress: images after 50000 (a), 60000 (b) and 10 (c), 9 (d), 4 (e), 3 (f), 2 (g), 1 (h) cycle before the final failure occurred.

The appearance of visible cracks is confined to the last 10-100 cycles for HNBR and to only less than 5 cycles for the TPU materials. The images in Figure 3.10 show a special case.

Macroscopic crack initiation was observed and recorded already after 50000 cycles (Figure 3.10a), there was no propagation during the next 10000 cycles (Figure 3.10b) and the acquired 10 last images present the final failure (Figure 3.10c to h). From the images recorded the crack tip opening distance was determined; it is shown in Figure 3.11a at a selected cycle number. The crack growth rates are calculated and presented in Figure 3.11b, where the rapid failure in the last few cycles is well visible.

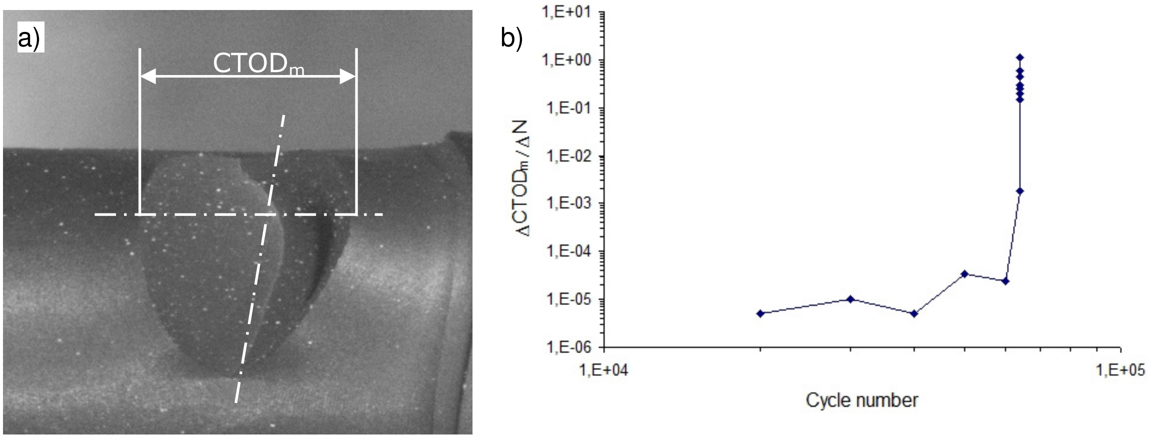

Fig. 3.11: Position of the measured crack tip opening distance (CTOD$_m$) (a), and the crack grow rate as a function of the cycle number.

The corresponding hysteresis curves measured during this test are visible in Figure 3.12. The marks show the position of the images. No significant or sudden change is visible on the hysteresis curves during the cyclic loading and the crack growth process expected. The shape of the hysteretic curves changes continuously but without a clear indication of the onset of crack initiation and crack growth. This continuous and stable failure process is analyzed in the following Figures in terms of dynamic and secant modulus values.

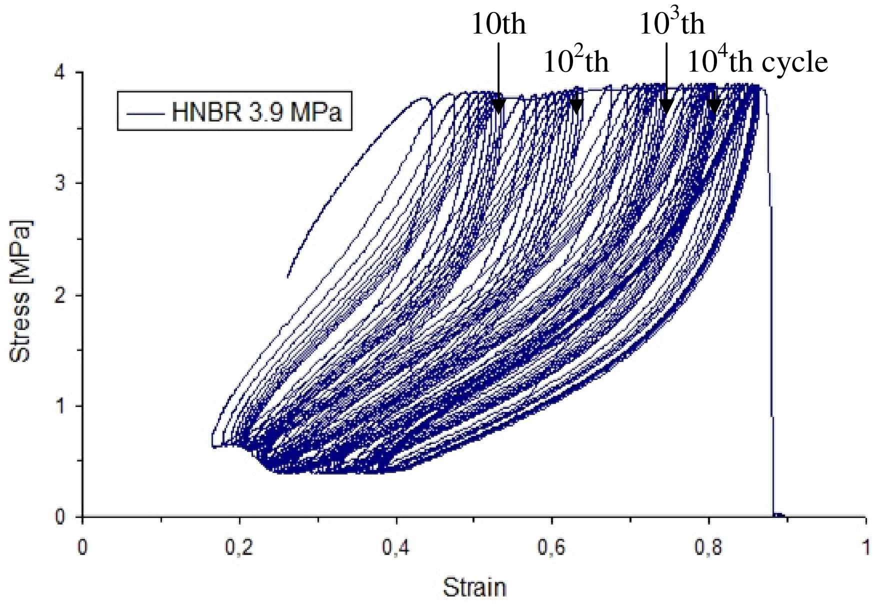

Fig. 3.12: Hysteresis curves of the selected HNBR fatigue measurement with 4 MPa maximum stress.

Figure 3.13a shows the dynamic and secant modulus change during the fatigue measurement. The crack growth effect is visible in Figure 3.13b, where both values decrease until material failure. The total strain energy density and the dissipated energy densities are shown in Figure 3.14a. After 1000 cycles both values decrease, but during the crack growth process (Figure 3.14b) the dissipated energy grows due to the energy demand of the new surfaces.

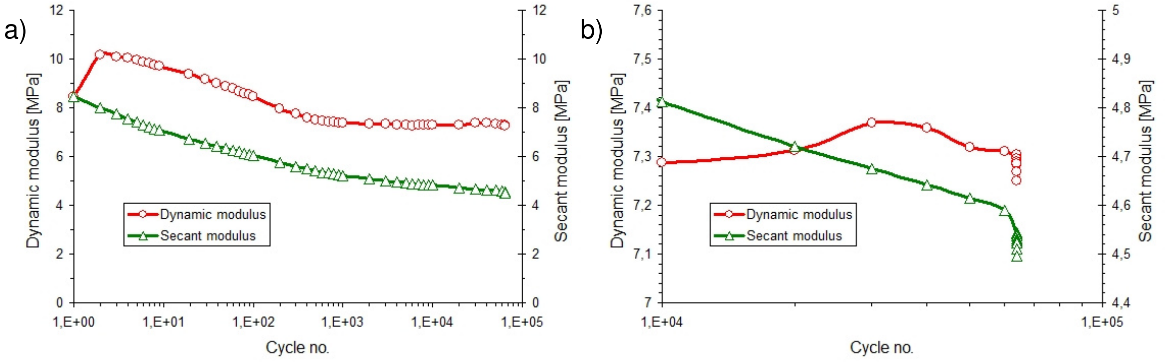

Fig. 3.13: Changing of the secant and the dynamic modulus of HNBR (a), and the effect of the visible crack propagation on their values (b).

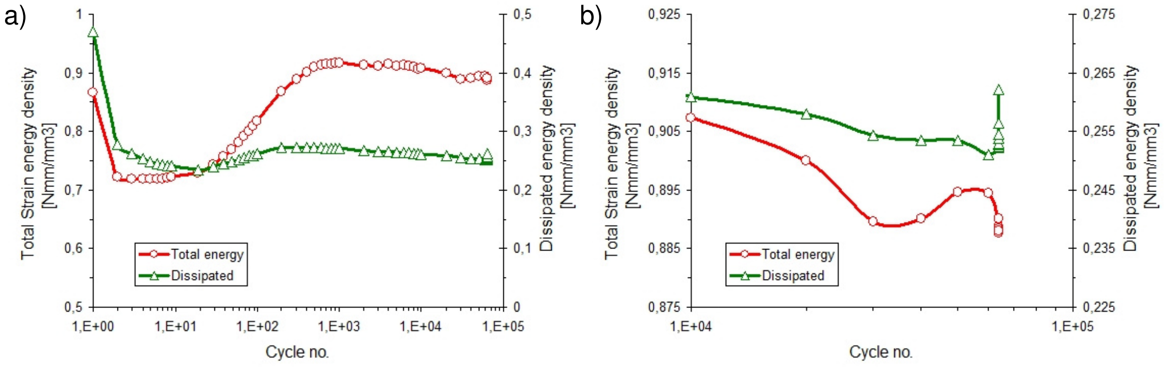

Fig. 3.14: Changing of the total and the dissipated strain energy density of HNBR (a), and the effect of the visible crack propagation on their values (b).

3.2.2.4 Hysteresis analysis of the HNBR material

As only negligible differences were observed between the fatigue results of specimens revealing different roughness values, for the hysteretic analysis only the OF1 (smallest roughness) specimens were investigated. Typical hysteresis curves are shown in a σ-ε diagram in Figure 3.15, where the S-shaped curves

(Bennani, 2003) shift with time, whereas the similar $\Delta\varepsilon$ values and energy areas of the cycles are well visible. This special behavior (no change of the shape of the curve, only a horizontal shift) of the material makes the usage of the calculated and plotted lifetime predictors (dynamic modulus, strain energy density) difficult with HNBR materials.

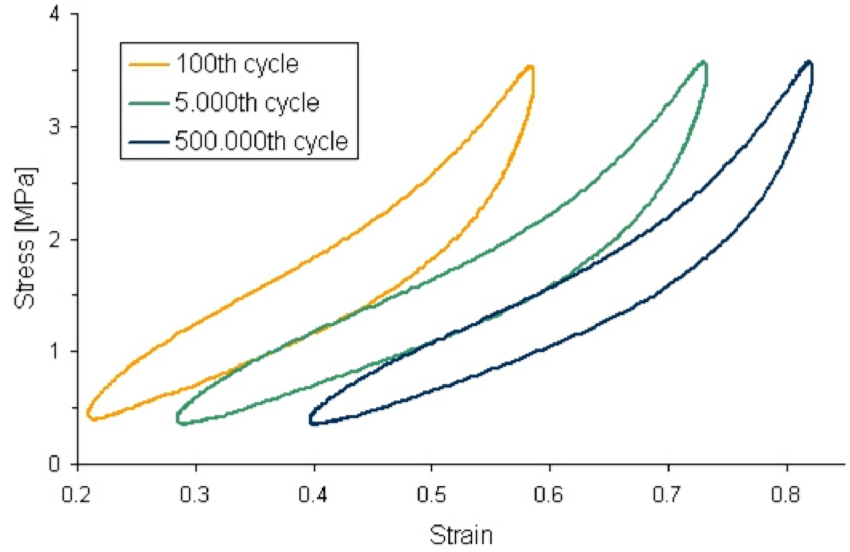

Fig. 3.15: Measured stress-strain curves of the HNBR materials at different time intervals.

The dynamic modulus ($E_{dyn}=(\sigma_{max}-\sigma_{min})/(\varepsilon_{max}-\varepsilon_{min})$) is widely used to determine the damage accumulation of the tested materials under cyclic load condition. The change of the dynamic modulus as a function of cycle number with different maximum stress is shown on figure 3.16.

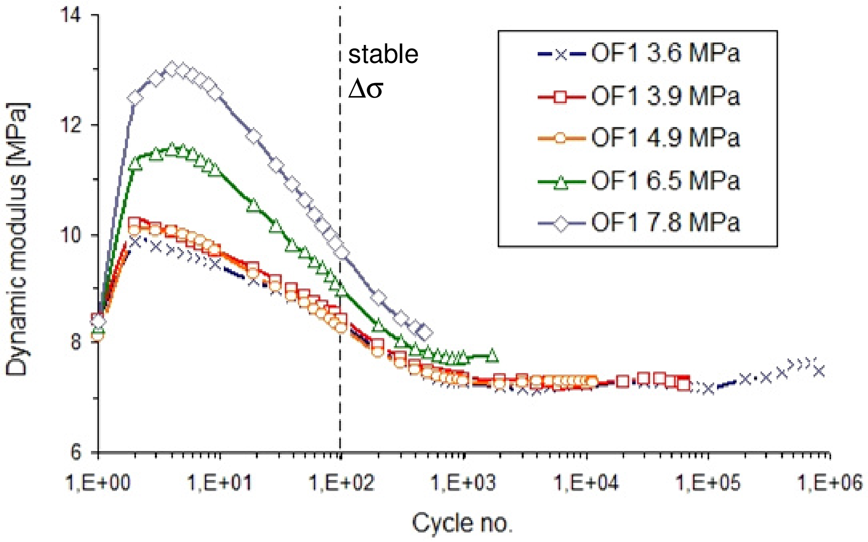

Fig. 3.16: Dynamic modulus change in function of the cycle number with HNBR materials.

For reliable data reduction cycles above 100 can be used (but because of the change in the material properties, initial values are also plotted). After the first 100 cycles, where the Mullins effect and the running in of the testing machine are dominant, a small reduction is visible and after this period it tends to a constant value. In contrary to Figure 3.13b, in Figure 3.16 there is no real crack propagation observed, because this process would cause a dramatic modulus decrease.

More details are shown in Figure 3.17, where four different measurement results are have been plotted together. In three cases there is a clear correlation between the fatigue life and the modulus value, but one specimen did not break during the testing time.

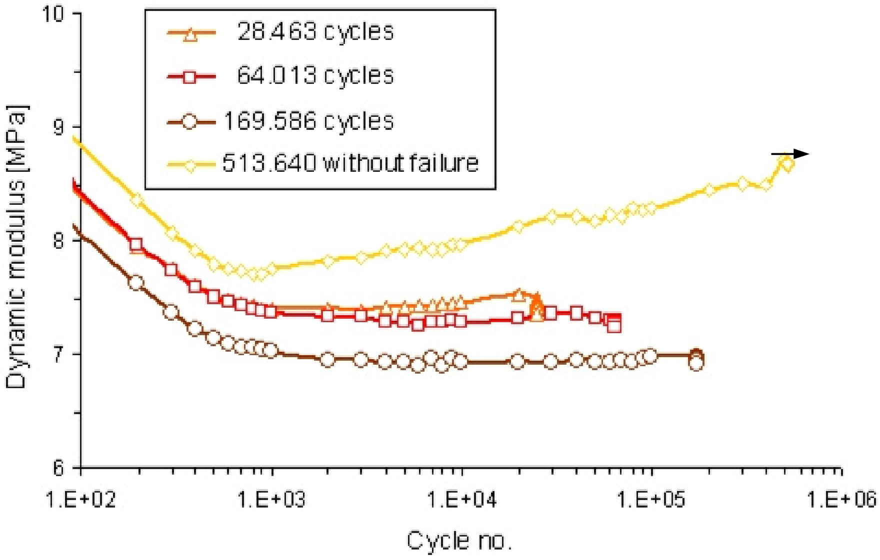

Fig. 3.17: Effect of the dynamic modulus on the fatigue life time under 3,9 MPa maximum stress.

The dynamic modulus has a constant value after 10^3 cycles. A decrease was measured only in the last cycles, during visible crack growth. This could have several reasons, and it is expected that strain crystallization might play an important role. Several studies have been done for characterizing strain crystallizing rubbers (Dick, 2001; Kim, 2003; Ito, 2003; Mars, 2004). Depending on the crystallization rate there can be a significant improvement in the fatigue life time, as the longest curve shows.

The secant modulus ($E_{sec}=\sigma_{max}/\varepsilon_{max}$) and also its change are nearly equal on all stress levels. Figure 3.18 shows how the peak of the hysteric curves on one line stay. In this case the secant modulus is not related to any fatigue damage accumulation or dependence on the applied loads.

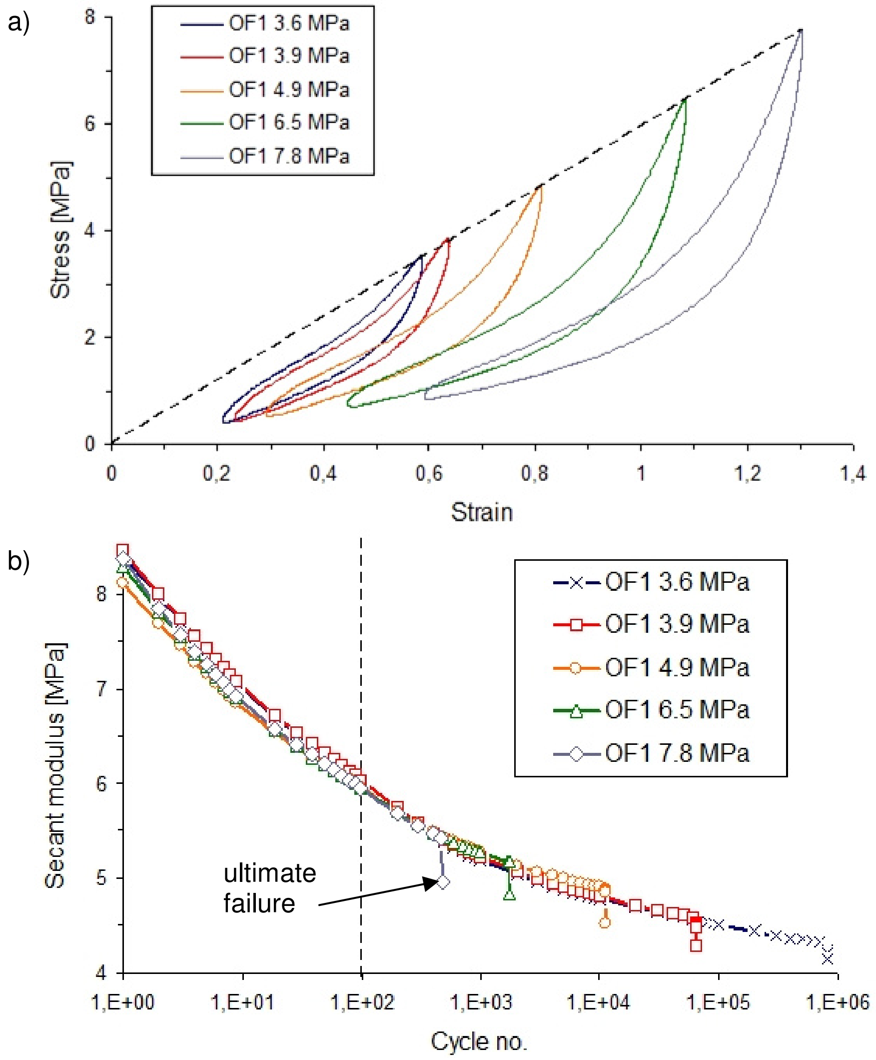

Fig. 3.18: Independence of the secant modulus on the applied stresses.

The maximum strains are shown in Figure 3.19. They are a well-known and frequently used fatigue predictor. The limit value of the maximum strain without failure is calculated by the following function:

$$\lim_{N_f \to \infty} \varepsilon_{\max}\left(N_f\right) = 0.78692 + \frac{24.6018}{\sqrt{N_f}} + \frac{-228.7004}{N_f} = 0.79 \left[\frac{mm}{mm}\right] \tag{3.15}$$

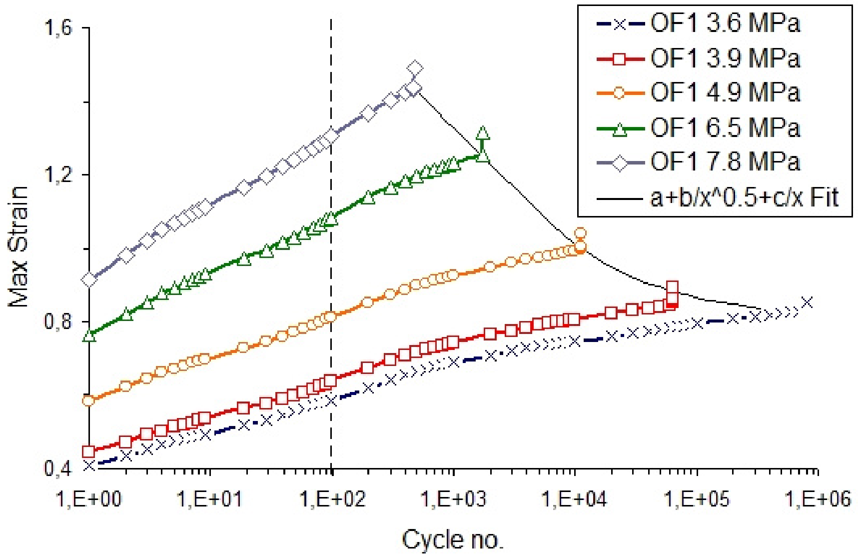

Fig. 3.19: Maximum strain change during the time.

The second frequently used approach to predict the fatigue life is the strain energy. Figure 3.20 shows the change of the strain energy density as a function of time. After the Mullins effect and the running-in period of the machine, because of the orientation of the rubber chains a slight upward trend is observed. From the ~500-1000th cycle, the values fall until final failure. With the calculated energy values, the same regularities are observed.

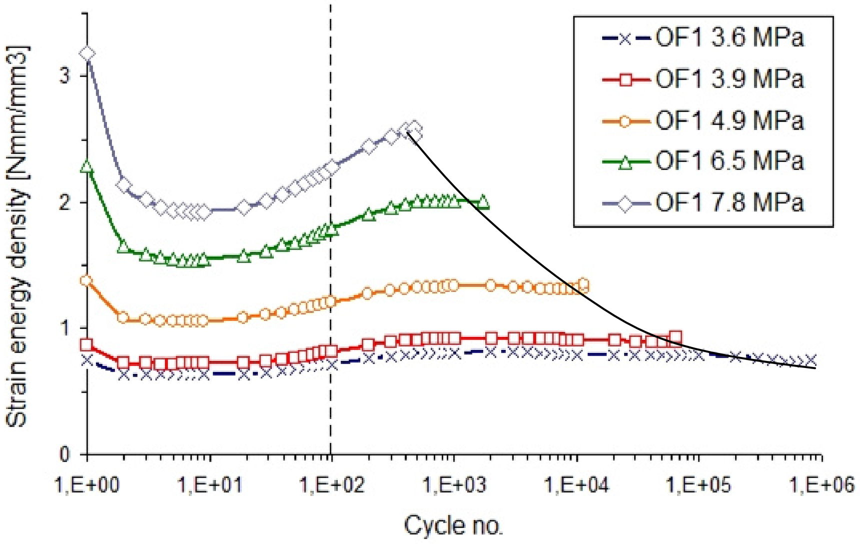

Fig. 3.20: Change of the strain energy density under different stress levels.

The relation between the fatigue life and the strain energy density of the last cycles depends on the maximum stresses but has no real threshold limit.

The dissipated (lost) energy has the same characteristic (Figure 3.21a), so the ratios of the dissipated and the total strain energy density are also shown in Figure 3.21b, which decrease with time and increase when a visible crack occurs.

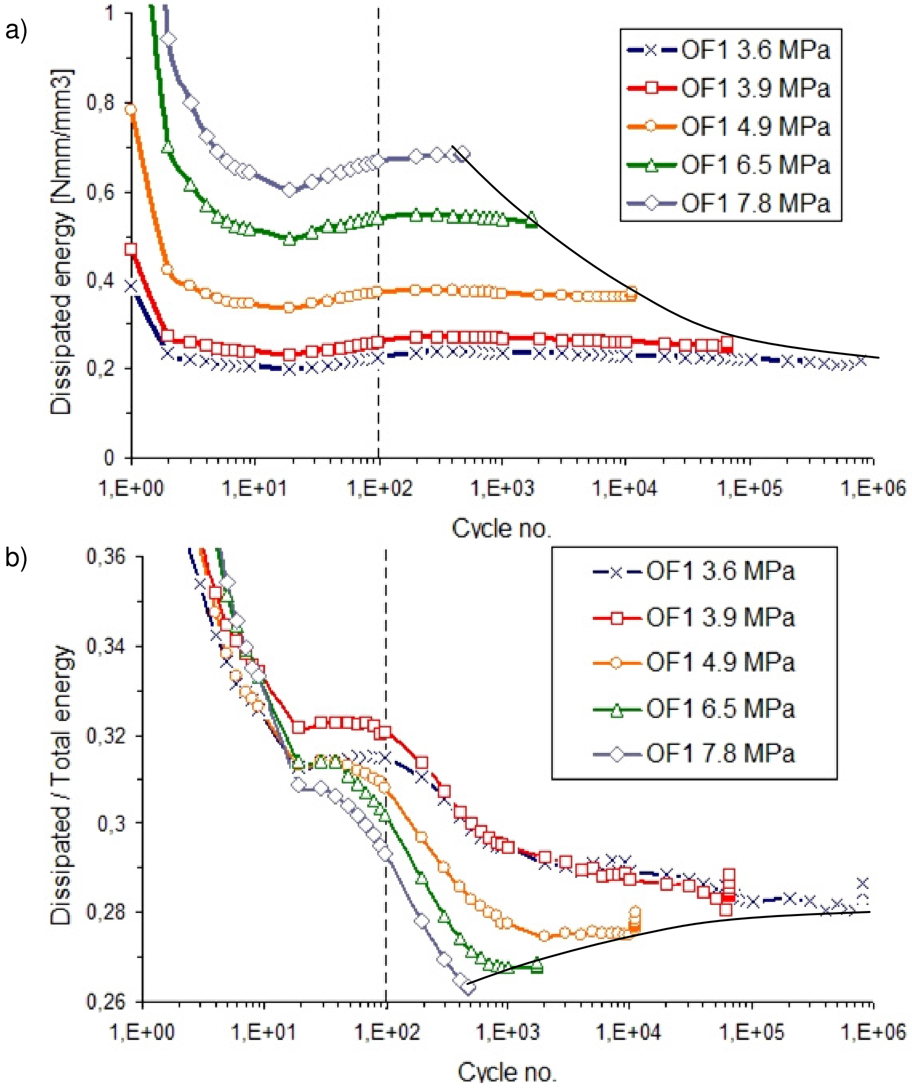

Fig. 3.21: Ratio of the lost and the total energy in the function of the cycle number.

The change of the dissipated energy can describe the energy demand of the new surface formation, but an increment of the ratio is visible only at final failure. Summarizing these findings, it must be stated here that the hysteretic analysis does not live up to the expectations for the detailed analysis of HNBR.

3.2.2.5 Analysis of the TPU results

To compare the fatigue behaviour of the two elastomeric materials, the same parameters have been calculated for the TPU measurements as previously for HNBR. The hysteresis cycles of the TPU with a nominal maximum stress 30 MPa are shown in Figure 3.22a. This hysteretic behaviour is completely different from the HNBR material, the hysteresis loops have visible time (cycle number) and stress dependences.

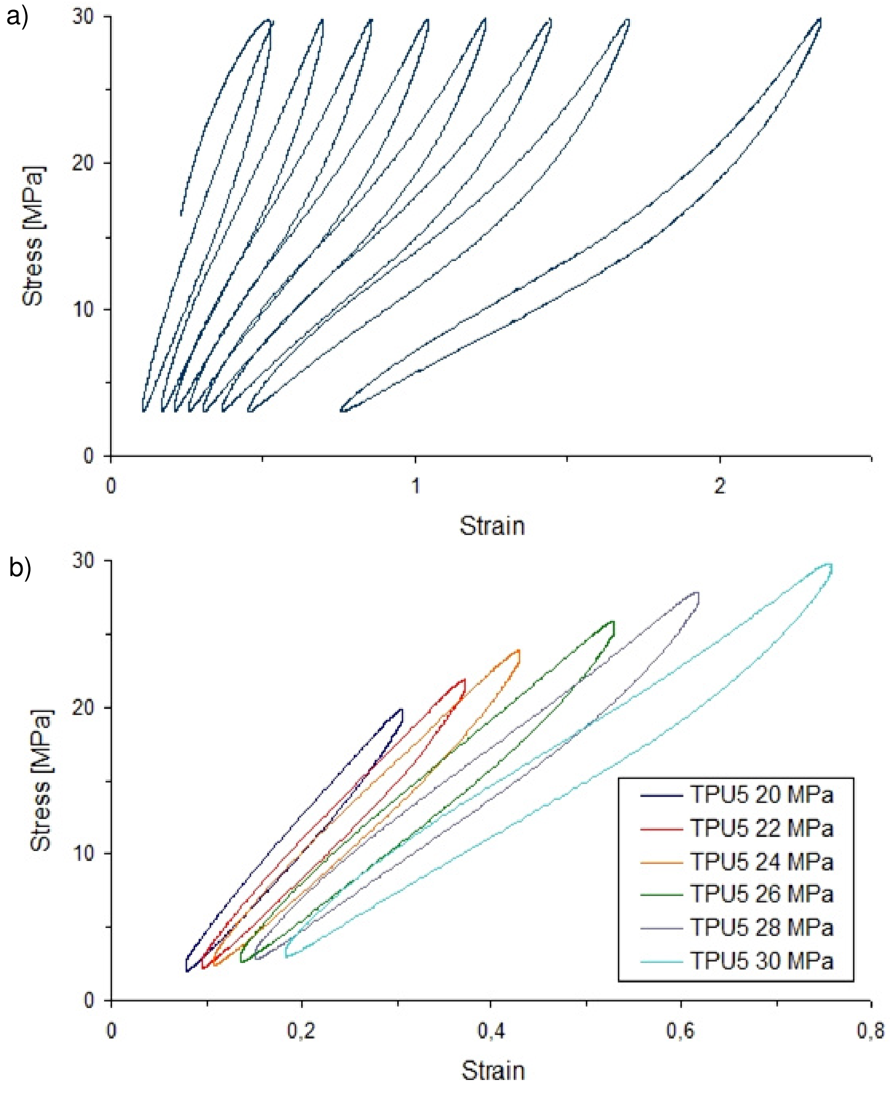

Fig. 3.22: Hysteresis curves of the TPU 5 material under cyclic loading; constant stress (a) and selected curves at various stress levels (b).

Dynamic modulus values for TPU at various stress levels from 20 MPa to 30 MPa are shown in Figure 3.23. Above 30 MPa maximum stress the TPU specimen failed after only a few cycles. The dynamic modulus reveals similar time dependence as the HNBR material above (compare Fig. 3.16). The modulus is decreases up to about 500 cycles with a higher and after 500 cycles with a lower gradient. However, in contrary to HNBR an inverse proportion between the modulus and the maximum stress is observed.

The secant modulus under different maximum stress levels over a long time is shown in Figure 3.24. As expected and similar to the tendency of the dynamic modulus values, higher loading results in a smaller secant modulus, too.

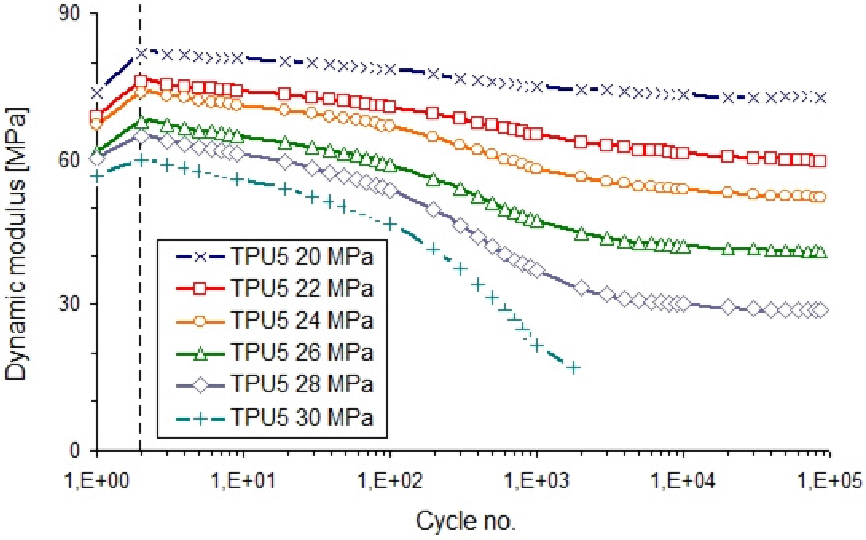

Fig. 3.23: Dynamic modulus change with different maximum stress.

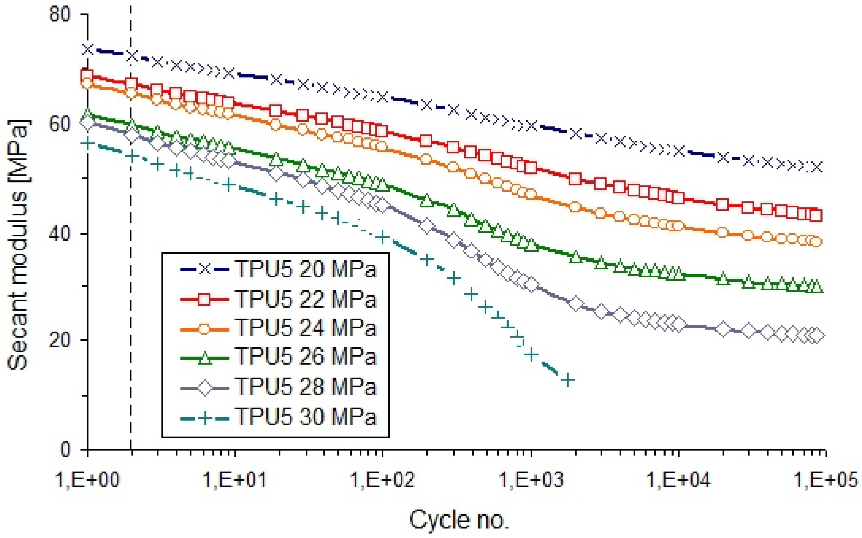

Fig. 3.24: Secant modulus change with different maximum stress.

The cycle number dependence of the total strain energy density values for various load levels is shown in Figure 3.25. The total strain energy densities at all stress levels increase continuously during the measurements. In contrast to this, a local maximum was visible for the HNBR materials after 500 cycles (compare Figure 3.20).

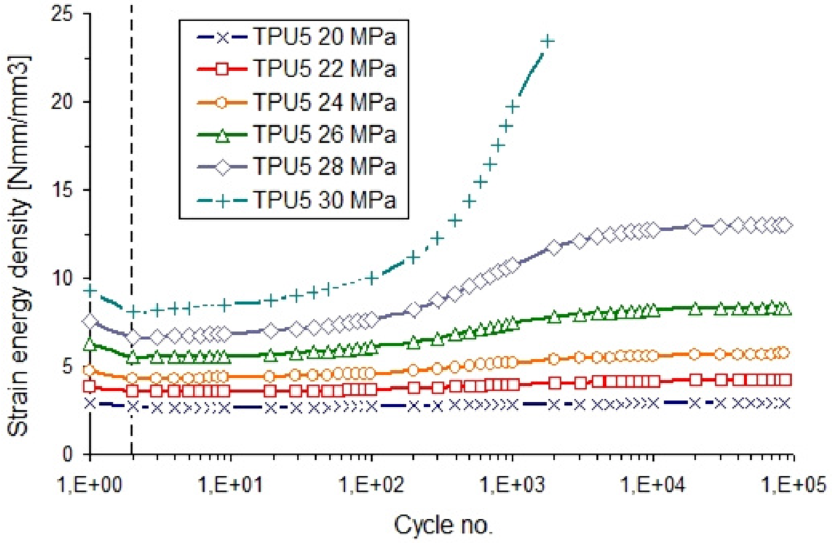

Fig. 3.25: Strain energy density of the TPU measurements.

3.2.2.6 Construction of the softening Wöhler curves

As no ultimate fracture of the TPU specimen in a reasonable cycle number range was observed, the reduction of the modulus (softening) was used as failure criterion. First, these softening-type Wöhler curves were constructed. The material softening of the TPU specimens as a function of the cycle numbers are shown on Figure 3.26, where 100% means the maximum value of the dynamic modulus (see Figure 3.23).

From the highest stress level, where failure has occurred at the 21.7% of the modulus maximum, we are able to estimate the fatigue life under different forces. The best fit of the dynamic modulus decline (E^*_i/E^*_{max}) is shown in Figure 3.27 as a function of the cycle number and the maximum stress (Zahnt, 2003).

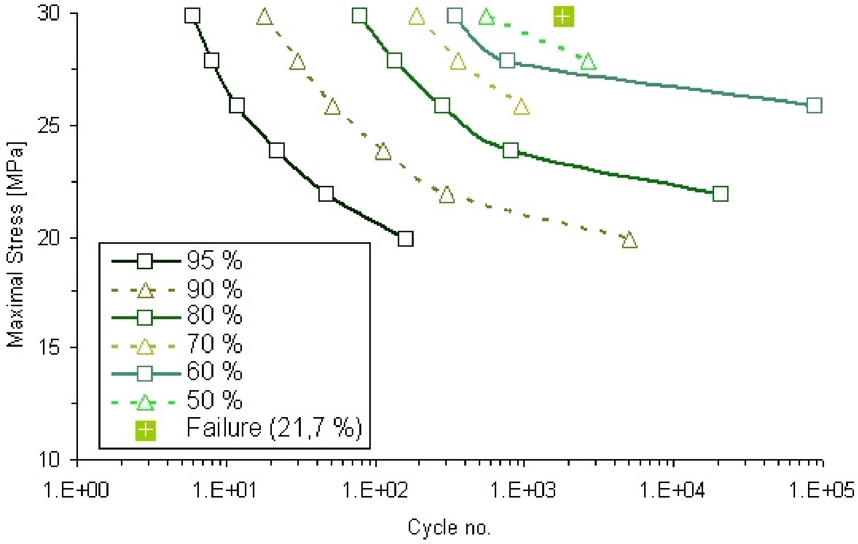

Fig. 3.26: Reduction of the dynamic modulus in percentages of the maximum value as a function of the maximum applied stress during the measurement cycles (softening Wöhler curves).

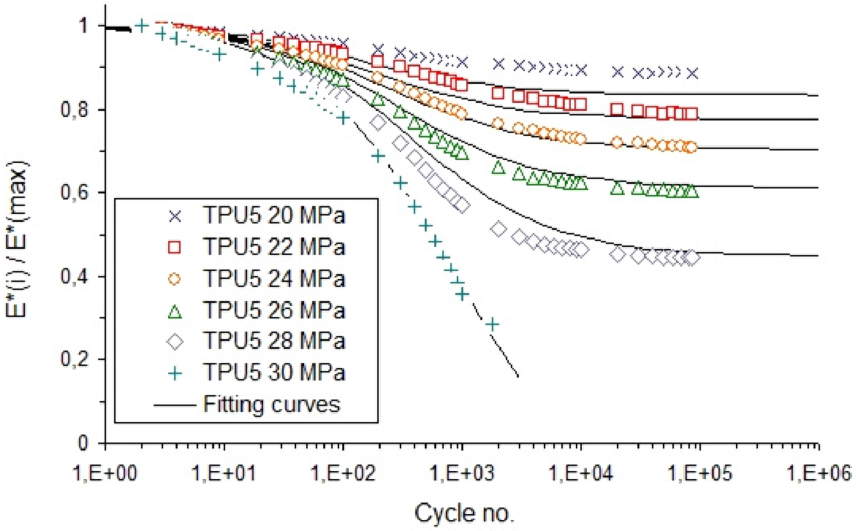

Fig. 3.27: Data points and 2D fitting curves of the dynamic modulus reduction.

Due to the asymptotic character of these curves, the following sigmoidal fitting equation is used:

$$E^*_{i/\max} = f(N_f, A, B) = A + \frac{1-A}{1+(N_f/B)^{3/4}} \tag{3.16}$$

where the A and B values depend on the maximum stress levels as follows:

$$A = f(\sigma_{\max}) = 1.012 - 2.2498 \cdot 10^{-5} \cdot \sigma_{\max}{}^{3} - 6.2166 \cdot 10^{-14} \cdot e^{\sigma_{\max}} \tag{3.17}$$

$$B = f(\sigma_{\max}) = 20.81 + 0.01528 \cdot \sigma_{\max}{}^{3} + 3.997 \cdot 10^{-11} \cdot e^{\sigma_{\max}} \tag{3.18}$$

The 3D representation of Figure 3.27 is shown in Figure 3.28.

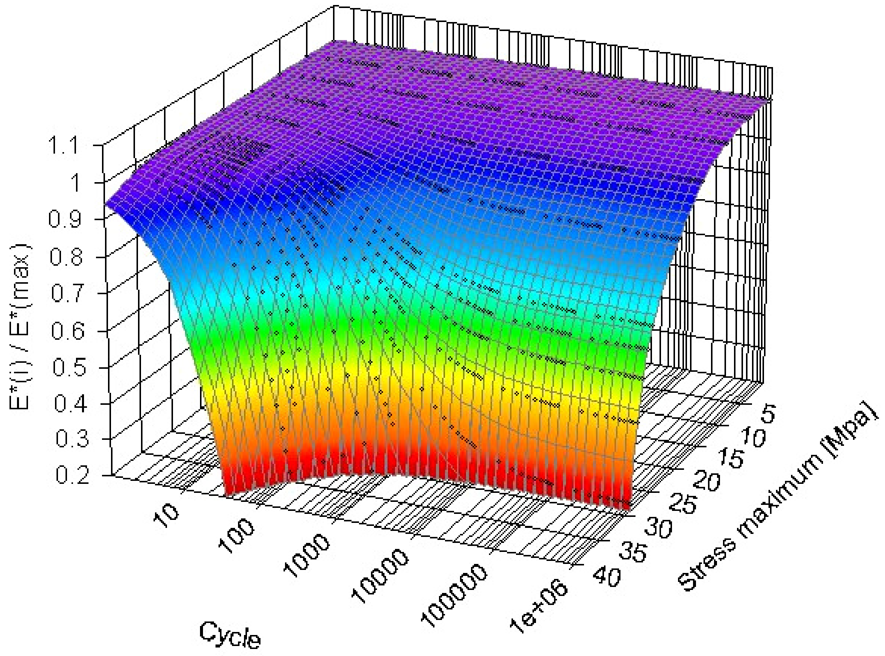

Fig. 3.28: 3D fitting curves of the dynamic modulus reduction.

To determine the limit of that maximum stress, where no failure will occur, the threshold value is read from the Figure 3.29 diagram at the point of $E^*_{(i)}/E^*_{\max}=0.25$ (see Figure 3.4):

The maximum stress level where no failure will occur was estimated for the TPU material under the above described experimental conditions:

$$\lim_{N_f \to \infty} \sigma_{\max}\left(N_f, E_i / E_{\max} = 0{,}25\right) \approx 28.95 \ [MPa] \tag{3.19}$$

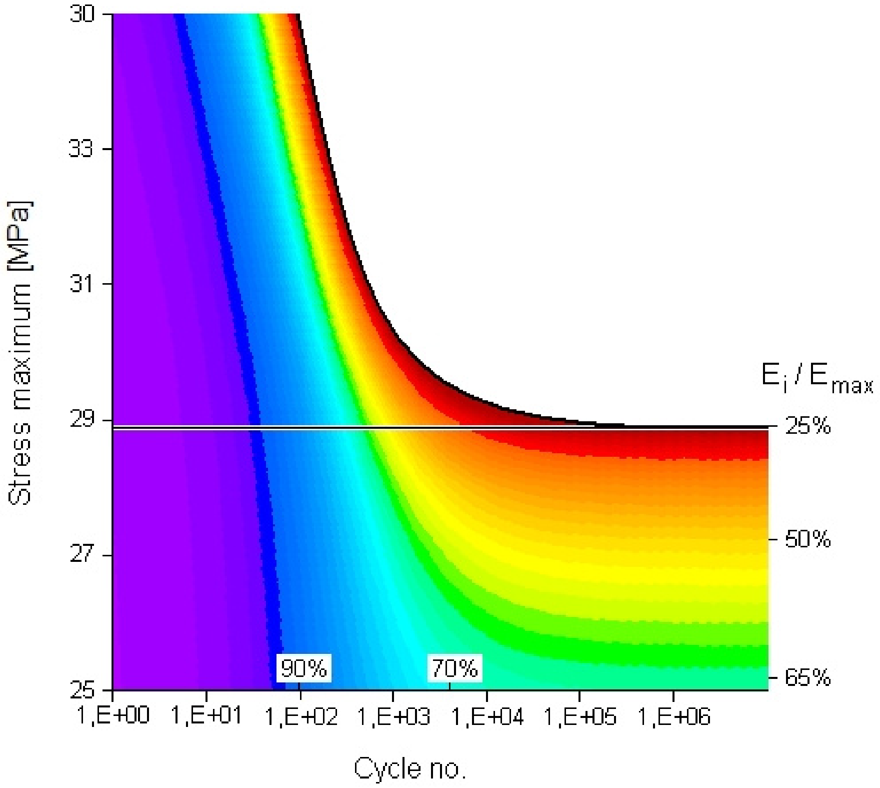

Fig. 3.29: Stress limits evaluation from the 3D fitting.

This nominal stress is interpreted as the fatigue strength of this TPU material for uniaxial test conditions and at room temperature.

3.3 Displacement controlled fatigue tests using Diabolo-type specimen

A displacement controlled uniaxial tensile test method using a novel smooth notched “Diabolo-type” specimen geometry along with an appropriate test set-up for cyclic loading was developed and local strain based Wöhler curves were constructed. The local stress and strain distribution of the “Diabolo-type” specimen was determined by using a proper viscoelastic-hyperelastic material model with adequate material parameters which were derived from preliminary experiments.

3.3.1 Experimental

A new specimen form was developed and manufactured by two different methods. The dimensions and the shape of the “Diabolo-type” specimen are shown in Figure 3.30.

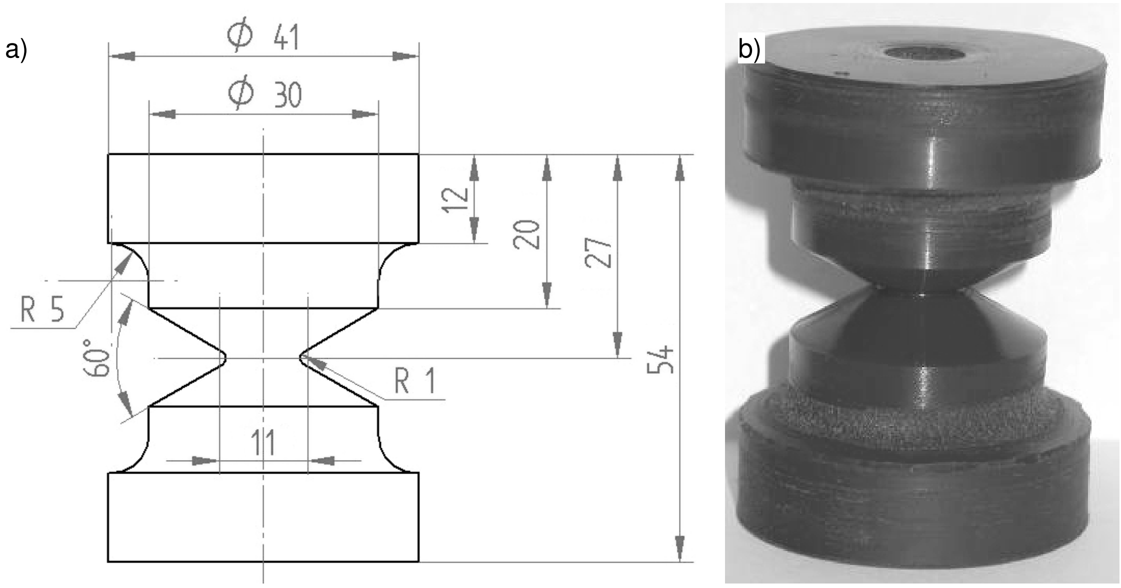

Fig. 3.30: Geometry of the diabolo specimen (a) and image of the manufactured specimen (b).

A special injection moulding tool was developed and realized by the company partner (SKF Economos Austria GmbH, Judenburg, A) and injection moulded specimens were produced. Specimens were also machined from cylindrical pieces of elastomers. While the first processing method is used for soft (low modulus) elastomers, the second is applied for stiffer (high modulus) elastomers and was used in these experiments. Special care was taken to ensure the reproducibility and accuracy of the notch region of these specimens with constant radius (R=1). Due to the smooth notch, the failure is localized in the mid section of the specimen. It was assumed that with highly concentrated stresses and strains the accuracy and reproducibility of the fatigue measurements could be improved. However, to construct local strain based Wöhler curves finite element simulations are needed and are described in the following section. Displacement controlled fatigue tests were performed on a servohydraulic testing machine (MTS 858, MTS Systems GmbH, Berlin, D) using the following test conditions:

- different displacement amplitude
    - from 2 to 7.1 mm for HNBR,
    - from 3.4 to 10.2 mm for TPU material,
- displacement ratio of R_s=0.1
- at standard climate conditions (T=23°C, 50% humidity)
- at a test frequency of 5 Hz

The test fixture with the test specimen is shown in Figure 3.31.

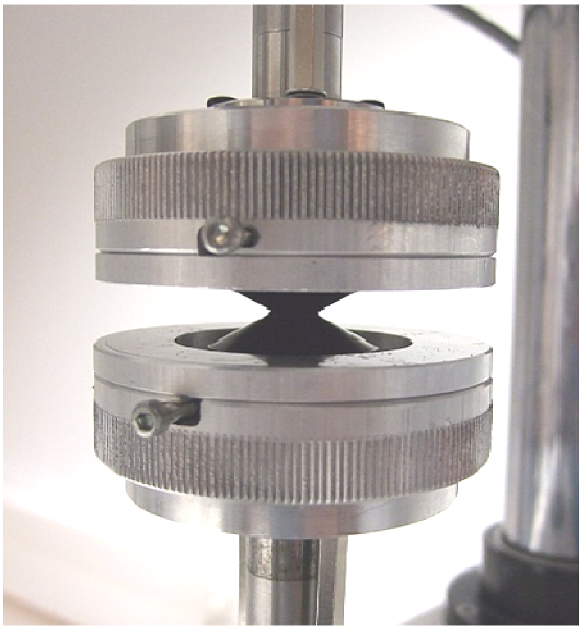

Fig. 3.31: Holder of the new specimen geometry for tensile and torsion fatigue tests.

The fixture was made from high strength aluminium alloy and allows for a fast and stable grip of both soft and stiff elastomer specimens.

During the cyclic tests the time, the peak and valley values of the reaction force are measured and recorded. The F_{max}/F_{min} curves corresponding to the lowest displacement range are shown for HNBR (2 mm) and TPU (3.4 mm) in Figure 3.32, respectively.

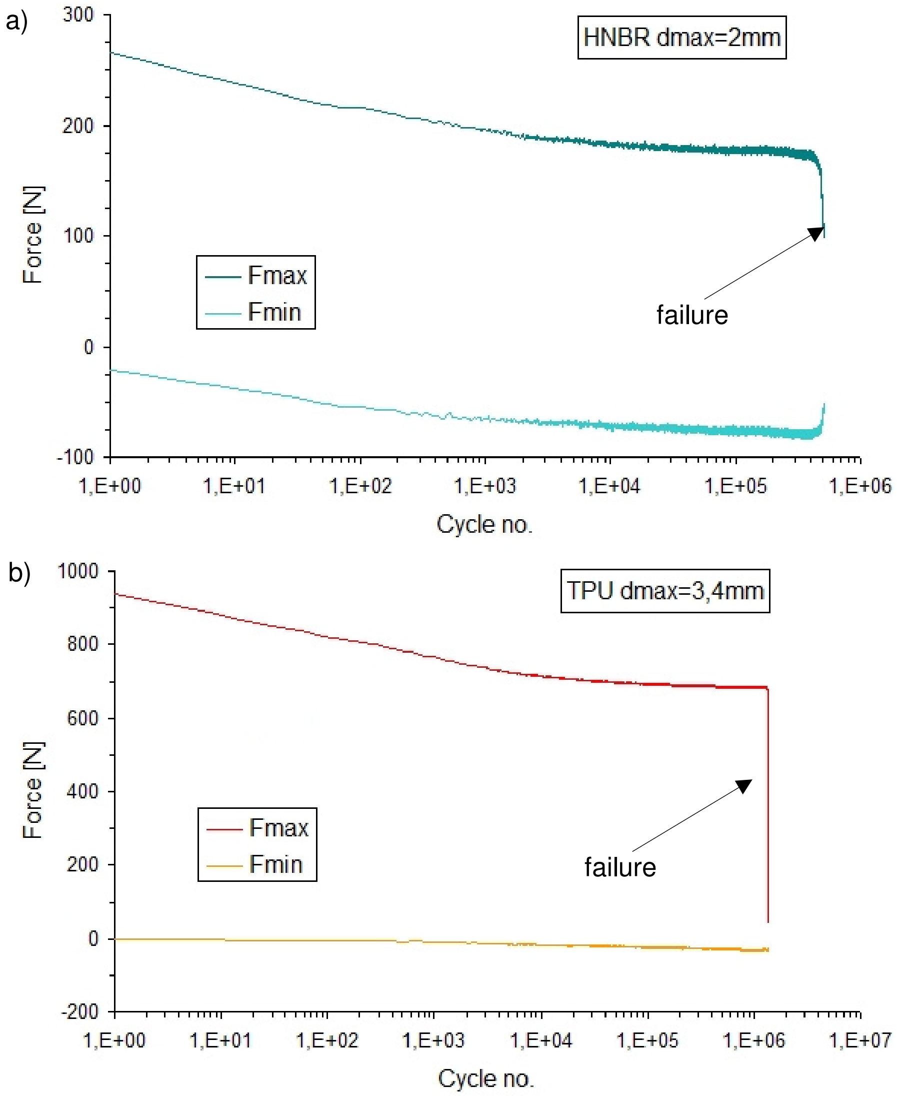

Fig. 3.32: Force during displacement controlled fatigue test of HNBR (a) and TPU (b).

The cycles-to-failure values were determined at the end of the sudden drop of the peak force values (indicated in the Figure 3.33 by the arrow). To construct local strain based Wöhler curves in terms of cycles to failure, N_f, values and local specimen strain, the global displacement must be transformed into local strain values. These local strain values were determined by finite element simulations and described in detail in the next section.

Finally, it must be noted that although the displacement ratio, R_s, was kept constant for all tests (R_s=0.1), the strain ratio varies slightly. Furthermore, comparing these experiments with the force controlled measurements, it has to be noted that positive displacement/strain ratio ($R_\varepsilon=\varepsilon_{max}/\varepsilon_{min}$) values cause negative $R_\sigma=\sigma_{max}/\sigma_{min}$ ratio values. That is, F_{min} (σ_{min}) is in the compression range during the displacement controlled experiments.

3.3.2 Finite element simulation of the Diabolo specimen geometry

A 3D finite element model was built and the illustration of one quarter of the Diabolo-type specimen with the sample holder is shown in Figure 3.33. To get the smallest element size in the highest stress region the hex-dominated meshing was optimized and the displacement was applied through a rigid body for simulating the holder of the real measurements. All specimens are stretched up to 15 mm (which corresponds to 7.5 mm in the FE simulation) and the results are analyzed in specified regions. For the contact a material specific averaged constant coefficient of friction (COF) was used.

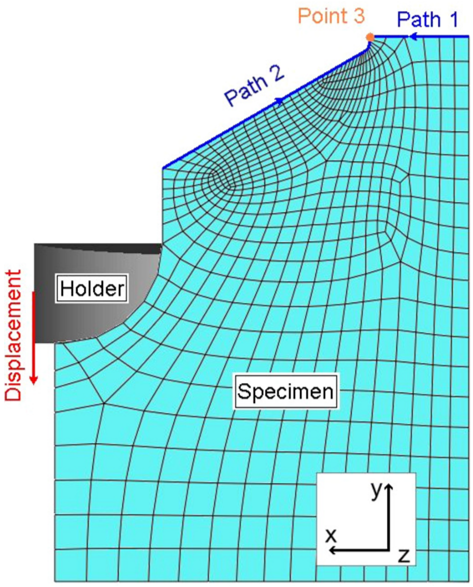

Fig. 3.33: Simulation setup.

The strain and stress distributions are investigated in two directions: one in the X direction along the specimen cross-section (Path 1), and one in Y direction (Path2) at the neck. At the node of the notch tip (Point 3) stress-strain values are determined and the corresponding diagrams are plotted.

The predicted forces (with the friction coefficients μ_{TPU}=0.55 and μ_{HNBR}=0.95) of the monotonic tensile tests are compared with the measured forces and the curves are plotted in Figure 3.34. The parameters for the hyperelastic material model used here have been determined at a testing rate of 0.01 mm/s (which corresponds to a strain rate of 0.045%/s) and the procedure along with the model parameter values are described in Section 1.3.2. To approximate the cyclic test conditions more realistically (5 Hz), the monotonic stretching of the specimen is done with 1 mm/s in these experiments.

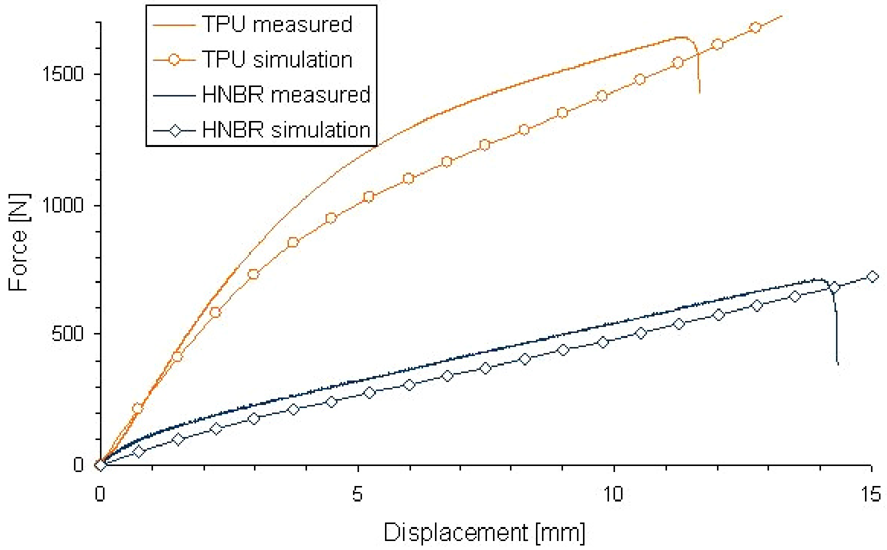

Fig. 3.34: Comparison of simulated and measured force-displacement curves.

However, rate dependent material behaviour was assumed especially for TPU. Hence, to more realistically compare the measured and predicted forces, the viscoelastic behaviour of these materials should be considered and a combined viscoelastic-hyperelastic model implemented in the FE code (Abaqus v6.7) was applied. This model is described in the next section along with the parameters necessary for the calculations.

3.3.2.1 Time dependent hyperelastic material model

In agreement with the principles of linear viscoelasticity the frequency dependence of the modulus is described without the influence of the test amplitude.

Hence, we are able to describe the time dependence of the material behaviour based on the DMA measurements (see Figure 1.17). The materials might also reveal significant strain dependencies, but both functions cannot be used simultaneously in the existing version of the simulation software (Abaqus v6.7). A new model was proposed in the literature for combining the time (frequency) and strain amplitude effects by Höfer (Höfer, 2009) but this is not yet implemented in the Abaqus code (version 6.7).

The model described below was used in this thesis for modelling the combined hyper-viscoelastic behaviour of elastomers. The viscoelastic time domains have to be defined by Prony series:

$$g_R(t) = 1 - \sum_{i=1}^{N} g_i^P \cdot (1 - e^{-t/\tau_i^G}) \tag{3.20}$$

where $g_R(t)$ is a dimensionless relaxation modulus, g_i^P and τ_i^G are material constants, and t is the time (Abaqus Analysis User's Manual v6.7).

For frequency dependent data fitting the required parameters were calculated from the DMA results as follows:

$$\omega_{real}(g^*) = \frac{G_l}{G_\infty} = \frac{E_l}{E_\infty} \tag{3.21}$$

$$\omega_{imaginary}(g^*) = 1 - \frac{G_s}{G_\infty} = 1 - \frac{E_s}{E_\infty} \tag{3.22}$$

$$\left.\begin{array}{l} \omega_{real}(k^*) \\ \omega_{imaginary}(k^*) \end{array}\right\} are \quad ignored \quad for \quad incompressible \quad materials$$

where G are shear modulus, E_l is the loss modulus, E_s is storage modulus, and E_∞ is the long-term elastic modulus. These modulus values were estimated by fitting the measured DMA curves and were taken as E_∞=36.5 for TPU and E_∞=12.45 for HNBR.

The corresponding Prony series values were calculated by the FE software and are listed in Table 3.2.

TPU			**HNBR**		
i	g_i	τ_i	i	g_i	τ_i
1	2.24E-01	6.08E+03	1	8.83E-01	5.58E-05
2	3.18E-02	2.85E+00	2	2.30E-02	7.80E-03
3	3.15E-02	3.21E+00	3	1.64E-02	6.34E-02
4	3.15E-02	3.21E+00	4	1.28E-02	5.64E-01
5	3.15E-02	3.21E+00	5	9.33E-03	7.78E+00
6	3.15E-02	3.21E+00	6	9.33E-03	7.78E+00
7	3.15E-02	3.21E+00	7		

Table 3.2: Prony series for describing the time dependent material behaviour for HNBR and TPU (Abaqus calculation).

Testing speed can be calculated in the finite element software with the “Step time” (T) option, which is the time to the maximum strain (ε_{max}), and the corresponding strain rate is:

$$\dot{\varepsilon} = \frac{\varepsilon_{\max}}{T} \tag{3.23}$$

Figure 3.35 shows the viscoelastic “long-term” and “instantaneous” responses in “Visco” mode (Abaqus term) under different strain rates (together with the hyperelastic behaviour of a uniaxial stretched unit cube, which are able to represent the material model) for a single-element test.

The differences between the long-term and the instantaneous stress-strain curves come from the stress calculation methods. The hyperelastic Ogden model defines the uniaxial stress with the following equation (Shergold 2006):

$$\sigma_0(\lambda) = \sum_{i=3}^{N} \frac{2\mu_{0i}}{\alpha_i} \cdot (\lambda^{\alpha_i - 1} - \lambda^{-1/2 \cdot \alpha_i - 1}) \tag{3.24}$$

where $\lambda=\varepsilon+1$, $\sigma_0(\lambda)$ is the principal nominal stress, μ_{0i} and α_i are the materials constants, which were determined in section 1.3.2 for N=3.

This hyperelastic material equation represents also the material stress-strain response of the viscoelastic behaviour in FE simulations, when

- T→0 and the hyperelastic model has been determined as the “instantaneous” answer ($\dot{\varepsilon} \to \infty$)
- T→∞ and the hyperelastic model has been determined as the “long-term” behaviour ($\dot{\varepsilon} \to 0$)

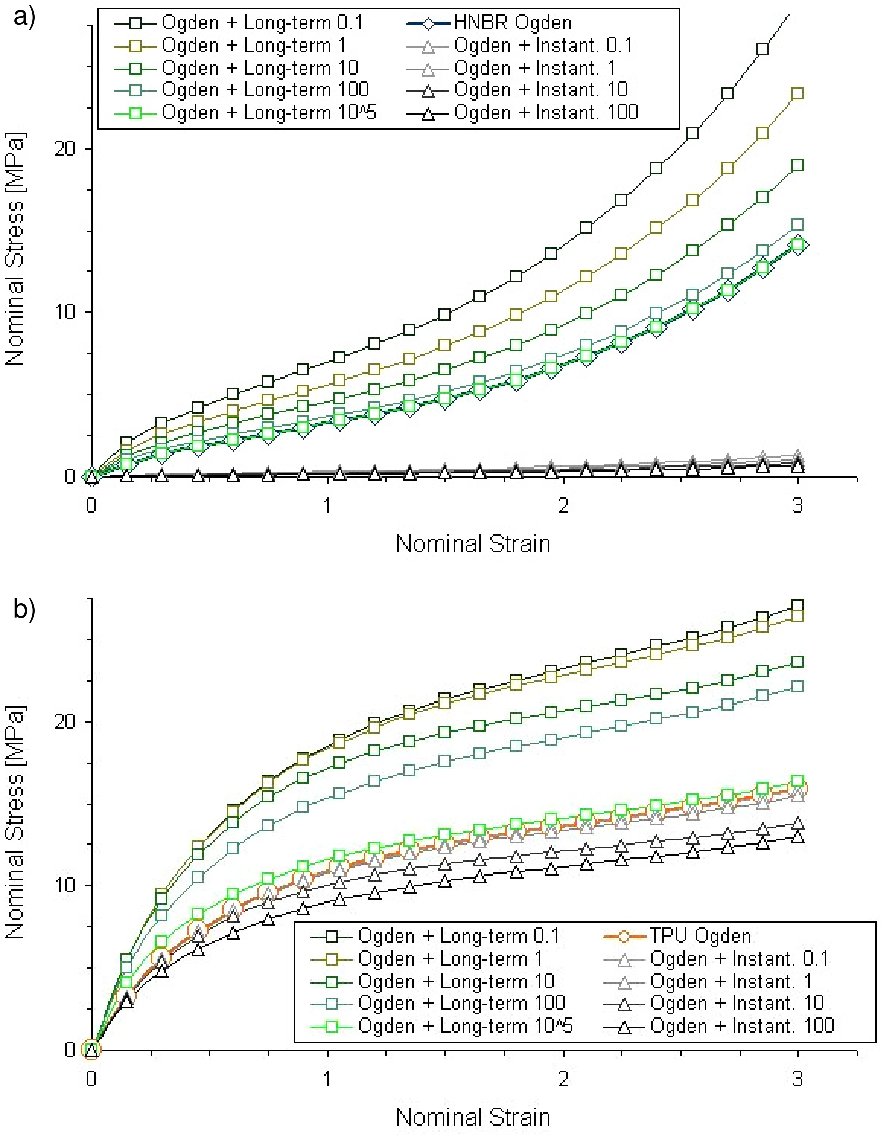

Fig. 3.35: Abaqus simulations of viscoelastic behaviour under different strain rate for HNBR (a) and TPU (b).

A model was proposed by Goh, Charalambides and Williams (Goh, 2004) for determining constitutive material constants for non-linear viscoelastic materials.

This model was used to combine large strain hyperelastic and viscoelastic behaviour in our case. The constitutive viscoelastic model consists of separable strain-dependent and time-dependent functions:

$$\sigma(\lambda,t)=\sigma_0(\lambda)\cdot g(t) \tag{3.25}$$

where g(t) is the time-dependent function.

The analytical solution of Goh (Goh, 2004) consists of the convolution integral (equation 3.26) of the stress and the finite increment method for this formula proposed by Kaliske (equation 3.30, Kaliske, 1997). The main relationships of this model are summarized below:

$$\sigma(\varepsilon,t)=\int_0^t g(t-s)\frac{d\sigma_0}{ds}ds \tag{3.26}$$

which can be split into a long-term elastic and a viscoelastic contribution:

$$\sigma(t)=g_\infty\cdot\sigma_0(t)+\sum_{k=1}^{N}\int_0^t g_k\cdot e^{-(t-s)/\tau_k}\cdot\frac{d\sigma_0(s)}{ds}ds=g_\infty\cdot\sigma_0(t)+\sum_{k=1}^{N}h_k(t) \tag{3.27}$$

where

$$h_k(t)=\int_0^t g_k\cdot\exp\left(-\frac{t-s}{\tau_k}\right)\cdot\frac{d\sigma_0(s)}{ds}ds \tag{3.28}$$

$$g_\infty=1-\sum_{k=1}^{N}g_k \tag{3.29}$$

where g_k and τ_k are shown as g_i and τ_i in Table 3.2. For the time interval (t_n, t_{n+1}), the time step Δt is given as $\Delta t=t_{n+1}-t_n$, and the exponential expression can be split into:

$$\exp\left(-\frac{t_{n+1}}{\tau_k}\right)=\exp\left(-\frac{t_n}{\tau_k}\right)\cdot\exp\left(-\frac{\Delta t}{\tau_k}\right) \tag{3.30}$$

With this method the stress term h_k at t_{n+1} can be separated into two components, one for the period $0 \le s \le t_n$ and one for $t_n \le s \le t_{n+1}$:

$$\begin{aligned}h_k(t_{n+1})&=g_k\int_0^{t_{n+1}}\exp\left(-\frac{t_{n+1}-s}{\tau_k}\right)\cdot\frac{d\sigma_0(s)}{ds}ds=\\&=\exp\left(-\frac{\Delta t}{\tau_k}\right)\cdot h_k(t_n)+g_k\int_{t_n}^{t_{n+1}}\exp\left(-\frac{t_{n+1}-s}{\tau_k}\right)\cdot\frac{d\sigma_0(s)}{ds}ds\end{aligned} \tag{3.31}$$

The differential coefficient expressed in terms of discrete time steps for instantaneous material model (T→0):

$$\frac{d\sigma_0(s)}{ds}ds = \lim_{\Delta s \to 0}\frac{\Delta\sigma_0(s)}{\Delta s} = \lim_{\Delta t \to 0}\frac{\sigma_0^{n+1} - \sigma_0^{n}}{\Delta t} \tag{3.32}$$

With equation 3.31 and 3.32, we are able to solve analytically the integral, updating the stress in equation 3.26 with $\sigma(t_{n+1})$:

$$\begin{aligned}\sigma(t_{n+1})_{Inst.} &= g_\infty \cdot \sigma_0(t_{n+1}) + \\ &+ \sum_{k=1}^{N}\left\{\exp\left(-\frac{\Delta t}{\tau_k}\right)h_k(t_n) + g_k\frac{1-\exp(-\Delta t/\tau_i)}{(\Delta t/\tau_i)}\left[\sigma_0(t_{n+1}) - \sigma_0(t_n)\right]\right\}\end{aligned} \tag{3.33}$$

Because the initial stress-state is known (σ=ε=0 and h_k=0 at t=0), the stress can be calculated at time t > 0, with the following equation:

$$\sigma(t)_{Inst.} = \sigma_0(t)\cdot\left[g_\infty + \sum_{k=1}^{N}g_k\frac{1-\exp(-t/\tau_i)}{(t/\tau_i)}\right] \tag{3.34}$$

where the time (t) can be described in the function of the stretch maximum (λ=ε+1) and “Step time” (T):

$$t = \frac{T}{(\lambda_{\max} - 1)}\cdot(\lambda - 1) \tag{3.35}$$

To summarize the above derivation of the viscoelastic stress-strain-time dependences in uniaxial tension, here are the initial equations (original Ogden model) again:

$$\sigma_0(\lambda) = \sum_{i=3}^{N}\frac{2\mu_{0i}}{\alpha_i}\cdot(\lambda^{\alpha_i - 1} - \lambda^{-1/2\cdot\alpha_i - 1}) \tag{3.36}$$

, where λ=ε+1, $\sigma_0(\lambda)$ is the principal nominal stress, μ_{0i} is the shear modulus and α_i are the dimensionless parameters of the Ogden hyperelastic model, and the modified Ogden model is defined as follows:

$$\sigma(\lambda,t) = \sigma_0(\lambda)\cdot g(t) \tag{3.37}$$

Where σ(λ, t) is the time dependent principal normal stress. From the determined instantaneous stress (equation 3.34), the time dependent parameters are for t ≠ 0:

$$g(t)_{Inst.} = \left[g_\infty + \sum_{k=1}^{N} g_k \frac{1-\exp(-t/\tau_i)}{(t/\tau_i)} \right] \tag{3.38}$$

$$g(t)_{Long-term} = \frac{1}{g_\infty} \cdot g(t)_{Inst.} \tag{3.39}$$

The functions of the equations 3.38 and 3.39 on the hyperelastic Ogden material model are shown on Figure 3.36 compared with the viscoelastic-hyperelastic model with the effect of the strain-rate (and time step).

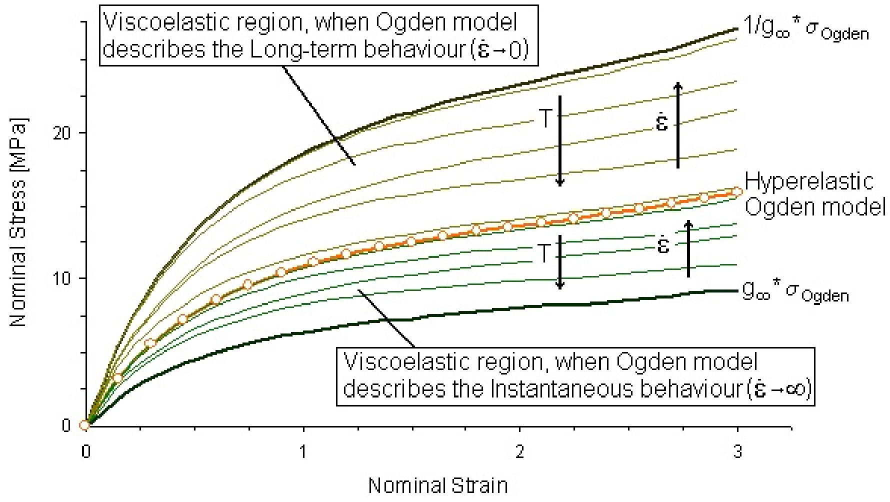

Fig. 3.36: Stress limit curves of the viscoelastic TPU material model.

As previously stated, this hyperelastic material equation represents also the material strain-stress response of the viscoelastic behaviour in FE simulations, when

- T→0 and the hyperelastic model has been determined as the "Instantaneous" answer ($\dot{\varepsilon}\to\infty$, and $g(t)_{Inst.}=1$, $\sigma(\lambda,t)=\sigma_0(\lambda)$)
- T→∞ and the hyperelastic model has been determined as the "Long-term" behaviour ($\dot{\varepsilon}\to0$, and $g(t)_{Long-term}=1$, $\sigma(\lambda,t)=\sigma_0(\lambda)$)

To verify the calculated time and strain dependent stress data by the equations 3.24, 3.25, 4.38 and 4.39 with the results of the finite element simulation the normalized root mean squared errors (NRMSE) have been determined under different “Step times” (T) for the maximum strain ε=3:

$$NRMSE = \frac{RMSE}{\sigma_{\max}^{Abaqus} - \sigma_{\min}^{Abaqus}} = \frac{\sqrt{\dfrac{\sum_{i=1}^{N}\left(\sigma_i^{calculated} - \sigma_i^{Abaqus}\right)^2}{N}}}{\sigma_{\max}^{Abaqus} - \sigma_{\min}^{Abaqus}} \qquad (3.40)$$

where $\sigma_{\max}^{Abaqus} = \sigma(T, \varepsilon = 0.115)$, and $\sigma_{\max}^{Abaqus} = \sigma(T, \varepsilon = 3)$.

The results are shown in Table 3.3.

NRD [MPa/MPa]					
TPU			HNBR		
T	Instantaneous	Long-term	T	Instantaneous	Long-term
10^{-1}	7.098E-05	8.021E-05	10^{-1}	3.187E-02	3.235E-02
10^{0}	5.714E-04	5.794E-04	10^{0}	2.736E-02	2.783E-02
10^{1}	2.798E-03	2.805E-03	10^{1}	2.949E-02	2.996E-02
10^{2}	1.323E-03	1.327E-03	10^{2}	2.114E-02	2.163E-02
10^{5}	-	3.450E-03	10^{5}	-	2.734E-05

Table 3.3: Normalized squared error between the calculated and the simulated stress values.

The parameters for the hyperelastic material model were determined at 0.045 % strain per seconds (corresponds to 0.01 mm/s) in section 1.3.2. The monotonic experiments using the Diabolo-type specimens were carried out at higher loading rates. Hence, the material model was corrected applying the method which was described above.

The following equation was used to define the new, time dependent Ogden model:

$$\sigma_0(\lambda) = \sigma_1(\lambda) \cdot g\ (t, \dot{\varepsilon} = 4.5 \cdot 10^{-4}) \qquad (3.41)$$

where $\sigma_1(\lambda)$ is the time independent response of the new hyperelastic model, and g $(t, \dot{\varepsilon} = 4.5 \cdot 10^{-4})$ is the time dependent factor at the given strain rate.

Thus the long-term stress of the new model is:

$$\sigma_1(\lambda) = \frac{\sigma_0(\lambda)}{g\ \ (t, T(\varepsilon = 1) = 2200s)} \qquad (3.42)$$

Calculated nominal stress-strain curves are shown in Figure 3.37 for HNBR and for TPU. The original Ogden model considers time independent behaviour, but also represents the situation at zero strain rates as it is shown in Eq. 3.25. The modified Ogden model is necessary to create a basic equation, and the modified model with additional viscoelastic parameters reflects the time/rate dependent behaviour.

So, the degree of the change of the fitted new (called modified) Ogden model parameters depends on the parameters of the material specific Prony series. So, the modification for HNBR is nearly invisible in this strain scale in Figure 3.37a.

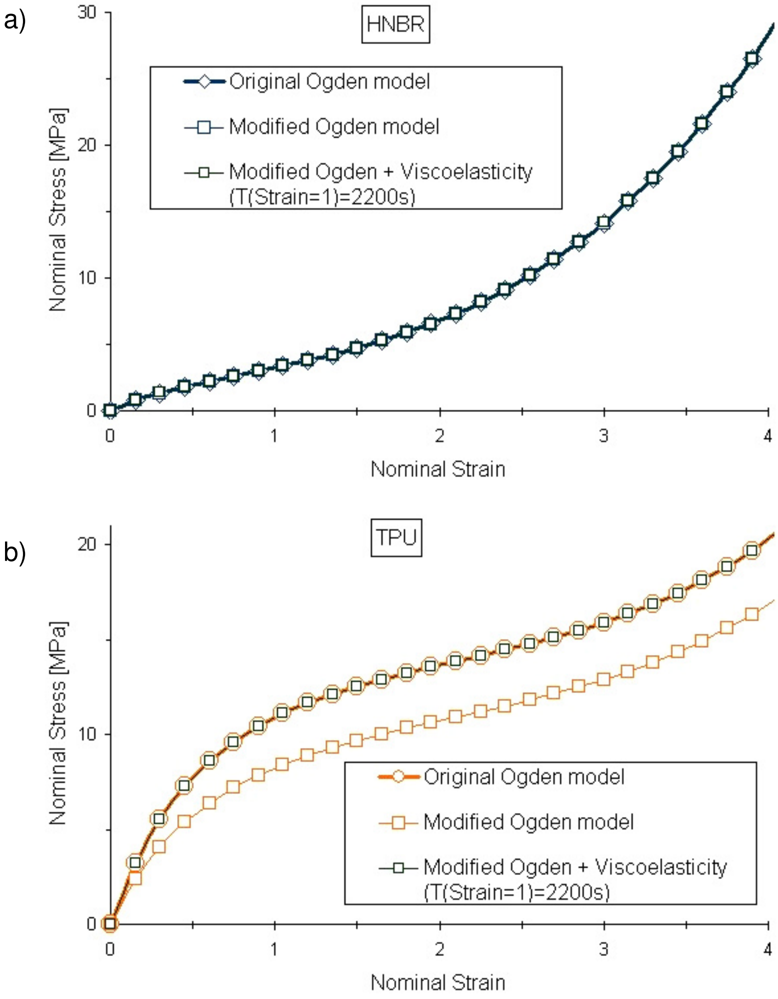

Fig. 3.37: Uniaxial stress-strain response of the modified Ogden models.

The modified Ogden model parameters for the two elastomers are listed in Table 3.4 and were used with the Prony coefficients (Table 3.2) for modelling the time dependent hyperelastic-viscoelastic material behaviour.

TPU_{mod}			**$HNBR_{mod}$**		
i	μ_i	α_i	i	μ_i	α_i
1	6.316	1.064	1	1.784	1.192
2	0.002	6.449	2	0.131	4.790
3	-0.106	-1.430	3	0.09	-2.854

Table 3.4: Material parameters of the Ogden three order hyperelastic model.

For comparison, the parameters for the original time independent Ogden model are listed in section 1.3.2 in Table 1.2.

3.3.2.2 Simulation comparison, stress and strain distributions

With the new model we can set the 1 mm/s testing speed in the finite element simulation and the measured and the calculated displacement-force curves are plotted in Figure 3.38.

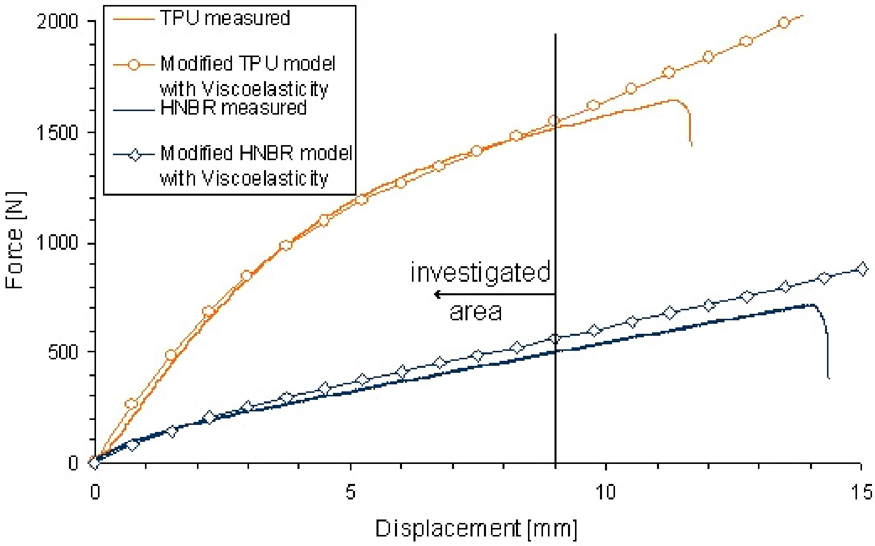

Fig. 3.38: Comparison of the measured and calculated force-displacement curves using the combined hyperelastic and viscoelastic model developed.

As the results show, with this model we were able to simulate the force-displacement response for both materials up to 9 mm displacement within ±10% accuracy. The differences between the simulations and the measured values come from two sources:

- the hyperelastic model of TPU can not describe the material damages under large strain,
- the response error of the HNBR simulated force comes from the somewhat in accurate Prony series.

The dominant volume of the specimen lies in the linear elastic range during the stretching. Furthermore, due to the localization of the stresses in the mid-section of the specimen, large strain hyperelastic behaviour of the elastomers can only be recognized in the mid section. The von Mises stress reveals a high concentration at the neck root as shown for both materials in Figure 3.39.

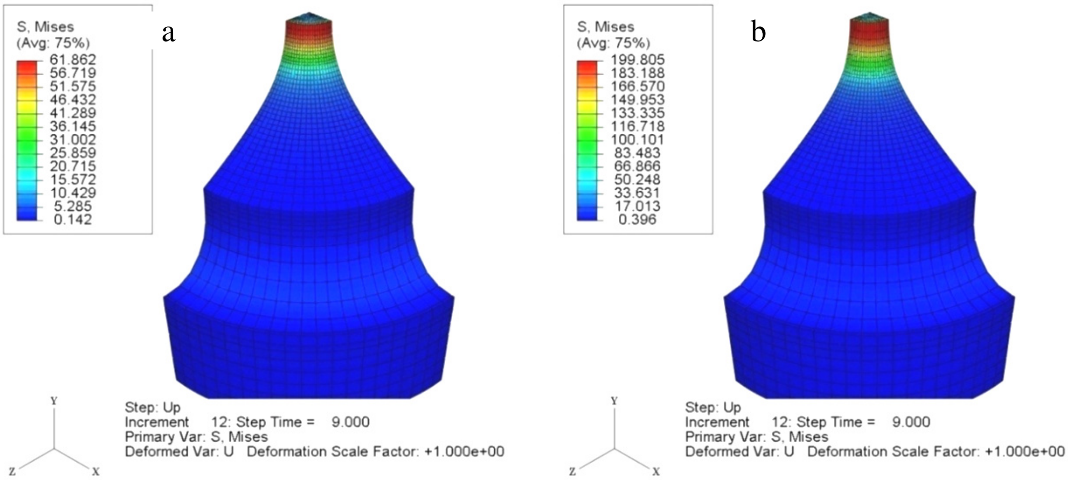

Fig. 3.39: Stress concentration of the HNBR (a) and TPU (b) materials.

Furthermore, in the Abaqus software the true stresses and the true strains were calculated. The principal maximum values of these parameters up to 9 mm stretching are shown at the P3 point in Fig 3.40a.

In general the stress-strain relationship at P3 highly depends on the material behaviour and the specimen geometry. The two hyperelastic models have relevant differences in the strain and stress values also, depending on the behaviour of the specimen parts with larger diameter. The stiffer TPU has more strain (and stress) concentration than the HNBR material with a smaller modulus in the neck.

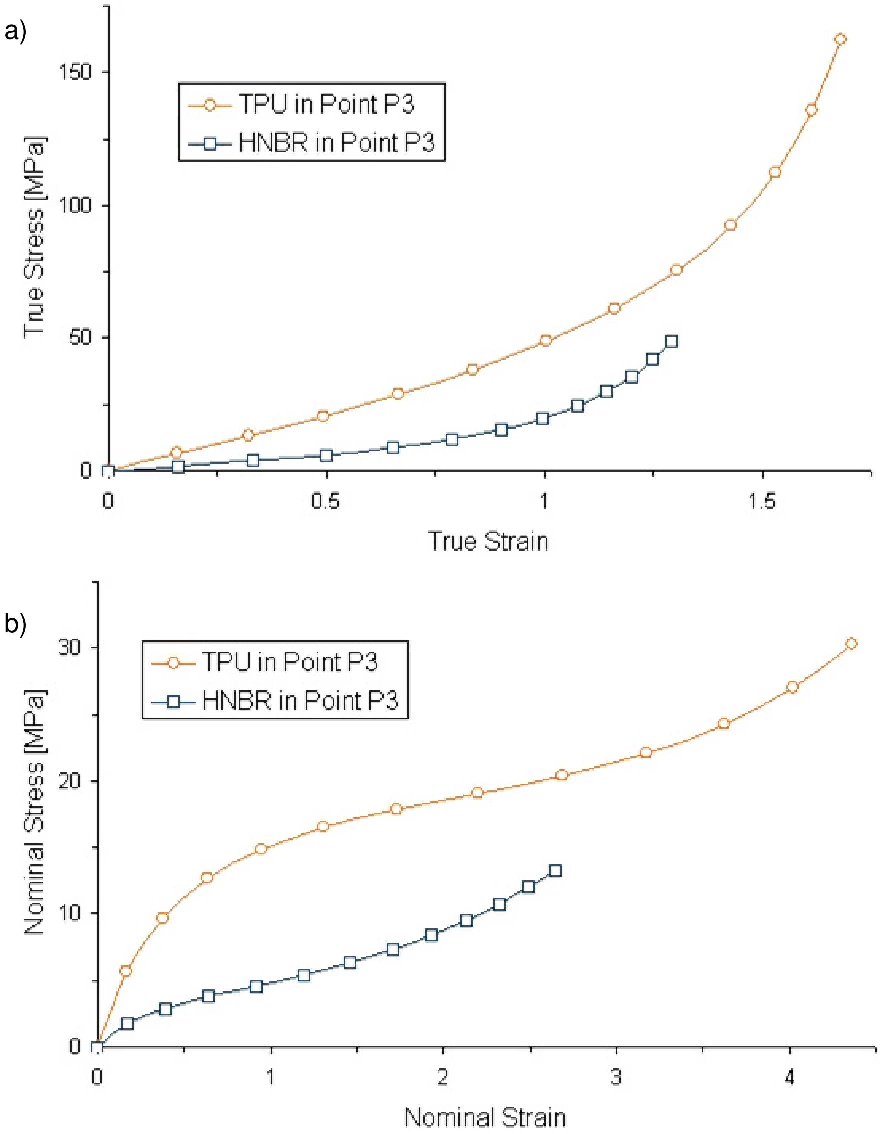

Fig. 3.40: Maximum true stress-strain (a) and nominal (b) stress-strain curves in Point 3.

To get a better comparison between the two materials and to characterize the strain localization process more precisely with non-linear hyperelastic behaviour, these values were converted into nominal stress-normal strain diagrams and are shown in Figure 3.40b. Due to the high strain localization in the materials, the true stress values or the local values of the nominal stresses can not be calculated from the measured values.

The spatial distribution of the nominal strains and stresses on the specimen surfaces at various displacement values are visible in Figures 3.41 and 3.42 on Path 2 (in Y direction). Due to the highly non-linear hyperelastic behaviour and due to the smooth notched specimen geometry, the strains and stresses don’t have an easily definable relationship. The strain concentration is observed not only in the stretching direction, but also in the specimen also observable, as it is shown through Path1 in Figure 3.43.

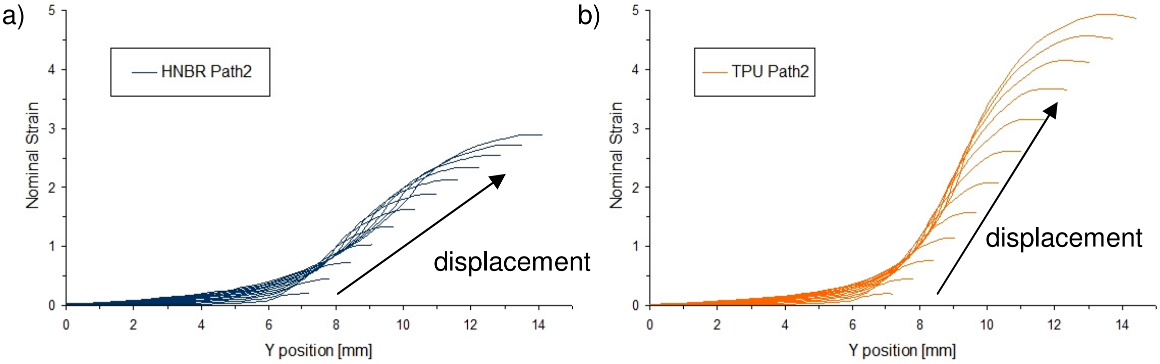

Fig. 3.41: Nominal strains through Path2 (on the surface) in the function of the Y direction.

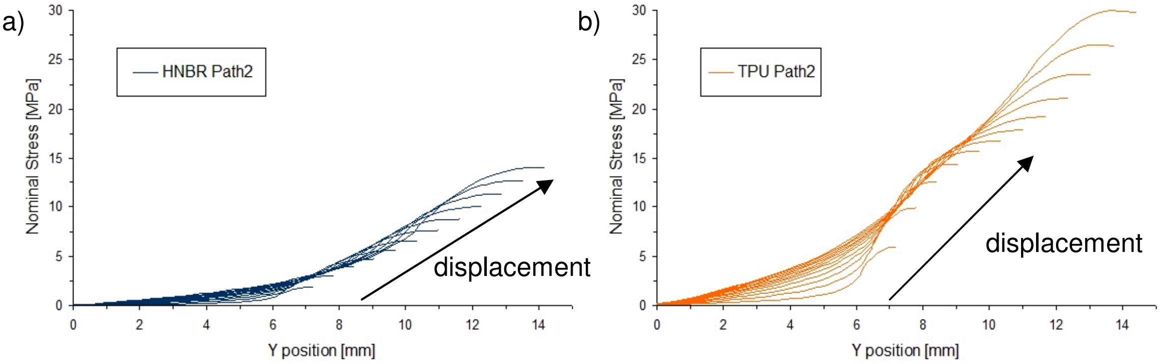

Fig. 3.42: Nominal stresses through Path2 (on the surface) in the function of the Y direction.

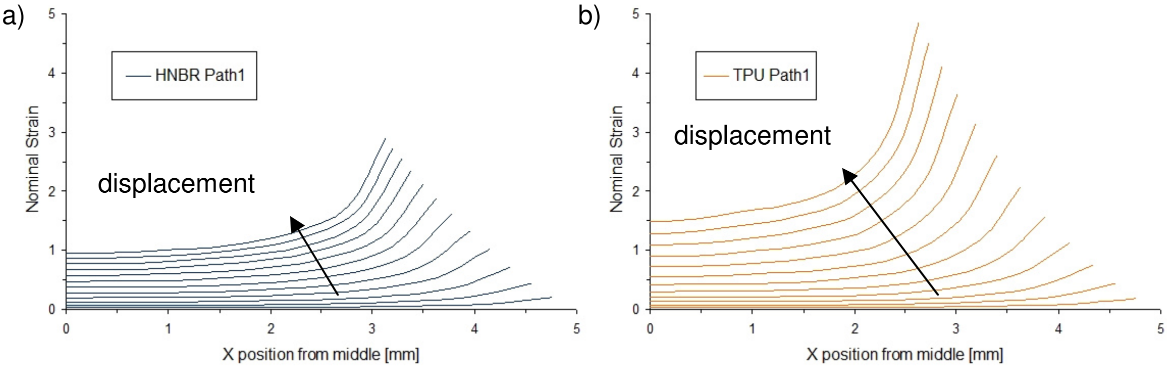

Fig. 3.43: Nominal strains through Path1 in the function of the X direction (radius).

The stress distributions shows also huge concentrations on the specimen surface compared with the axis in the middle (Figure 3.44). Furthermore, the relationship between the global displacement applied during the monotonic loading and the local strain in Point 3 was established and plotted in Figure 3.45. The calibration curve plotted in Figure 3.45a can be used for constructing local strain-based Wöhler curves. Additionally, corresponding stress values are shown for both materials in Figure 3.45b.

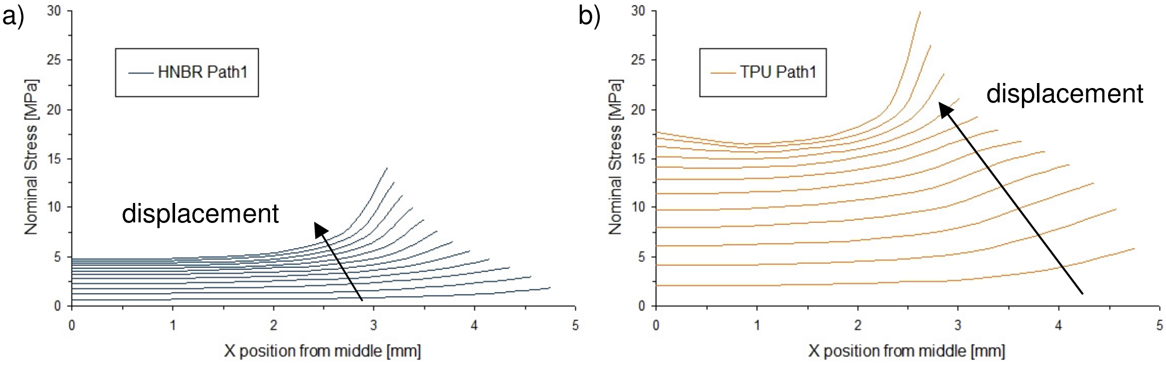

Fig. 3.44: Nominal stresses through Path1 in the function of the X direction (radius).

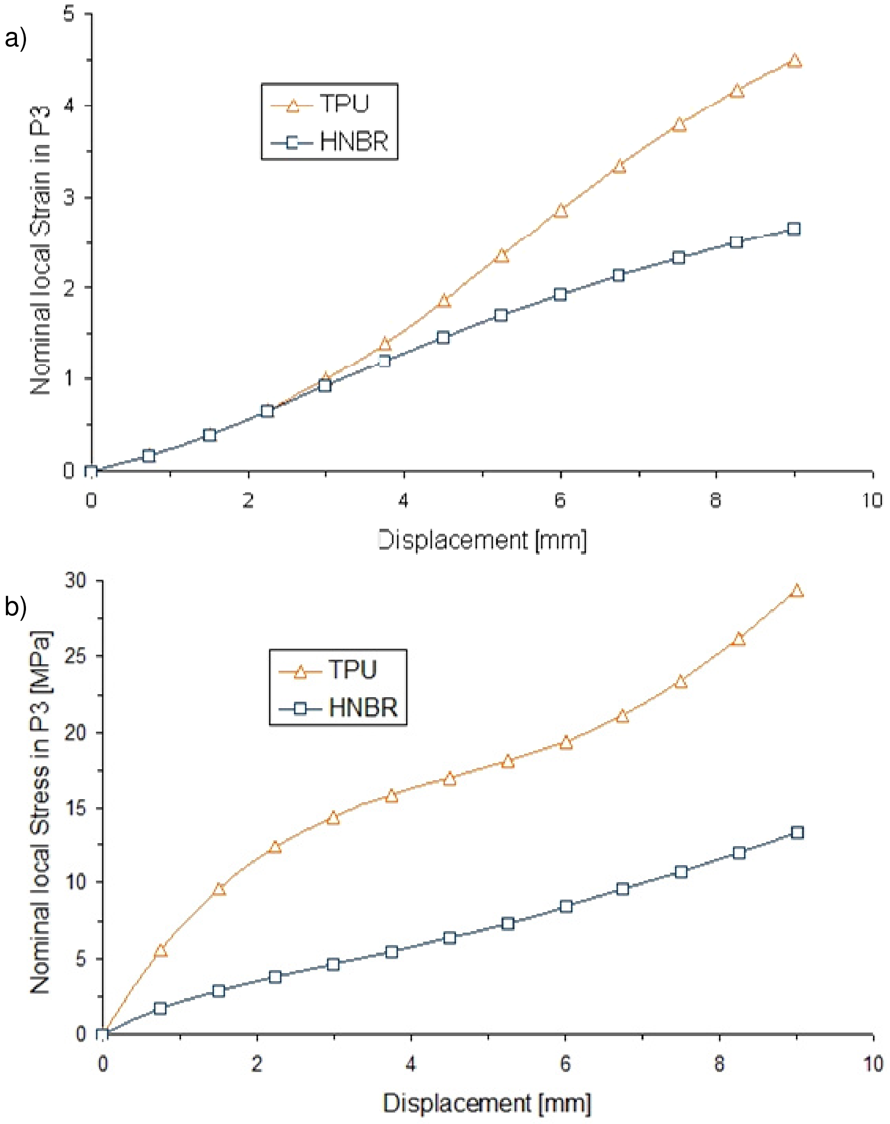

Fig. 3.45: Nominal strains (a) and stresses (b) at different displacement points in P3.

Summarizing the results of this section, it can be stated that the finite element simulations yield accurate strain values in the process zone. These values will be used in the next section for the data reduction of the displacement controlled fatigue test.

3.3.3 Displacement controlled fatigue results

Light microscope images of the fractured specimen surfaces for both materials are shown in Figure 3.46.

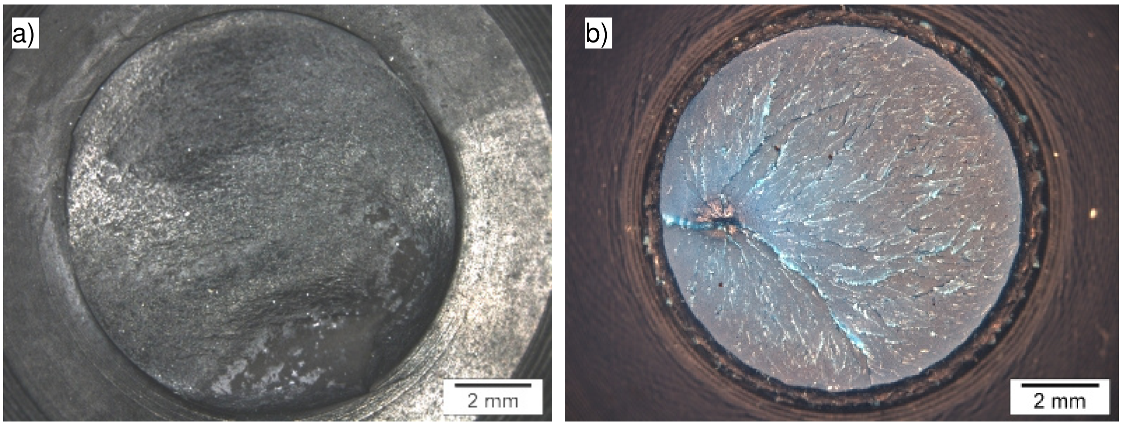

Fig. 3.46: Fracture surface images of the failed specimens for HNBR (a) and for TPU (b).

The effect of the displacement maximum on the fatigue life determined is shown in Figure 3.47, where the points represent the final specimen failure of the materials investigated (global displacement based Wöhler curves).

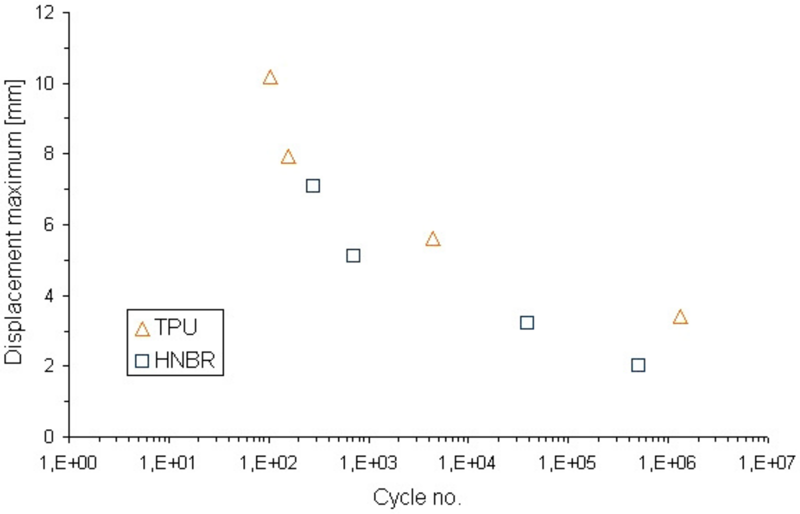

Fig. 3.47: Maximum displacement based Wöhler curves for both materials investigated.

3.3.4 Construction of local strain based Wöhler curves

A non-uniform, highly localized stress-strain distribution was observed in the Diabolo-type specimens developed and this makes the conduction of the fatigue tests easier. In addition problems encountered by the conventional fatigue tests were also eliminated:

- uniaxial elastomer specimens reveal large strains – complicated tuning,
- due to local fretting-like effects, the fixture highly influences the fatigue life,
- the distribution of the imperfections is localized in a smaller volume.

However, to accurately calculate local strain values finite element simulations are necessary. As it was previously shown in Figure 3.45, no linear relationship between the global displacement and the local strain was observed. The schematic presentation of the method developed is shown in Figure 3.48.

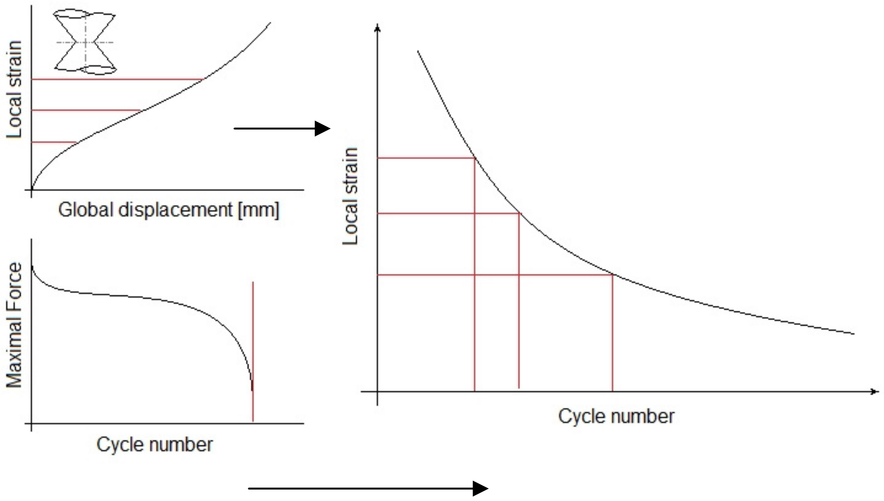

Fig. 3.48: Evaluation of the local strain based Wöhler curve.

The method consists of two parts:

- Maximum and minimum force values, F_{max}/F_{min} are continuously measured and recorded during the displacement controlled cyclic tests. The cycle number-to-failure values, N_f are determined at the final rupture of the specimen as indicated by the sudden drop of the force signal. It must be noted here, however, that determination of fatigue life is possible at different limits of the measured force values. These points can represent the various stages of the failure process, from the onset of damage up to the final rupture. The identification of these points can be done based on the change of the slope of the F_{max}-N_f curves or based on additional (i.e., optical, thermal) observations. For simplicity, in this study final failure was taken for the fatigue life time.

- With the help of the finite element simulation, the displacement axis of the conventional Wöhler curve is replaced by the calculated local strain. Due to the localized nature of the failure process, this local strain is more relevant for dimensioning of components.

To improve the accuracy of the local strain values and to determine time dependent stress-strain curves, simulations were performed using the hyperelastic-viscoelastic model. The corresponding stress-strain curves in point P3 for 5 Hz are shown in Fig 3.49.

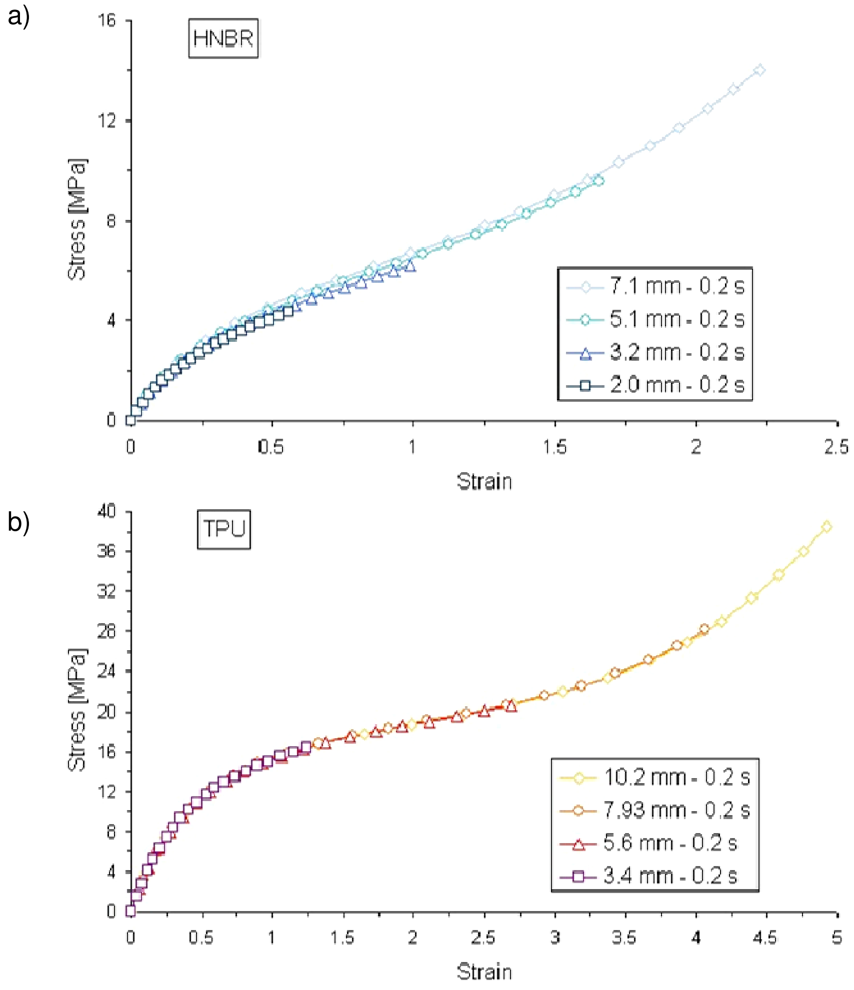

Fig. 3.49: Time dependent nominal stress-strain curves of the finite element simulations in Point 3 in dependence of the maximum displacement values (from 2 to 7. 1 mm) with a test frequency of 5Hz.

From Figures 3.47 and 3.49 the local strain based Wöhler curves were constructed, fitted by a selected function, the strain limits were determined and these curves are shown in Figure 3.50 for both elastomers investigated.

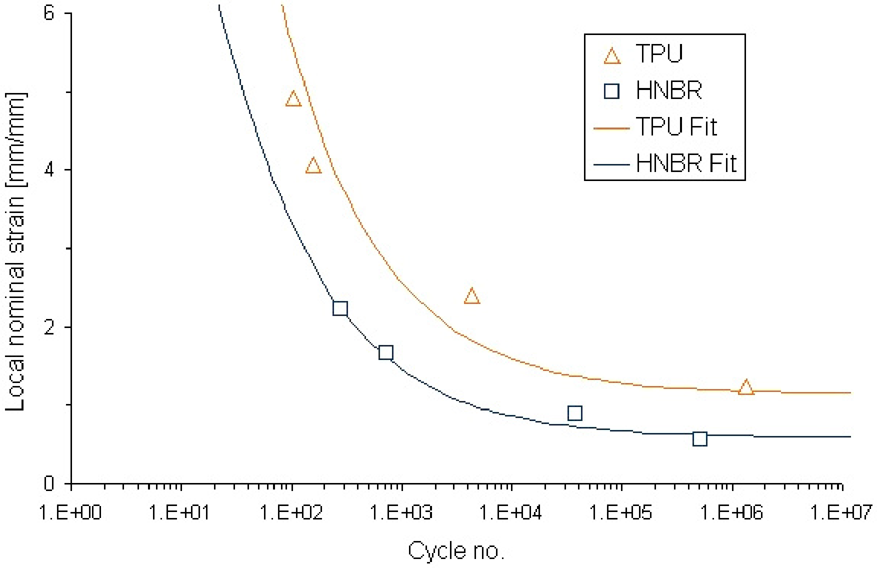

Fig. 3.50: Data points and local strain based Wohler diagrams for both elastomers.

Similar to the previous chapter (section 3.2.2.2, see Figure 3.9), the working hypothesis was in this case too that the two elastomers reveal a distinct fatigue limit. Hence, the measured points in the local strain based Wöhler curve were fitted by a function with a treshold in the positive stress range.

$$\lim_{N_f \to \infty} \varepsilon_{TPU} = 1.14342 + \frac{44.943}{\sqrt{N_f}} + \frac{-75.1585 \cdot \ln(N_f)}{N_f} = 1.14 \tag{3.43}$$

$$\lim_{N_f \to \infty} \varepsilon_{HNBR} = 0.5864 + \frac{27.6214}{\sqrt{N_f}} + \frac{-63.2491 \cdot \ln(N_f)}{N_f} = 0.59 \tag{3.44}$$

Based on the method developed the critical local fatigue strain is 59 % for HNBR and 114 % for TPU. Due to the limited number of points and the selection of the function, for practical engineering purposes this limit value can be taken as a range 55-60 % for HNBR and 105 to 120 % for TPU. Comparing these values with the critical strain values determined in stress controlled uniaxial tests (78 % for

HNBR and higher than 150 % for TPU but), it can be concluded that the displacement controlled Diabolo-type specimens reveal lower critical fatigue strain values.

The following main results were obtained in this section:

- The conduction of displacement controlled fatigue tests is far easier than the conduction of force controlled test.
- Diabolo specimen reveal a stress/strain concentration which localizes the failure in a well-defined volume.
- The reproducibility of the results of these tests highly depends on the quality of the specimen in the notch region.
- The experimental duration of the determination of a Wöhler curve was reduced which can lower the costs for determining relevant fatigue parameters.
- To construct component relevant local strain based Wöhler curves, additional finite element simulations along with adequate material models are necessary.

3.4 Torque controlled torsion cyclic tests

As a further improvement of the fatigue test methodology, torque controlled cyclic torsion tests with constant axial displacement were also performed and the torsion fatigue behaviour for the two elastomers was characterized. It was expected that the torsion fatigue parameter, may contribute to a better understanding and interpretation of the results of the fretting fatigue experiments.

3.4.1 Experimental results

To determine the shear stress fatigue limit (τ_D), torque controlled fatigue tests were carried out on a BOSE ElectroForce® 3200 testing machine (BOSE Corp., MN, USA) under standard laboratory environment (23°C, 50% humidity). The test frequency was 1 Hz with the torque ratio ($R=M_{min}/M_{max}$) 0.1. Preliminary monotonic torsion tests were performed for both material with 0.1 °/s testing speed up to the torque limit (2.5 Nm) of the testing machine; the resulting torque-rotation angle-vertical force curves are shown for both materials in Figure 3.51.

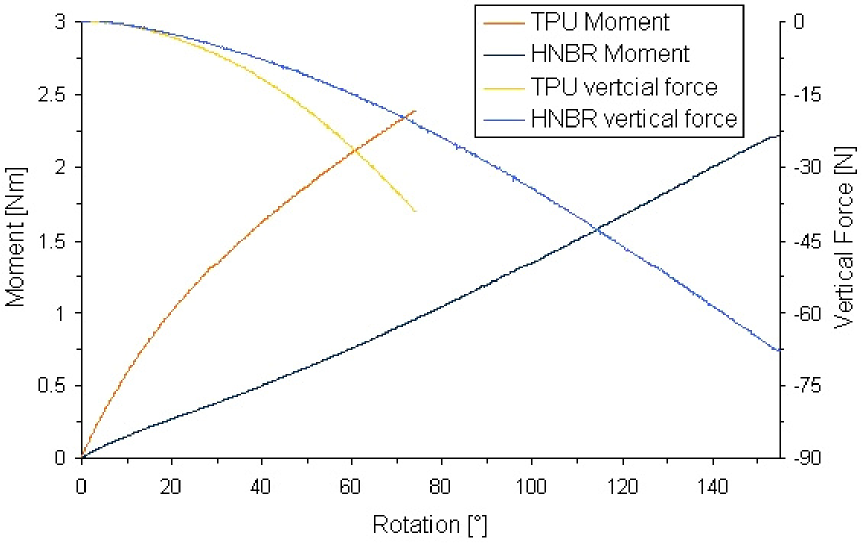

Fig. 3.51: Rotation angle dependence of torque and axial force values during monotonic torsion experiments of HNBR (a) and TPU (b).

As expected, the TPU material revealed a higher torsion stiffness (shear modulus) than HNBR. In addition, as the axial boundary condition was set to constant zero displacement, vertical forces were also measured and printed in the diagram. Similar to the torque curves, TPU revealed higher axial stiffness.

3.4.2 Torsion fatigue results

The fatigue surfaces of the Diabolo-type specimens are visible in Figure 3.52. The initial radial crack initiations are well visible on the fracture surfaces. As expected, significant differences between the fracture surfaces for tension and for torsion were observed (compare with Figure 3.46). Based on the higher roughness of the torqued surfaces it might be speculated that they reveal a more ductile behaviour than the fracture surfaces of the tensile loaded specimens. Furthermore, the two elastomers revealed also different fracture surfaces under similar loading conditions.

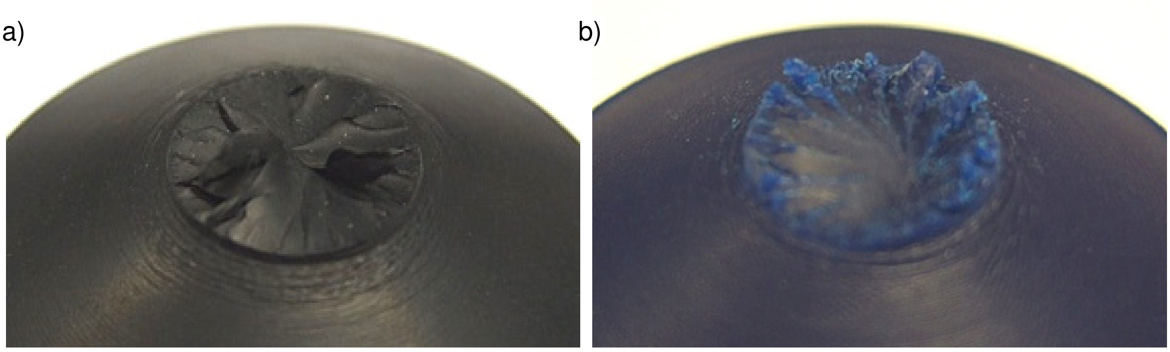

Fig. 3.52: Torsion-fatigue cracked specimen surface of the HNBR (a) and TPU (b) materials.

The maximum shear stresses of the cross section were calculated at the edge with the following equation:

$$\tau_{\max} = \frac{M}{I_p} \cdot r \tag{3.45}$$

where M is the maximum moment in [Nmm], r is the radius of the cross-section (r=4.92mm) and I_p is the second polar moment of a circular cross-section:

$$I_p = \frac{d^4 \cdot \pi}{32} = 1929.33 \quad \left[mm^4\right] \tag{3.46}$$

The failure points determined are shown in Figure 3.53. Contrary to the experiments under axial loading, in all torsion loading situations ultimate rupture of the specimen was clearly observed.

Although the number and trend of the fatigue data points are not sufficient to clearly determine fatigue failure limit values, the fatigue tendency is well characterized. Two possible fitting curves are drawn in the diagram, and the material shear limit is determined for 1 point after 500 kcycles between these two fitting curves ($\tau_{D(HNBR)}$=1.53MPa, $\tau_{D(TPU)}$=4,19MPa).

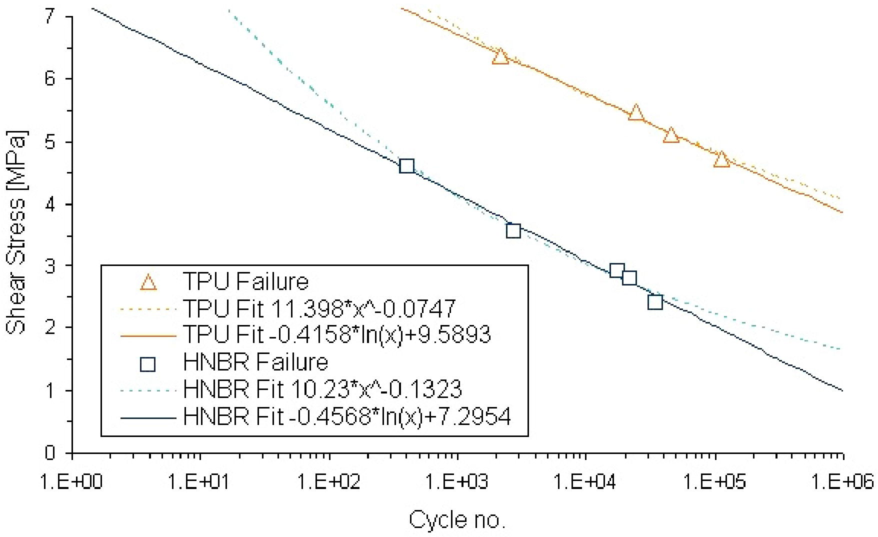

Fig. 3.53: Material failures at given shear stress.

From the measured rotation angles, the shear strain was calculated with the following equation:

$$\gamma_{xy} = r\frac{d\phi}{dy} \qquad (3.47)$$

, where r is the radius of the notch (r=9mm), ϕ is the measured angle in rad and y is the height of the notch section (y=1).

The changes of shear strain ($\Delta\gamma_{xy}$) in the function of the cycles are shown in Figure 3.54.

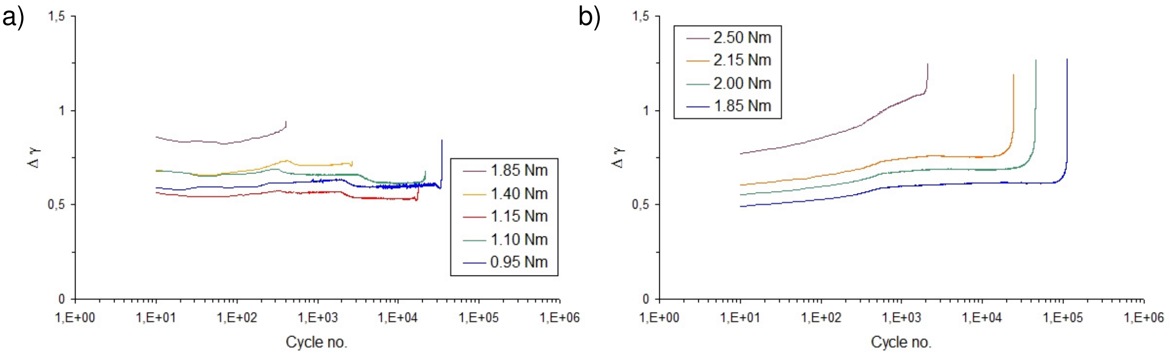

Fig. 3.54: Shear strain change vs. cycle number for HNBR (a) and TPU (b) materials.

While Δγ stays nearly constant during the measurements, the maximum angle has a well visible tendency (Figure 3.55)

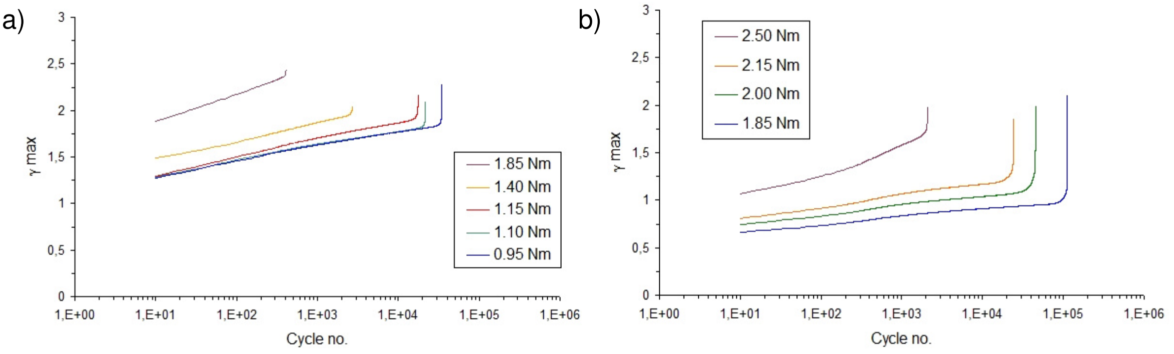

Fig. 3.55: Shear strain maxima under moment controlled fatigue of HNBR (a) and TPU (b).

3.5 Summary and conclusions of fatigue tests

3.5.1 Uniaxial stress controlled fatigue tests

Cyclic deformation and fatigue failure behaviour under force controlled uniaxial test condition were characterized for HNBR and TPU materials in this chapter. The schematic representation of the applied data reduction methodology is shown in Figure 3.56. At first, the surface crack initiation type failure mode was investigated from the tested samples by fracture surface analysis. Somewhat surprisingly, no clear deviation was observed for the fatigue behaviour regarding the fatigue life time (cycles-to-failure values) between the different surface roughness values. The fatigue stress limit was estimated with the experimental data and the fitting curves for HNBR.

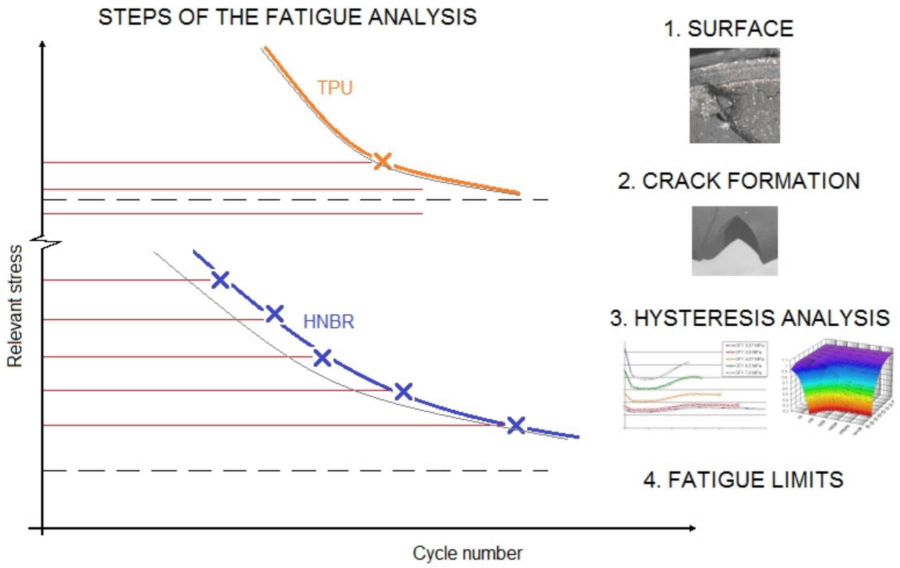

Fig. 3.56: Schematic representation of the determination of the Wöhler curves for the elastomers examined.

The process of crack formation was observed with the developed optical system, which is described in chapter 2. Rapid failures occurred in both cases. While no visible crack propagation was detected for the TPU material, crack formation for the HNBR material occurred only in a few cycles before ultimate failure.

The hysteresis analysis shows different fatigue damage behaviour for the two elastomers investigated. The maximum strain and the strain energy show relevant dependence of the fatigue life as a function of the used maximum stress and cycle number, but the dynamic and secant modulus cannot describe the damage accumulation for HNBR. On the contrary, for TPU the dynamic modulus method could be used as fatigue life predictor. Finally, the stress limits are described with the measured points in case of the HNBR material and with a binary extrapolation of the dynamic modulus change for the TPU material.

Damage accumulation of the elastomers tested

In the hysteresis analysis procedure, the maximum strain, the dynamic modulus and the strain energy were shown as a function of the cycle number. Their change and limits were shown for the maximum stress levels used and significant differences were observed. Based on various indicators (e.g. dynamic modulus, total strain energy density), a nearly linear damage accumulation was observed over a wide cycle number range for HNBR, which was followed by a very nonlinear damage formation over a very short range, slightly before the occurrence of ultimate failure. After the same cycles, higher stress level means a higher dynamic modulus in case of the HNBR measurements, and the modulus tends to reach a constant value. For some HNBR specimens, the dynamic modulus increase is correlated for the fatigue life time which might be explained by strain induced crystallization of this elastomeric material. Damage accumulation is highly non-linear for TPU and was described by the continuous and simultaneous change of the dynamic and the secant modulus values. For TPU, the secant modulus showed the same tendency as the dynamic modulus. While the secant modulus values were found to be stress independent for HNBR, they revealed significant stress level dependence for TPU. For HNBR, however, the maximum strains of the hysteresis cycles were good indicators of the damage process. The strain energy diagrams show that the energy based approach could not characterize the fatigue of these elastomers under the specified conditions used in this thesis.

Finally, the determined fatigue limit values in terms of nominal stresses were 3.7 MPa for the HNBR and 29 MPa for the TPU material under uniaxial conditions. These values are higher than the simulated maximum values of the true stresses which are relevant for multiaxial stress states and which were determined (<4MPa) in Point 2 and in Point 3 of the fretting contact simulations (see Section 1.4.2.3). It should be noted here that the described limits do not contain the effect of the stress ratio and the frequency. They are objectives of future research work.

3.5.2 Fatigue tests using Diabolo-type specimens

A novel Diabolo-type specimen along with an appropriate test set-up was developed and implemented in the experimental work, as described in this chapter. Due to the localized strain and stress in the mid section and the stable fixture of the specimen, the reproducibility of the test results is sufficient for a reliable fatigue analysis. Furthermore, due to the displacement controlled loading and the easier and more accurate machine tuning, a higher frequency range or a significantly better test frequency/amplitude combination is available for these fatigue tests. Moreover, determination of material fatigue is possible with a continuous measurement of the force peak and force valley values during the loading cycles. Finally, for both elastomeric materials displacement controlled tensile and torque controlled torsion fatigue tests were performed under laboratory conditions using the developed Diablo-type specimens.

The strain concentrations of the smooth notched Diabolo-type specimen were determined by finite element simulations. In addition to the hyperelastic model used in the fretting simulation in chapter 1, a combined viscoelastic-hyperelastic material model was used in these simulations. The use of this type of material model allows for the consideration of rate dependence for elastomers. While TPU revealed a rather significant rate dependence, only minor influence of the rate was shown for HNBR. Based on the simulation results the local stress/strain states were defined as a function of the global displacement. These calibration curves were later used to construct local strain based Wöhler curves for both elastomers.

Due to the smooth notched specimen geometry and to the highly nonlinear material behaviour, only the first loading part of the cyclic loading can be described with these simulations. The stress states inside the material are always variable depending on the connection of the middle neck and the remaining parts of specimen deformation. Some simulation methods mentioned in the research literature propose to involve Mullins effect (continuous softening in the first phase of the displacement controlled loading) and hysteretic behavior, but curently only the first hysteretic cycle can be modelled without creep effect with the commercial FEM code. Further work will include the implementation of these models with proper material data to extend the simulation of the cyclic behaviour of elastomers.

Furthermore, the experimentally determined cycles-to-failure and the simulated local strain values were then used to construct strain based Wöhler curves for both elastomers. By modifying the conventional Wöhler curve, local strain fatigue limit values for both materials were determined, applying the relationship between the simulated local strain and the global displacement of the displacement controlled fatigue tests. The data points were fitted by a proper mathematical function with the assumption that the two elastomers reveal a distinct fatigue limit in terms of local strain values. Although the experimental data support this assumption and the definition of a fatigue limit is useful for practical engineering design procedures further investigations are necessary to substantiate the hypothesis and to make correlations with different elastomer structures.

The fretting contact and loading imply a highly multiaxial loading situation for the cases investigated. Due to the relevance of shear induced stress in the fretting contact, and to extend the fatigue test methodology to multiaxial loading situations, fatigue tests under cyclic torsion loading were carried out and described in the final part of this chapter.

Torque controlled fatigue tests with Diabolo-type specimens were performed at various shear stress levels, and shear stress Wöhler curves were constructed. In contrast to the previous fatigue experiments under tensile loading (see section 3.2) no clear shear fatigue limits were determined based on these test results. To compare the results with the results of above measurements, an apparent fatigue limit was estimated at 500 kCycles. The measured fatigue limit values of all fatigue tests for both elastomers are shown in Table 3.5 in terms of applied nominal stress, σ_D, strain, ε_D, and shear stress, τ_D.

Material	σ_D **[MPa]**	ε_D **[mm/mm]**	$\tau_{D\ (N=500kCycles)}$ **[MPa]**
HNBR	3.73	0.59	1.53
TPU	28.95	1.14	4.19

Table 3.5: Fatigue limit values determined at R = 0.1.

3.6 Comparison of fretting fatigue and bulk fatigue results

A functional model was proposed based on the combination of the failure analysis of the fretting fatigue experiments and the simulation and the determination of the relevant stress components. While microcrack formation was observed at low shear stress values for HNBR, irreversible inelastic deformation induced waviness formation was observed for TPU. Comparing the stress levels in Figures 1.61 and 1.62 with the stress levels in Table 3.5, it is evident that the shear stresses lie in similar ranges. The uniaxial test predicts significantly higher stress limits.

The location of the maximum principal strain and the von Mises stress in the fretting simulations for various tangential displacement amplitudes are shown in Figure 3.57 and in Figure 3.58 for HNBR.

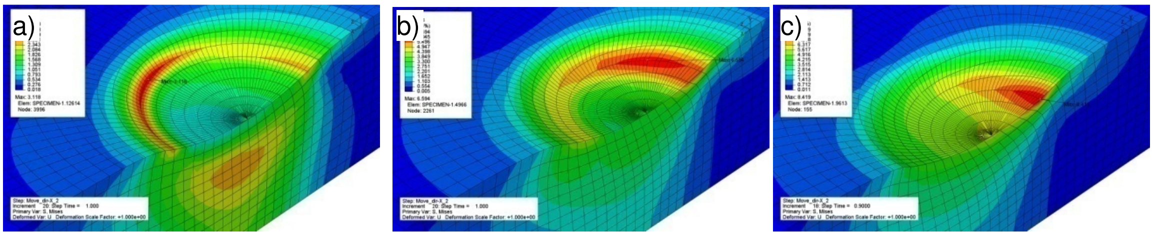

Fig. 3.57: Location of the maximum von Mises stress at a the tangential displacement amplitude of 0.1 mm (a), 0.6 mm (b) and 1 mm (c) for HNBR material model.

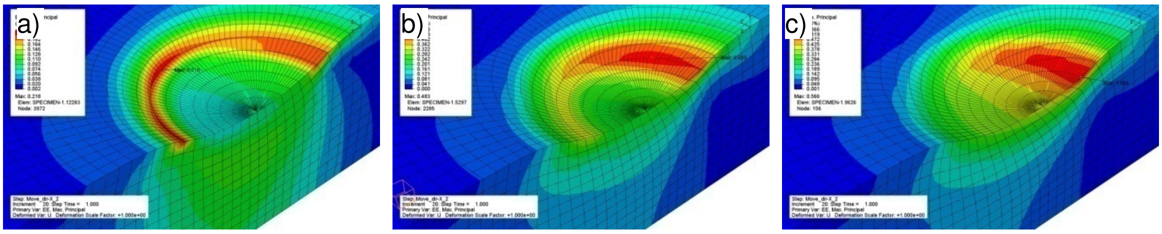

Fig. 3.58: Location of the maximum principal strain at a tangential displacement amplitude of 0.1 mm (a), 0.6 mm (b) and 1 mm (c) for HNBR material model.

The variation of the maximum value of the principal strain and of the von Mises stress in one cycle of the HNBR fretting simulation is shown in Figure 3.59. The maximum values of these curves were used to produce the data points in Figure 3.63.

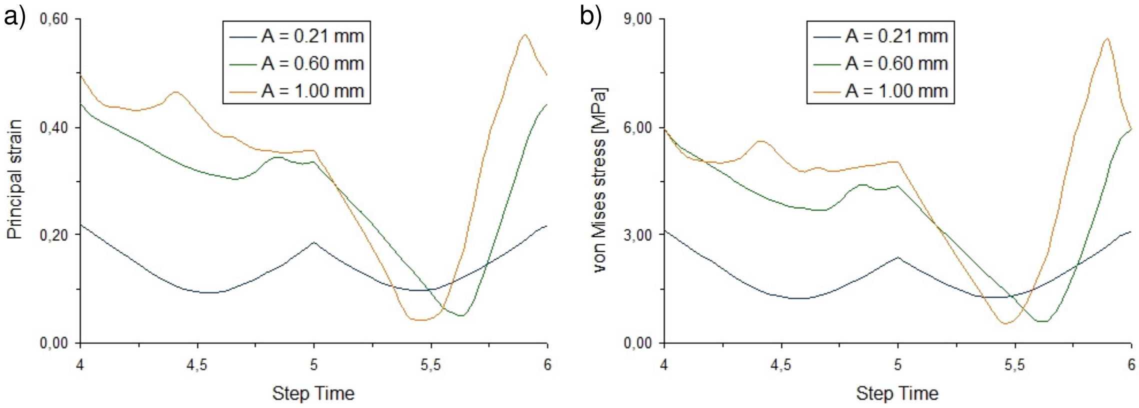

Fig. 3.59: Variation of the maximum value of the principal strain (a) and of the von Mises stress (b) in one cycle of the HNBR fretting simulation.

The locations of the maximum principal strain and stress in the fretting experiments for various tangential displacement amplitudes are shown in Figures 3.60 and 3.61 for TPU.

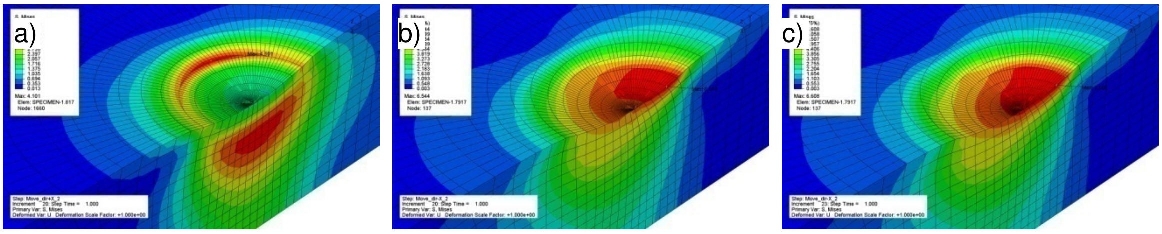

Fig. 3.60: Location of the maximum von Mises stress at a tangential displacement amplitude of 0.1 mm (a), 0.3 mm (b) and 0.4 mm (c) for TPU material model.

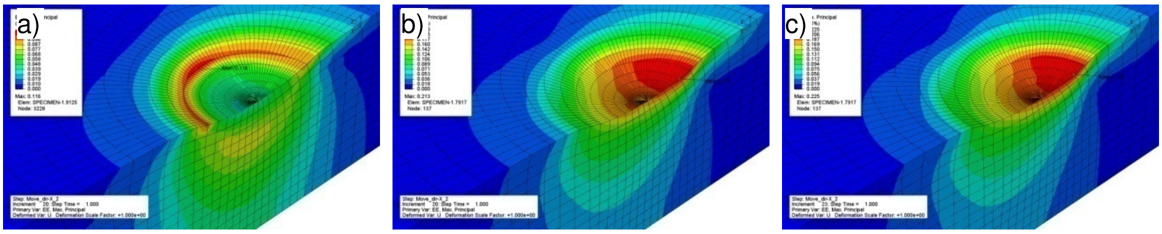

Fig. 3.61: Location of the maximum principal strain at a tangential displacement amplitude of 0.1 mm (a), 0.3 mm (b) and 0.4 mm (c) for TPU material model.

The variation of the maximum value of the principal strain and of the von Mises stress in one cycle of the TPU fretting simulation is shown in Figure 3.62.

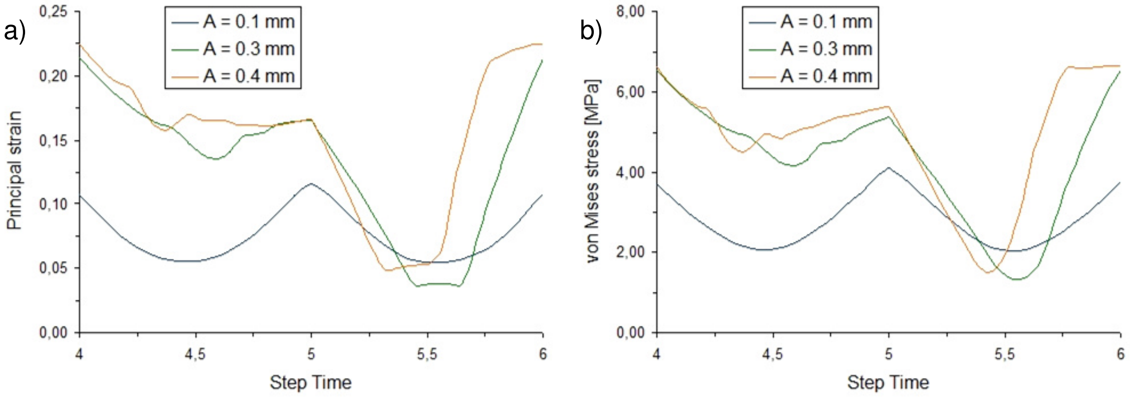

Fig. 3.62: Varaition of the maximum value of the principal strain (a) and of the von Mises stress (b) in one cycle of the TPU fretting simulation.

The essence of these images is summarized in Figure 3.63. Principal strain and equivalent stress values are shown as a function of the tangential displacement amplitude for both elastomers investigated. While for HNBR the relevant strain and stress values are very near to the range of the uniaxial fatigue limit values (strain 0.59 and stress 3.7 MPa) at low displacement amplitudes, for TPU higher differences were observed (strain 1.14 and stress 29 MPa). As it was clearly shown in the fretting model in Section 1.5.1 (Figures 1.61 and 1.62), the relevant tangential displacement regime for crack initiation and propagation by crater formation is up to 0.5 mm for HNBR. In this regime both principal strain and stress values of the contact are only slightly smaller than the estimated fatigue limit values.

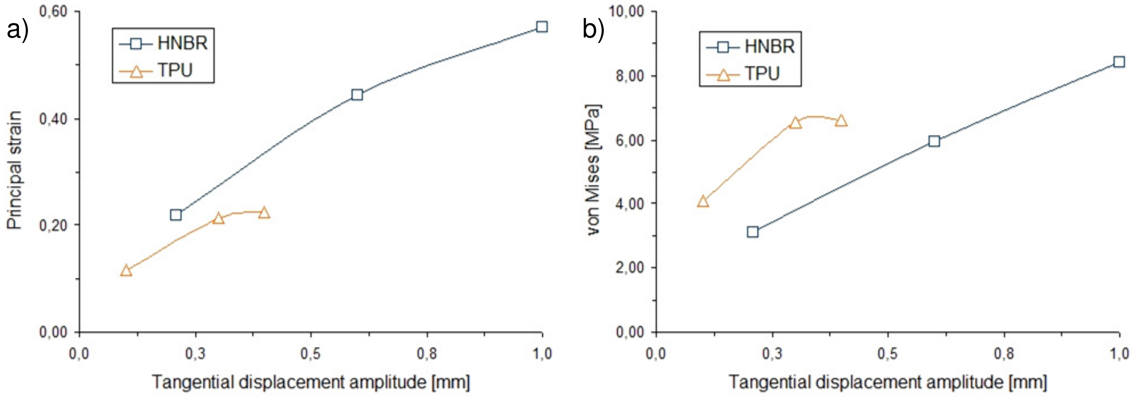

Fig. 3.63: Maximum principal strain values (a) and the maximum von Mises stress values (b) in the function of the tangential displacement amplitude for both elastomeric materials.

Considering the uncertainty of the fitting functions and the influence of the stress multiaxiality, it can clearly be stated that the probability of the occurrence of fretting fatigue failure is very high for HNBR under these conditions. While the crack initiation is associated with the high local strain, the crater formation is related to the combination of local strain and sliding.

In contrast, for TPU a different failure mode was shown. The dominant damage is the waviness formation on the surface by localized inelastic deformation, which is reflected by the results of the bulk fatigue experiments. The fatigue limit strain and stress values are significantly lower than the principal strain and stress values simulated for TPU in contact situations. In this case, the shear deformations and the resulting stresses play an important role in the damage formation as shown in Table 3.5 (see shear stress values). The shear fatigue limit estimated is in the range of the contact shear stresses simulated (compare Figure 1.62). However, further work should clarify the mechanisms and the role of the local inelastic deformation for TPU under cyclic contact conditions.

References

F. Abraham, T. Alshuth, S. Jerrams (2005): „The effect of minimum stress and stress amplitude on the fatigue life of non strain crystallising elastomers" Materials and Design 26, pp. 239–245.

V. Altstädt, (1987): „Hysteresismessung zur Charakterisierung der mechanisch-dynamischen Eigenschaften von R-SMC", Dissertation, Institute for Materials Engineering, Universität Kassel, D.

A. Andriyana, E. Verron (2007): „Prediction of fatigue life improvement in natural rubber using configurational stress", International Journal of Solids and Structures 44, pp. 2079-2092.

O.H. Basquin (1910): „The Exponential Law of Endurance Tests", Proc. ASTM Part 2, Vol. 10, pp. 625-630.

J.T. Bauman, C.H. Verlag (2008): „Fatigue, stress, and strain of rubber components", Hanser Gardner Publications, Germany.

J.R. Beatty (1964): „Fatigue of rubber", Rubber Chemistry and Technology 37, pp. 1341-64.

A. Bennani, L. Laiarinandrasana, R. Piques, S. Cantournet (2003): „Influence of the filler properties on the mechanical response of silicia filled natural rubber" in Constitutive models for rubber III, pp. 177-195.

C. Berger, B. Pyttel, D. Schwerdt (2008): „Beyond HCF – Is there a fatigue limit?", Materialwissenschaft und Werkstofftechnik 39, pp. 769 – 776.

T. Bui-Quoc (1975): „High-temperature fatigue-life estimation: extensionof a unified theory", Experimental Mechanics 15, pp. 219-225.

S.M. Cadwell, R.A. Merrill, C.M. Sloman, F.L. Yost (1940): „Dynamic fatigue life of rubber", Industrial and Engineering Chemistry, Analytical Edition 12, pp. 19-23.

J.S. Dick (2001): „Improving the Physical Properties of Cured Rubber Compounds", „Rubber Technology: Compounding and Testing for Performance", Hanser Gardner, pp. 23.

A. Fatemi, I. Yang (1998): „Cumulative faigue damage and life prediction theories : a survey of the state art for homogeneous materials", Internal Journal of Fatigue 20, pp. 9-34.

A.N. Gent, P.B. Lindley, A.G. Thomas (1964): „Cut Gwoth and Fatigue of Rubbers. I. The Relationship Between Cut Growth and Fatigue," Journal of Applied Polymer Science 8, pp. 455-466.

S.M. Goh, M.N. Charalambides, J.G. Williams (2004): „Determination of the constitutive constants of non-linear viscoelastic materials", Mechanics of Time-Dependent Materials 8, pp. 255-268.

H.W. Greensmith (1963): „Rupture of Rubber. X. The change in Stored Energy on Making a Small Cut in a Test Piece Held in Simple Extension," Journal of Applied Polymer Science 7, pp. 993-1002.

K. Grosh (1988): „Rolling resistance and fatigue life of tires”, Rubber Chemistry and Technology 61, pp. 42-63.

H.J. Grover (1960): „An observation concerning the cycle ratio in cumulative damage” in Symphosium on Fatigue of Aircraft Structures, American Society for testing and Materials, Philadelphia, pp. 120-124.

H. Hirakawa, F. Urano, M. Kida (1978): „Analysis of fatigue process of rubber vulcanizates”, Rubber Chemistry and Technology 51(2), pp. 201–214.

P. Höfer, A. Lion (2009): „Modelling of frequency and amplitude dependent material properties of filler reinforced rubber”, Journal of the Mechanics and Physics of Solids 57, pp. 500-520.

W. B. Hwang, K.S Han (1989): „Fatigue of Composite Materials - Damage Model and Life Prediction“ in „Composite Materials - Fatigue and Fracture - ASTM STP 1012“, (P.A. Lagace, ed.), Vol. 2, American Society for Testing and Materials, Philadelphia, USA, pp. 87-102.

S. Ito (2003): „HNBR - A very versatile engineering elastomer”, in „Engineering Elastomers 2003: Conference Proceedings”, Geneva, Switzerland, 13-14 November 2003.

M. Kaliske, H. Rothert (1997): „Formulation and implementation of three-dimensional viscoelasticity at small and finite strains”, Computational Mechanics 19, pp. 228-239.

W. Kim, M. Kim, Y.-W. Chang, J.-E. Shin, J.-W. Bae (2003): „Fatigue Crack Growth Behavior of NR and HNBR Based Vulcanizates with Potential Application to Track Pad for Heavy Weight Vehicles”, Macromolecular Research 11, No. 2, pp. 73-79.

W.D. Kim, H.J. Lee, J.Y. Kim, S.K. Koh (2004): „Fatigue life estimation of an engine rubber mount”, International Journal of Fatigue 26, pp. 553-560.

G.J. Lake, P.B. Lindley (1964): „Cut growth and fatigue of rubbers. II. Experiments on noncrystallizing rubbers”, Journal of Applied Polymer Science 8, pp. 707–721.

G.J. Lake, P.B. Lindley (1965): „The Mechanical Fatigue Limit for Rubber”, Journal of Applied Polymer Science 9, pp. 1233-1251.

G.J. Lake (1971): „Mechanical Fatigue of Rubber”, Division of Rubber Chemistry, American Chemical Society, Cleveland, Ohio, October 12-15, pp. 309-328.

P. Lazzarin, P. Livieri, F. Berto, M. Zappalorto (2008): „Local strain energy density and fatigue strength of welded joints under uniaxial and multiaxial loading”, Engineering Fracture Mechanics 75, pp. 1875–1889.

W.E. Mahmoud, S.A. Mansour, M. Hafez, M.A. Salam (2007); “On the degradation and stability of high abrasion furnace black (HAF)/acrylonitrile butadiene rubber (NBR) and high abrasion furnace black (HAF)/graphite/acrylonitrile butadiene rubber (NBR) under cyclic stress-strain”, Polymer Degradation and Stability 92, pp. 2011-2015.

S.M. Marco, W.L. Starkey (1954): „A concept of fatigue damage”, American Society Of Mechanical Engineers 76, pp. 627-632.

W.V. Mars, A. Fatemi (2002): „A literature survey on fatigue analysis approaches for rubber”, International Journal of Fatigue 24, pp. 949-961.

W.V. Mars, A. Fatemi (2004): „Factors that affect the fatigue life of rubber: a literature survey”, Rubber Chemistry and Technology 77, pp. 391–412.

M.A. Miner (1945): „Cumulative damage in fatigue”, Journal of Applied Mechanics 67, pp. A159-164.

H.L. Oh (1980): „A fatigue-life model of a rubber bushing”, Rubber Chemistry and Technology 53, pp. 1226-1238.

G. Pinter, E. Ladstätter, W. Billinger, R.W. Lang (2006): „Characterization of the tensile fatigue behaviour of RTM-laminates by isocyclic stress-strain-diagrams”, Internal Journal of Fatigue 28, pp. 1277-1783.

R.S. Rivlin, A.G. Thomas (1953): „Rupture of Rubber. I. Characteristic Energy of Tearing”, Journal of Polymer Science 10, 3, pp. 291-318.

N. Saintier, G. Cailletaud, R. Piques (2006): „Multiaxial fatigue life prediction for natural rubber”, International Journal of Fatgie 28, pp. 530–539.

O.A. Shergold, N.A. Fleck, D. Radford (2006): „The uniaxial stress versus strain response of pig skin and silicone rubber at low and high strain rates”, Int. Journal of Impact Engineering 32, pp. 1384-1402.

S. Suresh (1998): „Fatigue of Materials”, Cambridge University Press, Germany

R. Talreja, (2001):. „Fatigue of Polymer Matrix Composites“ in „Polymer Matrix Composites“, (R. Talreja und J.-A.E. Månson, ed.), Elsevier Science, Oxford, UK. pp. 529-552.

E. Verron, A. Andriyana (2008): „Definition of a new predictor for multiaxial fatigue crack nucleation in rubber”, Journal of the Mechanics and Physics of Solids 56, pp. 417-443.

Chang-Su Woo, Wan-Doo Kim, Jae-Do Kwon (2008): „A study on the material properties and fatigue life prediction of natural rubber component”, Material Science and Engineering A 483-484, pp. 376-381.

A. Wöhler (1867): „Wöhler's experiments on the strength of metals”, Engineering 2, pp. 160-161.

D.G. Young (1986): „Fatigue Crack Propagation in Elastomer Compounds: Effects of Strain Rate, Temperature, Strain Level and Oxidation,” Rubber Division, American Chemical Society, New York, N.Y. April 8-11, pp. 809-825.

B.A. Zahnt (2003): „Eermüdungsverhalten von Diskontnuierlich glaserverstärkten kunststoffen“, Dissertation, Institute of Materials Science and Testing of Plastics, Montanuniversität Leoben, A.

Sz. T. Vezér, Z. Major (2008): „Analog triggered image acquisition method for optical measurement under cyclic load conditions”, Materials Engineering 15, pp. 5-13.

4. OVERALL CONCLUSION AND OUTLOOK

The fretting fatigue behaviour and the bulk fatigue behaviour of a thermoset rubber (Hydrogenated Nitrile Butadiene Rubber - HNBR) and a thermoplastic polyurethane grade (TPU) were characterized by various experimental methods and by finite element simulations. The main results along with the conclusions are summarized below.

Fretting fatigue – method development

A novel fretting fatigue test equipment was developed and used to characterize the fretting fatigue behaviour of two elastomer types. The fretting was modelled by a metallic sphere-elastomer plate contact with the assumption of a rigid body like motion of the test specimen. Short-term cyclic experiments in a fretting contact situation were carried out over a wide normal force and tangential displacement range. The sliding regime was defined based on the tendencies of the hysteretic tangential force-displacement curves. The results are summarized in “Running Condition Fretting Maps” (RCFM) for both elastomers.

Furthermore, to characterize the fretting failure mechanisms at various sliding regimes, long-term fretting fatigue tests were performed at a selected normal load over a wide tangential displacement range. The failure types in the fretting paths were analyzed by various microscopy methods and subsequently classified.

Moreover, a finite element simulation model was developed using the fretting test configuration and model with relevant parameters for both elastomers. The material parameters for the 3rd order Ogden type model were determined in preliminary experiments under monotonic compressive/tensile loading conditions. The observations of the failure analysis and the results of the FE simulations were summarized in fretting failure models for both elastomers. Good agreement was found between the location and distribution of the shear stress values simulated in sliding contact and the failure modes observed in the real fretting experiments.

Bulk fatigue – method development

In addition to the characterization of the surface related fretting fatigue failure behaviour, the bulk fatigue behaviour of the two elastomer grades was characterized. Conventional nominal stress based Wöhler curves were constructed using the results of uniaxial force controlled cyclic tests at various force levels. To gain more insight into the kinetics of the failure process a comprehensive analysis of the hysteretic force-displacement curves was performed by simultaneously detecting and recording crack initiation and propagation with a novel image analysis method. This image analysis method consists of the following main parts: local strain measurement, a smart trigger tool, a proper image acquisition and recording module.

The visually observed distinct differences between the hysteretic curves of HNBR and TPU were quantified by the analysis of the tendencies of the dynamic and secant modulus as well as by strain energy values. While a standard Wöhler curve could be constructed by applying conventional cycles to ultimate failure values for HNBR, a novel softening type Wöhler curve was proposed and constructed for TPU. In both cases the existence of a pronounced fatigue limit was assumed, at least from a practical engineering point of view.

To overcome the experimental difficulties of force controlled cyclic tests of elastomers, displacement controlled cyclic tests were carried out using a novel “Diabolo type” specimen configuration under axial loading. Local strain based Wöhler curves were constructed using the local strain values of FE simulations and the cycles-to-failure values determined on the Fmax/Fmin-cycle number diagrams. Finally, to further improve the multiaxial character of the fatigue analysis, torque controlled torsion fatigue tests using the same “Diabolo-type” specimens were performed and Wöhler curves for this loading situation were constructed.

Fretting fatigue – material characterization

Relevant material parameters for hyperelastic material models were determined by using monotonic uniaxial compressive/tensile tests. The hyperelastic model was selected based on a fitting procedure of the FE simulation tool. In addition, dynamic mechanical analysis experiments under small scale tensile strain conditions were performed and the frequency, the test amplitude and the temperature dependence of the loss and storage modulus were determined. These values can be applied to simulations with viscoelastic or to combined hyperelastic-viscoelastic models.

The differences between the two elastomers observed in the material model were reflected by the FE simulation of the contact deformation. Due to the lower modulus of HNBR, a higher indentation and higher degree of strain localization was obtained in the normal load direction than for TPU. Furthermore, the formation of a characteristic ring-shaped localized shear stress zone was observed for both elastomers. Due to the higher coefficient of friction, the width of this zone was smaller for HNBR.

Moreover, failure started at low shear stress level (see Figure 1.61, 1.5 MPa) with micro-crack initiation and continued at higher normal loads/sliding distance in a crater formation and finished in a dominant abrasion wear process for HNBR. Contrary to this observation, failure started at a higher shear stress level (see Figure 1.62, 3 MPa) with plastic deformation of the contact surface for TPU. This resulted in a waviness formation on the specimen surface and transformed into a combined adhesive and abrasive wear without clear sign of micro-crack formation.

Bulk fatigue – material characterization

In general, visible crack initiation and propagation were observed for both elastomer types only at the end of the uniaxial force controlled fatigue experiments (several 100 for HNBR and several 10 or less for TPU). The dynamic modulus is nearly stress and cycle independent for HNBR and highly stress and time dependent for TPU. The change of the dynamic modulus for TPU is well described with a mathematical fitting function. The secant modulus does not depend on the load for HNBR and highly depends on the load for TPU. The change of the secant modulus reflects the degree of the creep deformation during the cyclic loading. In spite of the significant difference in modulus values, both materials revealed the same degree of creep deformation, while the dynamic modulus was nearly constant for HNBR and changed continuously for TPU. The strain energy reveals the same asymptotic tendency for both elastomers without any sign of damage initiation

Furthermore, it is assumed that a distinct fatigue strength limit (app. 4MPa for HNBR and 29 MPa for TPU) for both elastomers exists under tensile loading conditions, at least from an engineering point of view. In spite of the fact that no conventional Wöhler curve was measured for TPU, the softening Wöhler curve indicated the change of the material resistance against fatigue. Contrary to this, no such limit was observed in the torsion fatigue tests for both elastomers.

The basic material model was completed by considering time dependence of the material deformation behaviour. A combined hyperelastic-viscoelastic model was derived based on a method proposed in the literature, and material parameters for both elastomers were determined. While HNBR reveals a lower modulus and a high strain hardening at large strains, TPU shows a higher initial modulus and a significantly lower hardening. The influence of this basic material behaviour on the strain localization was successfully simulated and described by the model above.

Finally, in spite of all efforts no direct relationship was found between the fretting fatigue and the bulk fatigue behaviour for the investigated elastomer grades. The finding of this correlation along with the extension and quantitative characterization of the fatigue behaviour over a wide stress multiaxiality/constraint range remains a challenging task for further research.

APPENDIX

Documentation of the analog triggered image acquisition software.